Optimization of a 4th generation CMB space mission

Ranajoy Banerji

To cite this version:

Ranajoy Banerji. Optimization of a 4th generation CMB space mission. Physics [physics]. Université Sorbonne Paris Cité, 2017. English. NNT : 2017USPCC199 . tel-02019119v2

HAL Id: tel-02019119
https://theses.hal.science/tel-02019119v2

Submitted on 18 Apr 2019

UNIVERSITÉ SORBONNE PARIS CITÉ

Thèse préparée
à L'UNIVERSITÉ PARIS DIDEROT
École doctorale STEP'UP – ED N° 560
Laboratoire Astroparticule et Cosmologie

Optimisation d'une mission spatiale CMB de 4eme génération

par
Ranajoy Banerji

présentée et soutenue publiquement le
21 septembre 2017

Thèse de doctorat de Science de la Terre et de l'environnement

dirigée par Jacques Delabrouille

devant un jury composé de :

Jacques Delabrouille	Directeur de thèse
Directeur de recherche	CNRS-IN2P3, APC, Paris-VII
Stavros Katsanevas	Président
Professeur	APC, Paris-VII
Karim Benabed	Rapporteur
Directeur de recherche	IAP, UPMC
Anthony Challinor	Rapporteur
Reader	Institute of Astronomy, University of Cambridge
Delphine Hardin	Membre
Professeur	LPNHE, UPMC
Nicolas Ponthieu	Membre
Chargé de recherche	CNRS, IPAG, Grenoble

ABSTRACT

The Cosmic Microwave Background radiation is a rich and clean source of Cosmological information. Study of the CMB over the past few decades has led to the establishment of a "Standard Model" for Cosmology and constrained many of its principal parameters. It has also transformed the field into a highly data-driven domain.

Currently, Inflation is the leading paradigm describing the earliest moments of our Universe. It predicts the generation of primordial matter density fluctuations and gravitational waves. The CMB polarisation carries the signature of these gravitational waves in the form of primordial "B-modes". A future generation of CMB polarisation space mission is well suited to observe this signature of Inflation.

This thesis focuses on optimising a future CMB space mission that will observe the B-mode signal for reaching a sensitivity of $r = 0.001$. Specifically, I study the optimisation of the scanning strategy and the impact of systematics on the quality of polarisation measurement.

RÉSUMÉ

Le rayonnement du Fond Diffus Cosmologique est une source riche et propre d'informations cosmologiques. L' étude du CMB au cours des dernières décennies a conduit à la mise en place d'un modèle standard pour la cosmologie et a permis de mesurer précisément ses principaux paramètres. Il a également transformé le domaine, en le basant davantage sur les données observationnelles et les approches numériques et statistiques.

A l'heure actuelle, l'inflation est le principal paradigme décrivant les premiers moments de notre Univers. Elle prédit la génération de fluctuations de la densité de matière primordiale et des ondes gravitationnelles. Le signal de polarisation du CMB porte la signature de ces ondes gravitationnelles sous la forme de modes-B primordiaux. Une future génération de missions spatiale d'observation de la polarisation du CMB est bien adaptée à l'observation de cette signature de l'inflation.

Cette thèse se concentre sur l'optimisation d'une future mission spatiale CMB qui observera le signal en modes-B pour atteindre une sensibilité de $r = 0{,}001$. Plus précisément, j'étudie la stratégie d'observation et l'impact des effets systématiques sur la qualité de la mesure de polarisation.

DEDICATION AND ACKNOWLEDGEMENTS

First and foremost to thank is my PhD supervisor who took me on when I hardly knew anything about CMB observation. He kept feeding me interesting ideas and provided me space to let them grow into the work I present here. Collaborating with others at APC, especially Guillaume, helped me develop my work faster and introduced me to new ideas. APC has been a great place to work and I wish to thank anyone else who I have come across here over the years.

Among the students at APC my first shout goes out to Pierros for being a great friend. To all the others who have been occupants of 427B and 312B over the years especially Cyrille, Alessandro, Thuong and Mikhail, my appreciation of your friendship. The help I received from Julien and Davide helped me overcome several of my deficiencies regarding the CMB and computing. The coffee sessions with Dhiraj every afternoon was something I looked forward to and enjoyed the interesting discussions which ranged from physics to politics to movies. For the constant supply of great coffee a special thanks to Ken.

To all my friends and acquaintances, Paris would not have been the same without you. Special thanks to Bitan, Ayan and Shantanu for being wonderful and supportive friends. It goes without mentioning that my life would have been different without my best friend Debashmita, whose support and friendship is what got me through life on several occasions.

Last but not the least, my parents, who have been supportive of everything I have done in life and allowed my to pursue my dreams, be it music or physics.

TABLE OF CONTENTS

LIST OF TABLES

TABLE **Page**

LIST OF FIGURES

CHAPTER 1

THE COSMIC MICROWAVE BACKGROUND AND INFLATION

The Cosmic Microwave Background (CMB) is undoubtedly one of the richest and cleanest sources of information about the Universe. Observation and analysis of the CMB radiation and its anisotropies, small fluctuations in its intensity and polarisation, has been instrumental in establishing a ‘Standard Model’ for Cosmology and heralding in an age of precision measurement of several cosmological parameters. The Cosmic Microwave Background provides an unique testing ground for a variety of physical theories, unprecedented in scope and scale to any other probe. It allows us to test physical theories on both the quantum and cosmological scale simultaneously as its properties are the outcome of both quantum and gravitational processes in the early Universe. The energy scales that can be probed range from a few meV to energies as high as the Planck scale.

A remnant radiation from a hot, dense and young Universe was first proposed in the $1940's$ by Alpher, Herman and Gamow [1][2] to explain the relative abundance of the lightest elements. A serendipitous discovery of a faint radiation in every direction by the radio telescope at Bell Labs by Penzias and Wilson in 1965 [3][4] led to the detection of the Cosmic Microwave Background Radiation and provided an early vindication of a hot ‘Big Bang’ model for cosmology. The uniformity of the radiation in every direction provided a direct verification of the principles of Homogeneity and Isotropy that had till then been only a smart guess. This further motivated the formulation of a theory of ‘Inflation’, an exponential phase of expansion of the Universe, to explain the remarkable homogeneity. This also led to the formulation of how quantum fluctuations seeded the early Universe with inhomogeneities that eventually collapsed under gravity to form the galaxy clusters we observe at present. The magnitude of these fluctuations, imprinted on the CMB at the last scattering surface, was measured to 1 part per 10^5 by COBE/DMR [5] and COBE/FIRAS also showed that the CMB radiation spectra conforms almost perfectly to a black body [6], indicating that it was at thermal equilibrium with the hot plasma of the early Universe. Subsequent measurements of the CMB temperature anisotropies and characterisation of the acoustic peaks in the power spectrum, over the next two decades, by instruments such as DASI, BOOMERanG, WMAP and Planck, among others, led to the establishment of the facts that we reside in a locally flat Universe that is composed not only of ordinary baryonic matter, but also ‘Dark Matter’, which does not interact electromagnetically with ordinary matter, and of a more elusive component ‘Dark Energy’, which dominates at our current epoch and is responsible for an accelerated expansion of the Universe. Precision measurement of the shape of the CMB temperature power spectrum as well as CMB polarisation by the current generation of experiments such as BICEP/Keck, POLARBEAR, ACT, SPT and *Planck* , has placed strong constraints on several of the cosmological parameters and provided us hints of Inflation by putting strong constraints on the nearly scale invariant scalar power spectrum and on the level of non-Gaussianity.

The CMB acts as a backlight to all the processes that took place in the Universe post the Recombination epoch and thus encodes information regarding the Reionisation history. Through the process of weak lensing it encodes information regarding the Dark Matter distribution, the sum of neutrino masses and properties of dark energy among others. Hot gas in galaxy clusters inverse Compton scatters with the CMB photons and alters its spectral distribution. This offers us a new probe of galaxy clusters and their peculiar velocities. Present and future generations of CMB experiments are aiming to probe all these science possibilities and exploit them to the fullest. Together with the temperature anisotropy information, precision measurements of the polarisation signal is expected to lead us to the correct model for Inflation and put additional constraints on cosmological parameters, help break degeneracies between parameters, and provide us deeper insight into the early history and formation of the Universe.

In this chapter we develop, in brief, the mathematical framework on which our Cosmological theories and hypotheses are based. We start off by modelling our expanding Universe and its dynamics and develop certain key concepts and relations. We give a brief timeline of the thermal history of the universe and the process of formation of the Cosmic Microwave Background. We introduce the Inflationary model as a solution to horizon and flatness problem, formulate its basic principles, and show how the initial quantum fluctuations, during Inflation, seed the young Universe. We show the evolution of these perturbations and eventually how they are imprinted on to the CMB at the last scattering surface. We relate the fluctuations induced by the initial quantum perturbation to the CMB anisotropies and its statistics and briefly describe the sources of secondary anisotropies and how they encode additional information on to the CMB. This chapter captures the essence of the Physics and the motivation behind the observation of the CMB. Nonetheless, full justice of the entire theory can only be done by careful study of the standard texts [7][8][9][10][11] and several other texts, the reference of which are listed in the text when appropriate.

1.1 The Expanding Universe

The Cosmological Principle is the cornerstone to our modern accepted Cosmological theories, its core concept being that no point or direction in the universe is special. This leads us to accept that our Universe is Homogeneous and Isotropic, that is, the physics and statistics of observed quantities at all points in space and in every direction is equivalent. We must be careful in understanding the scales at which these principles are defined since we see in our daily lives, in our local environment, visible inhomogeneities and anisotropies. The Principle holds up at scales $> 100\,\mathrm{MPc}$ [12].

1.1.1 The Friedmann-Robertson-Walker Metric

The stage for the mathematical framework of modern Cosmological theories is set by the Friedmann-Robertson-Walker (FRW) metric. This is the most general $(3+1)$ dimensional space-time metric that preserves the cosmological principle and causality, and the space part of the metric can be understood to be a 3-sphere embedded in a 4 dimensional space [7]. The FRW metric is

$$\mathrm{d}s^2 = -\mathrm{d}t^2 + a^2(t)\left[\frac{\mathrm{d}r^2}{1-kr^2} + r^2\left(\mathrm{d}\theta^2 + \sin^2\theta\,\mathrm{d}\phi^2\right)\right], \tag{1.1}$$

where (t,r,θ,ϕ) represent the cosmic time and the co-moving space coordinates respectively. The factor $a(t)$ is a time-dependent scaling factor of the spatial sector of (Equation 1.1). k is the intrinsic curvature of the 3-sphere, which by proper scaling assumes either of three integer values $(-1,0,1)$ corresponding to an open, flat or closed Universe respectively.

1.1.2 Distances, Redshifts and Horizons

The coordinate r we see in the FRW metric (Equation 1.1) is not the physical distance between two points but is rather a geometric marker that is fixed between two stationary points in the cosmic frame. The physical distance between two points at time t can be appropriately calculated by the distance covered by a null ray (light) starting at time t_1 from coordinate r and reaching at time t to the observer at $r = 0$ and is given by

$$d_{Phy}(t) = a(t)\int_0^r \frac{\mathrm{d}r}{\sqrt{1-kr^2}} = a(t)\int_{t_1}^t \frac{\mathrm{d}t'}{a(t')}. \tag{1.2}$$

Using the definition of physical distance, we may define a ‘Particle Horizon’, the maximum physical distance any particle can travel from time $t = 0$ to an epoch at time t. In other words this is the distance up to which an event at time t is causally connected. We get this by substituting $t_1 = 0$ in (Equation 1.2). Thus, at our current epoch, this is the furthest we can observe any light ray that started out at the beginning of the Universe. It is given by

$$d_{PH}(t) = a(t)\int_0^t \frac{\mathrm{d}t'}{a(t')}. \tag{1.3}$$

A very important outcome of a changing scale factor $a(t)$ is the shifting of the wavelength of light between a stationary source and observer. This can be calculated very simply by considering a wave of wavelength λ_1 leaving its source at time t_1 and arriving at the observer at time t with a wavelength λ. Using simple calculations of the arrival times of the wave crests we can show that

$$\frac{\lambda}{\lambda_1} = \frac{a(t)}{a(t_1)} = 1 + z. \tag{1.4}$$

We see that for an expanding Universe, the light will be redshifted. We have also defined an important quantity z which measures the fractional change in the wavelength and is termed the 'redshift'. As was first observed by Slipher and Hubble, the galaxies appear to be redshifted the further away they are. Modern probes of the Cosmological distance ladder confirm this and the cosmic expansion is parametrised by the Hubble parameter H. This tells us how fast a galaxy is receding from us per unit separation between us. It is given by

$$H = \frac{\dot{d}_{Phys}}{d_{Phys}} = \frac{\dot{a}}{a}, \tag{1.5}$$

where a $\cdot$ represents a derivative $\mathrm{w.r.t}$ the cosmic time t.

Another distance of interest is the 'Hubble radius', not directly related to any visual horizon, but which will be important in the context of Inflation. It is given by

$$d_{HR}(t) = \frac{1}{aH}. \tag{1.6}$$

1.1.3 Dynamics of the FRW Universe

From the FRW metric (Equation 1.1) we see that the dynamics of the Universe is governed solely by the scale factor $a(t)$. There is overwhelming evidence that we live in an expanding universe that is undergoing an acceleration at our current epoch [13] [14]. To develop the formalism for the dynamics of the Universe we have to plug the FRW metric in the Einstein equation

$$\mathrm{G}_{\mu\nu} = 8\pi G\,\mathrm{T}_{\mu\nu} - \Lambda \mathrm{g}_{\mu\nu}, \tag{1.7}$$

where the term $\mathrm{T}_{\mu\nu}$ is the stress-energy tensor and contains the macroscopic information of the matter and energy distribution of the Universe. Solving (Equation 1.7) for the FRW metric (Equation 1.1) gives us the very important Friedmann equations which together constrain and describe the evolution of the cosmological scale factor $a(t)$. The Friedmann equations can be cast in several forms, one of the most useful being the following two equations,

$$\left(\frac{\dot{a}}{a}\right)^2 = \frac{8\pi G}{3}\rho - \frac{k}{a^2} + \frac{\Lambda}{3}, \tag{1.8a}$$

$$\frac{\ddot{a}}{a} = -\frac{4\pi G}{3}\left(\rho + 3p\right) + \frac{\Lambda}{3}. \tag{1.8b}$$

We note that a, ρ and p are all functions of time. The second equation may be called the acceleration equation. It is easy to see from this equation that to explain the current accelerated expansion of the Universe it is necessary to have a additional term Λ that dominates over the matter density. These equations can be combined to give us the continuity equation,

$$\dot{\rho} + 3\frac{\dot{a}}{a}\left(\rho + p\right) = 0. \tag{1.9}$$

Also, we note that since we have made the critical assumption that the Universe is a dilute gas which behaves ideally, the pressure and density are connected by the equation of state given by

$$p = w\rho. \tag{1.10}$$

Non-relativistic matter, or 'dust' as is often the terminology in cosmology, behaves like a pressure-less fluid with $w = 0$ whereas, a radiation gas has $w = \frac{1}{3}$, and the cosmological constant has $w = -1$. The evolution of the density can be thus cast as a function of the scale factor as,

$$\rho(a) = \frac{1}{a^{3(1+w)}}. \tag{1.11}$$

In an expanding universe, as one goes back in time, the scale factor decreases and for all conceivable matter and energy with $w > -1$, the density increases. This shows that at earlier epochs, the Universe was much denser and which leads to ain initial singularity as the scale factor approaches 0. This is the origin of the 'Big Bang' hypothesis.

To obtain the evolution history of the scale factor a and the matter-energy density ρ we plug the appropriate quantities in the Friedmann equations (Equation 1.8) and solve for a as a function of cosmic time t. Assuming single constituent components such as dust, radiation or the cosmological constant in a flat universe($k = 0$), we get the solutions listed in (Table 1.1),

Constituent	w	$\rho(a)$	$a(t)$	$\rho(t)$	$H(t)$
Dust	0	a^{-3}	$t^{\frac{2}{3}}$	t^{-2}	$\frac{2}{3t}$
Radiation	$\frac{1}{3}$	a^{-4}	$t^{\frac{1}{2}}$	t^{-2}	$\frac{1}{2t}$
Λ	-1	Constant	e^{Ht}	Constant	$\sqrt{\frac{\Lambda}{3}}$

Table 1.1: Evolution of components

In case $k \neq 0$ and when multiple components are present, the solution to the Friedmann equations is not trivial and must be computed numerically. However, throughout the evolutionary history of the universe, one component or the other has dominated and to a good approximation the results in (Table 1.1) are valid over periods of time.

Since the Friedmann equations relate the evolution of the scale factor to the energy and matter density of the Universe, it will be useful to recast the equations in a form that illustrates the contribution of different components. Writing the first equation in (Equation 1.8) in terms of energy densities,

$$\rho = \frac{3H^2}{8\pi \mathrm{G}} \left[1 + \frac{k}{a^2 H^2} - \frac{\Lambda}{3H^2} \right], \tag{1.12}$$

where ρ is the sum of the non-relativistic matter ρ_m and radiation ρ_r, we identify a critical energy density given by,

$$\rho_{crit} = \frac{3H^2}{8\pi \mathrm{G}}. \tag{1.13}$$

This leads us to reformulate the first Friedmann equation in the form

$$\Omega_m + \Omega_r + \Omega_k + \Omega_\Lambda = 1. \tag{1.14}$$

where each term on the $\mathrm{L.H.S}$ is the ratio of the corresponding energy density with the critical energy density.

The most recent measurements of the Hubble parameter H_0 from independent surveys of CMB and type $1a$ supernovae are,

$$H_0 = \begin{cases} 67.27 \pm 0.66 \,\mathrm{km\,s^{-1}\,Mpc^{-1}}, & \text{Planck TT,EE,TE + Low TEB [15]} \\ 73.24 \pm 1.74 \,\mathrm{km\,s^{-1}\,Mpc^{-1}}, & \text{Riess. et.al. 2016 [16]} \end{cases} \tag{1.15}$$

There is clearly a $\sim 3\sigma$ discrepancy in these two measurements which might point to an issue in the $\Lambda\mathrm{CDM}$ model itself or to some systematic effects in either instrument. An increase in

N_{eff}, the effective degrees of freedom of massive neutrinos, gives better consistency but it also leads to an increase of σ_8 [15].

The latest constraint on the matter and dark energy content, curvature, and the dark energy equation of state parameter, from Planck and external datasets combined [15], is illustrated in the following figure.

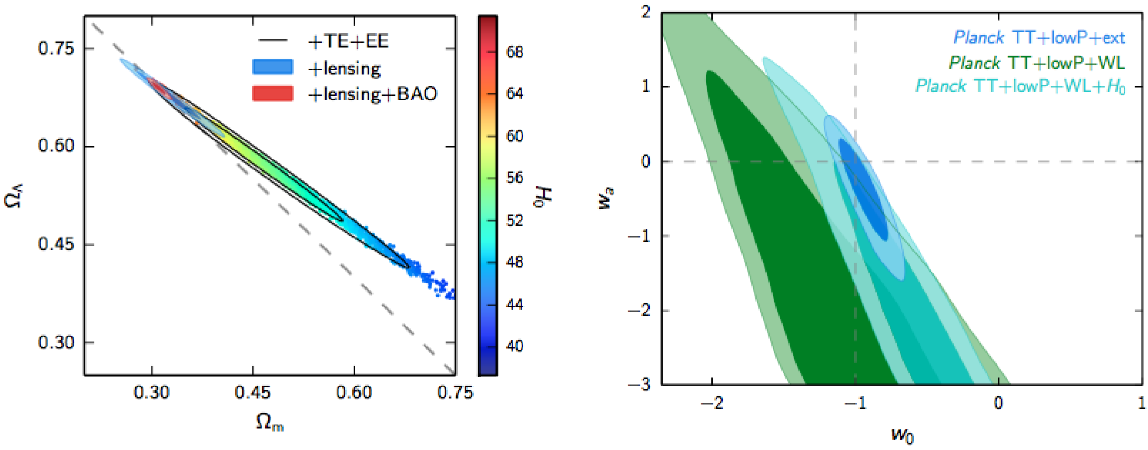

Figure 1.1: The left plot shows the constraints on the Ω_m-Ω_Λ plane from the *Planck* $\mathrm{TT,EE,TE}$ and LowTEB data which is strongly constrained by the addition of lensing reconstruction and BAO data. The right plot shows the constraints on w_0 and w_a, for the popular CPL parametrisation of the dark energy equation of state parameter $w = w_0 + (1-a)w_a$, using *Planck* $+\mathrm{BAO}+\mathrm{JLA}$ data. [15]

The values using the Planck $\mathrm{TT,EE,TE}$ and LowTEB data are:

$$\Omega_m = 0.3117 \pm 0.007, \tag{1.16a}$$

$$\Omega_\Lambda = 0.6881 \pm 0.0065, \tag{1.16b}$$

$$\Omega_k = 0.0002 \pm 0.0021. \tag{1.16c}$$

The equation of state parameter for Λ, using the *Planck* $+\mathrm{lensing}+\mathrm{external}$ datasets is given by,

$$w = -1.019^{+0.075}_{-0.080}, \tag{1.17}$$

which is compatible with vacuum energy, that is, a cosmological constant Λ.

1.2 Thermal History of the Universe and Recombination

It is apparent from the evolution equations for the different components (matter, radiation, Λ) of the Universe, that in a monotonically expanding universe, as we go back in time, the Universe grows denser and hotter. At sufficiently high redshifts before $10^{-10}\mathrm{s}$, when the Universe was hotter than a few TeV, the processes that took place are beyond the energy scales that can be probed by current particle accelerators. After $10^{-10}\mathrm{s}$ had elapsed, some of the key processes that took place are listed in (Figure 1.2).

Different particle species were in thermal equilibrium with the background plasma. During the radiation dominated epoch, the temperature scaled as $aT = \mathrm{const}$. Even when matter started to dominate at redshift $z_{eq} = 3371 \pm 23$ [15], the high relative abundance of photons meant the temperature of the matter-radiation plasma still scaled accordingly. As the Universe expanded and cooled, different species that were in equilibrium with the surrounding thermal bath, 'decoupled' or 'froze out'. Each particle species has a certain reaction rate Γ with the surrounding plasma. The criterion for them to decouple from it is if the mean time between two interactions, Γ^{-1} is much greater that the cosmological time scale, H^{-1}, that is $\Gamma^{-1} \gg H^{-1}$. Beyond this, the reactions are not efficient enough to keep the species in equilibrium.

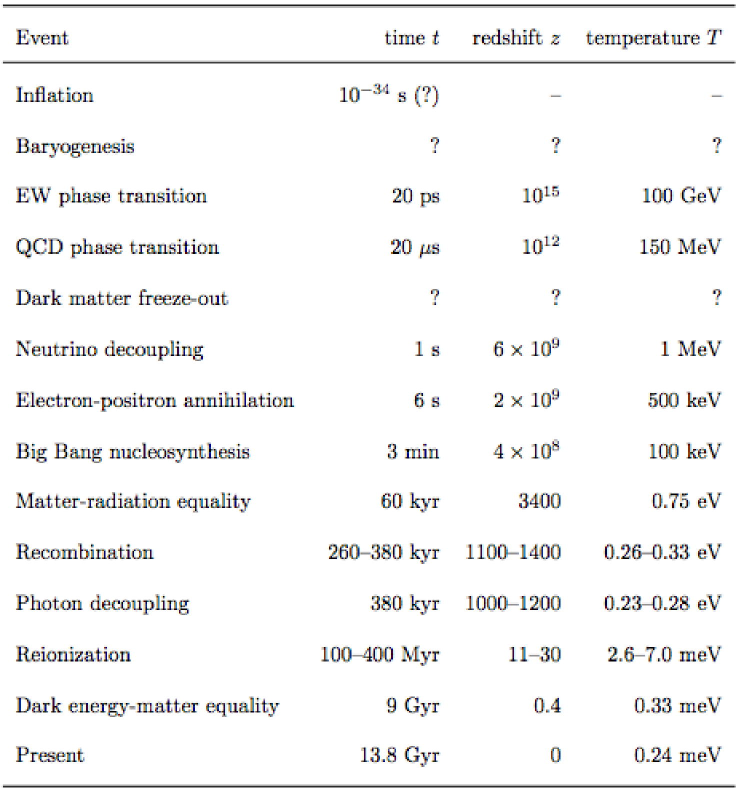

Event	time t	redshift z	temperature T
Inflation	10^{-34} s (?)	–	–
Baryogenesis	?	?	?
EW phase transition	20 ps	10^{15}	100 GeV
QCD phase transition	20 μs	10^{12}	150 MeV
Dark matter freeze-out	?	?	?
Neutrino decoupling	1 s	6×10^{9}	1 MeV
Electron-positron annihilation	6 s	2×10^{9}	500 keV
Big Bang nucleosynthesis	3 min	4×10^{8}	100 keV
Matter-radiation equality	60 kyr	3400	0.75 eV
Recombination	260–380 kyr	1100–1400	0.26–0.33 eV
Photon decoupling	380 kyr	1000–1200	0.23–0.28 eV
Reionization	100–400 Myr	11–30	2.6–7.0 meV
Dark energy-matter equality	9 Gyr	0.4	0.33 meV
Present	13.8 Gyr	0	0.24 meV

Figure 1.2: Table showing some of the key moments in the history of the Universe. (From DAMTP Baumann lecture notes.)

Before the background temperature dropped to the order of an eV, the high relative abundance of photons meant that there were enough high energy photons at the tail end of the Planck spectrum to ionise Hydrogen and Helium. The photons were strongly coupled to the free electrons through Compton scattering, the electrons to the nuclei by Coulomb scattering, and their mean free path was small compared to the Hubble radius. At sufficiently low energies, free electrons and protons recombined to form neutral Hydrogen atoms, an epoch known as 'Recombination', and the free electron density fell sharply. This allowed photons to freely stream through the transparent medium and form the Cosmic Microwave Background Radiation.

The free electron fraction X_e which is the ratio of free electrons to baryons is given by the

Saha equation,

$$\left(\frac{1-X_e}{X_e^2}\right)=\frac{2\zeta(3)}{\pi^2}\eta\left(\frac{2\pi T}{m_e}\right)^{\frac{3}{2}}e^{\frac{B_H}{T}}, \tag{1.18}$$

where, ζ is the Riemann function, η is the baryon to photon ratio and is about 10^{-9} at Recombination, $m_e = 0.51\mathrm{MeV}$ is the rest mass of electrons, $B_H = 13.6\mathrm{eV}$ is the binding energy of Hydrogen, and T is the temperature in energy units. The Saha equation approximately predicts the onset of Recombination but an exact solution of the electron relic density after Recombination is achieved numerically.

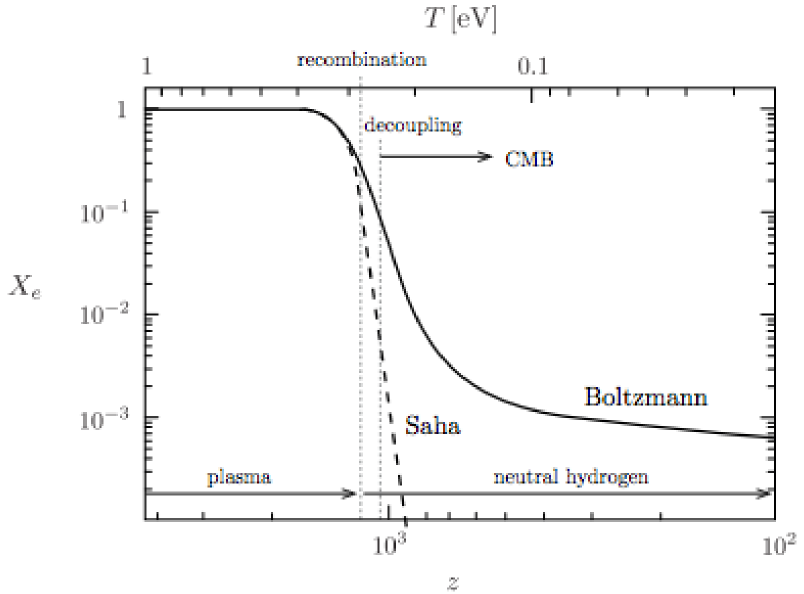

Figure 1.3: The figure shows the evolution of the electron fraction over time, the dashed line being the Saha approximation which correctly predicts the epoch of Recombination, and the solid line is the exact solution. The epochs of Recombination and Decoupling are defined when the electron fraction X_e falls below 0.1 and 0.01 respectively. (Figure from DAMTP Baumann lecture notes.)

The epoch of Recombination is defined when the free electron fraction dropped to 0.1. The temperature, redshift and time at Recombination is given as follows,

$$T_{\mathrm{rec}} \approx 0.3\mathrm{eV} \approx 3500\mathrm{K} \tag{1.19a}$$

$$z_{\mathrm{rec}} \approx 1320 \tag{1.19b}$$

$$t_{\mathrm{rec}} \approx 2.9 \times 10^5\,\mathrm{years} \tag{1.19c}$$

At Recombination, photons are still bound to the remaining free electrons and only decouple from them when the average time between photon-electron scattering falls below H^{-1} and the free electron fraction has fallen to ~ 0.01. This is the epoch of Decoupling and the temperature, redshift and time at this epoch is given as follows,

$$T_{\text{dec}} \approx 0.27\text{eV} \approx 3100\text{K} \tag{1.20a}$$

$$z_{\text{dec}} \approx 1100 \tag{1.20b}$$

$$t_{\text{dec}} \approx 3.8 \times 10^5 \,\text{years} \tag{1.20c}$$

This is the epoch at which the last scattering surface is present.

1.3 Inflation

The scenario presented above for the evolution of the Universe produces two major problems when it comes to reconciling with observational data. These two issues can be summarised as the Horizon and the Flatness Problem. Inflation provides a solution which naturally solves these issues and also acts as a mechanism for production of the initial quantum fluctuations which seeded the young Universe, which we now see in the CMB anisotropies, and later collapsed into the cosmic structures. Let us first look at the issues with the Standard Big Bang Cosmological picture.

1.3.1 Flatness and Horizon Problem

Let us combine the matter and energy density fractions in (Equation 1.14) into a single quantity $\Omega = \Omega_m + \Omega_r + \Omega_\Lambda$, and leaving out the curvature term. We thus have

$$|\Omega - 1| = \frac{k}{a^2 H^2}. \tag{1.21}$$

As mentioned in the previous section, the R.H.S of (Equation 1.21) is small now, and should thus have been much smaller at earlier epochs, since the Hubble radius $(aH)^{-1}$ grows with time in standard cosmological scenarios. If we consider a power law for the scale factor $a(t) = ct^n$, it can be shown for the two cases of matter and radiation dominated epochs, that

$$|\Omega - 1| \propto \begin{cases} (1+z)^{-2}, & \text{RD} \\ (1+z)^{-1}. & \text{MD} \end{cases} \tag{1.22}$$

This implies that at the Planck epoch of around 10^{-43}s we would expect the curvature parameter $|\Omega - 1|$ to approach 10^{-60}. While this is not an issue *a priori*, having a cosmological parameter so ‘fine tuned’ is not physically acceptable since only a slight fluctuation about this value would have caused the Universe to have collapsed or grown exponentially fast soon after its formation.

We had defined the particle horizon previously (Equation 1.3) as the maximum distance null rays can travel from time 0 to any epoch t and at present is given simply by the conformal time τ. We can reformulate the comoving distance as

$$d_{\text{PH}} = \int_0^a \text{d}(\ln a) \left(\frac{1}{aH} \right), \tag{1.23}$$

and, using the same transformation as above we may write,

$$d_{\mathrm{PH}} \propto \begin{cases} (1+z)^{-1}, & \mathrm{RD} \\ (1+z)^{-\frac{1}{2}}. & \mathrm{MD} \end{cases} \tag{1.24}$$

The comoving horizon is then monotonically increasing and at the time of recombination must have been much smaller. Regions of space that were causally disconnected at Recombination are thus not expected to share the same statistics of anisotropies. This however goes against observation, especially that of the CMB, which shows us that the entire observable last scattering surface happens to be homogeneous and shares the same statistics.

1.3.2 Inflation as a Solution to the Flatness and Horizon Problem

The importance of the Hubble radius $(aH)^{-1}$ in the horizon and flatness problem can be appreciated from (Equation 1.21) and (Equation 1.23). The Hubble radius represents the distance between two points in space at a particular epoch which will be in causal contact with each other. Since the Universe has only recently started accelerating, for most part of its history, the Hubble radius has always been increasing and hence was much smaller at earlier epochs. Inflation offers to solve the flatness and horizon problem by proposing that the Hubble radius was much larger at an earlier epoch followed by a phase of decreasing Hubble radius. This naturally solves the flatness problem by pushing the value of $|\Omega - 1|$ close to 0. The effect of a decreasing Hubble radius is illustrated in (Figure 1.4). Regions of space which were within the Hubble radius before Inflation were in causal connection with each other and left it during the phase of Inflation. After Inflation ceased, these regions started coming back into the horizon. Such a scenario was first proposed by Guth, Linde, Starobinsky, Albrecht and Steinhardt [17] [18] [19]. Some reviews on the topic include [8] [20].

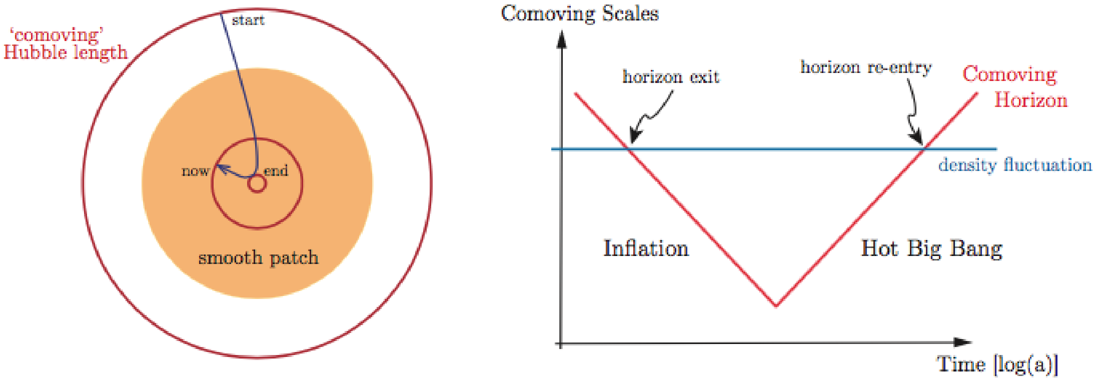

Figure 1.4: Comoving Hubble radius during Inflation. At the onset of inflation, distances larger than the causal horizon today were connected as the Hubble radius was large. Inflation caused the Hubble radius to decrease so that regions of space got causally disconnected. As Inflation ceased, the disconnected regions slowly started to come back into the Horizon. (Figures taken from [8].)

A decreasing Hubble radius may be mathematically stated as

$$\frac{\mathrm{d}}{\mathrm{d}t}\left(\frac{1}{aH}\right) < 0,$$

$$\implies -\frac{\ddot{a}}{(aH)^2} > 0. \tag{1.25}$$

where, for the second equation we have used the Friedmann equations (Equation 1.8). For a Universe not dominated by the cosmological constant, an accelerating universe implies that the equation of state parameter be

$$w < -\frac{1}{3}. \tag{1.26}$$

Another important relation can be obtained from the definition of the Hubble parameter H, giving us,

$$\frac{\ddot{a}}{a} = H^2(1-\epsilon), \tag{1.27}$$

where we have defined ϵ as,

$$\epsilon = -\frac{\dot{H}}{H^2} = -\frac{\mathrm{d}(\ln H)}{\mathrm{d}N} < 1. \tag{1.28}$$

To satisfy the condition of acceleration ϵ must be smaller than 1. We have also defined $\mathrm{d}N$ such that

$$\mathrm{d}N = H\mathrm{d}t = \mathrm{d}(\ln a), \tag{1.29}$$

which measure the number of e-folds N of increase of the scale factor a during Inflation. The number of e-folds can also be taken as the duration of Inflation and to solve the problem of flatness and horizon N should typically be around 60 or larger. This relation also shows that the Hubble parameter changes very slowly with each e-fold.

1.3.3 Mechanism of Inflation

To achieve the conditions, described in the previous section, of a decreasing Hubble radius and a permeating fluid with an equation of state parameter $w < -\frac{1}{3}$, it is customary to introduce a scalar field ϕ. The stress-energy tensor of such a field is given by

$$\mathrm{T}^{\phi}_{\mu\nu} = \partial_\mu\phi\partial_\nu\phi - g_{\mu\nu}\left(\partial^\lambda\phi\partial_\lambda\phi + V(\phi)\right). \tag{1.30}$$

The energy density and pressure can of such a fluid is given by the 00 and ii elements of the stress-energy tensor. This gives us

$$\rho^\phi = \frac{1}{2}\dot{\phi}^2 + V(\phi), \tag{1.31a}$$

$$p^\phi = \frac{1}{2}\dot{\phi}^2 - V(\phi). \tag{1.31b}$$

The condition for acceleration is satisfied when the equation of state parameter is less than

$-\frac{1}{3}$. This implies that the potential energy term must dominate over the kinetic energy term

$$\frac{1}{2}\dot{\phi}^2 < V(\phi). \tag{1.32}$$

The equation of motion of the field ϕ can be calculated from minimising the action given by

$$S = \int \mathrm{d}^4x\sqrt{-g}\left[\frac{1}{2}R + \frac{1}{2}g^{\mu\nu}\partial_\mu\phi\,\partial_\nu\phi - V(\phi)\right], \tag{1.33}$$

where the first part is the Einstein-Hilbert action and the remaining part is due to the scalar field ϕ. Minimising this $\mathrm{w.r.t}$ ϕ gives us

$$\ddot{\phi} + 3H\dot{\phi} + V_{,\phi} = 0. \tag{1.34}$$

This equation resembles a simple harmonic oscillator with a friction term $3H\dot{\phi}$ and a forcing term $V_{,\phi}$. So, as the universe accelerates with increasing H, it puts up more and more resistance to the ϕ field. In a flat Universe, the Friedmann equations can be cast as follows.

$$H^2 = \frac{8\pi G}{3}\rho^{\phi} = \frac{8\pi G}{3}\left(\frac{1}{2}\dot{\phi}^2 + V(\phi)\right), \tag{1.35a}$$

$$\dot{H} + H^2 = -\frac{4\pi G}{3}\left(\rho^{\phi} + 3p^{\phi}\right) = -\frac{8\pi G}{3}\left(\dot{\phi}^2 - V(\phi)\right). \tag{1.35b}$$

1.3.4 Slow-Roll Inflation

We rewrite the conditions for inflation in terms of the quantities derived in the previous section. The parameter ϵ can be recast, using the Friedmann equations (Equation 1.35), as

$$\epsilon = \frac{3}{2}\left(1 + w^{\phi}\right). \tag{1.36}$$

Accelerated expansion is sustained, as we have defined before, when the kinetic energy term is subdominant to the potential energy term. In the case

$$\dot{\phi}^2 << V(\phi), \tag{1.37}$$

the equation of state parameter $w^{\phi} \to -1$ and corresponds to a de Sitter solution for the evolution of the scale factor. To ensure that acceleration is sustained for a sufficiently long time to resolve the flatness and horizon problems, we require that the parameter ϵ also vary slowly with changing e-folds. We define a new parameter η and say that it should also be small.

$$\eta = \frac{\mathrm{d}(\ln\epsilon)}{\mathrm{d}N} = \frac{\dot{\epsilon}}{H\epsilon}. \tag{1.38}$$

The Hubble slow-roll parameters ϵ and η can be redefined in terms of the inflation potential to give the potential slow-roll parameters ϵ_V and η_V.

(1.39a) $$\epsilon_V = \frac{1}{16\pi G}\left(\frac{V_{,\phi}}{V}\right)^2,$$

(1.39b) $$|\eta_V| = \frac{1}{8\pi G}\left(\frac{V_{,\phi\phi}}{V}\right).$$

In the regime of slow-roll inflation, both potential slow-roll parameters are small in order to have a sustained phase of acceleration.

(1.40) $$\epsilon_V, |\eta_V| << 1,$$

and the background evolution in terms of the inflation potential is given by

(1.41a) $$H^2 \approx \frac{1}{3}V(\phi) \approx Constant,$$

(1.41b) $$\dot{\phi} \approx -\frac{V_{,\phi}}{3H},$$

and the scale factor behaves like in the de Sitter case

(1.42) $$a(t) \propto e^{Ht},$$

implying an accelerated phase of expansion.

The potential slow-roll parameters are related to the Hubble slow-roll parameters as

(1.43a) $$\epsilon \approx \epsilon_V,$$

(1.43b) $$\eta \approx \eta_V - \epsilon_V.$$

Inflation comes to an end when the slow-roll conditions are violated, and is given by the conditions

(1.44a) $$\epsilon(\phi_{\text{end}}) = 1,$$

(1.44b) $$\epsilon_V(\phi_{\text{end}}) \approx 1.$$

This happens as the inflation potential steepens and the inflaton, the inflation field, picks up enough kinetic energy to equal the potential energy and break the slow-roll condition.

Inflation, very elegantly, solves the issues of flatness and horizons as well as it redshifts away unwanted relics such as topological defects and monopoles which are not observed in the present Universe. However, it will do the same for any radiation or matter that might be present and will redshift it away to nothing, leaving behind the inflaton field as the primary source of the energy density. A primary concern is then how does the Universe acquire the matter and radiation density of which we are made of. The solution to this is theorised to be a process known as 'Reheating' which occurs as inflation ends and the inflaton field oscillates at the bottom of the potential $V(\phi)$ (for most models). The inflaton field undergoes a damped oscillation, decays into the particles of the standard model and commences the Hot Big Bang phase of the Universe.

1.3.5 Production of Initial Perturbations and its Statistics

The formalism of Inflation developed so far only considers the evolution of the mean of the inflaton field ϕ. Identifying the quantum nature of the inflaton field, we expect there to be quantum fluctuations $\delta\phi$ about the mean. This leads to Inflation ending at different times at different places and hence imparting a density fluctuation $\delta\rho(t,x)$ on the matter and radiation density.

The inhomogeneities imprinted on the CMB are of the order of 1 in 10^5. Since gravity attracts and makes inhomogeneities grow, the fluctuations must have been smaller early on. We thus proceed with a linear perturbation of all the quantities, the energy densities and the metric, about their mean values. This section does not attempt to give a detailed treatment of the topic and is based on the text [8].

The line element for the flat FRW metric, under a linear perturbation of the metric, can be represented in the form,

$$\mathrm{d}s^2 = -(1+2\Phi)\mathrm{d}t^2 + 2aB_i\mathrm{d}x^i\mathrm{d}t + a^2\left[(1-2\Psi)\delta_{ij} + E_{ij}\right]\mathrm{d}x^i\mathrm{d}x^j, \tag{1.45}$$

where we have made a convenient decomposition of the perturbation terms into scalar, vector and tensor quantities defined as

$$B_i = \partial_i B - S_i, \tag{1.46a}$$

$$E_{ij} = 2\partial_{ij}E - \partial_i F_j - \partial_j F_i + h_{ij}. \tag{1.46b}$$

Φ, Ψ, E and B are scalar fields, S_i and F_i are divergence-less vector fields and h_{ij} is a symmetric trace-less tensor field. The convenience of this decomposition lies in the fact that these fields (X represents any of the above) can be decomposed into their Fourier modes

$$X_k(t) = \int \mathrm{d}x^3 X(t,\boldsymbol{x})e^{-i\boldsymbol{k}.\boldsymbol{x}}, \tag{1.47}$$

and the different Fourier modes do not interact with each other under linear conditions.

Perturbing the density and pressure field about the mean background gives

$$\delta\rho(t,\boldsymbol{x}) = \rho(t,\boldsymbol{x}) - \bar{\rho}(t), \tag{1.48a}$$

$$\delta p(t,\boldsymbol{x}) = p(t,\boldsymbol{x}) - \bar{p}(t). \tag{1.48b}$$

The quantities so defined are not all gauge independent, meaning that under certain coordinate transformations, these quantities will change giving rise to spurious modes. The physical nature of any perturbation can thus be understood by constructing quantities that are gauge invariant. Only the quantity h_{ij} is gauge invariant. One of the gauge invariant quantities, constructed out of the ones defined above, that is of interest to us is

$$\mathfrak{R} = \Psi - \frac{H}{\bar{\rho}+\bar{p}}\delta q, \quad \text{Comoving curvature perturbation.} \tag{1.49}$$

To obtain the dynamical equations of these perturbations, we plug the perturbed metric (Equation 1.45) and the stress-energy tensor into the Einstein equation and solve for them. As noted, the SVT decomposition allows the Fourier modes of the fluctuations to not mix with each other. The solution of the Einstein equation for the scalar and tensor Fourier modes is given by the Mukhanov equation which has two counterparts, one for the scalar perturbation and one for the tensor perturbation.

$$v_k'' + \left(k^2 - \frac{z''}{z}\right) v_k = 0, \tag{1.50}$$

where we have made the substitutions

$$v_k = \begin{cases} a h_k, & \text{tensor} \\ z\mathfrak{R}_k, & \text{scalar} \end{cases} \tag{1.51a}$$

$$z^2 = \begin{cases} a^2, & \text{tensor} \\ a^2 \dfrac{\dot{\phi}^2}{H^2} = 2a^2\epsilon, & \text{scalar} \end{cases} \tag{1.51b}$$

and we have set the Planck mass $M_{\rm Pl} = (8\pi G)^{-\frac{1}{2}} = 1$ and $'$ represents a derivative $\mathrm{w.r.t}$ the conformal time τ where $a\mathrm{d}\tau = \mathrm{d}t$.

The Mukhanov equations are in general solvable numerically. In the slow roll approximation we get some intuition. As a mode with a comoving wavenumber leaves the shrinking Hubble horizon $(k < aH)$, the amplitude of the mode freezes and is given by its value at horizon crossing.

In a statistically isotropic and homogeneous Universe where the fluctuations are Gaussian in nature, all information is contained in the 2-point correlation function. In $k-\text{space}$, the primordial power spectra of the scalar and tensor modes generated by Inflation are almost scale invariant. After putting back in the Planck mass $M_{\rm Pl}$ they are

$$\triangle_s^2(k) = \triangle_{\mathfrak{R}}^2(k) = \frac{1}{8\pi^2}\frac{H^2}{M_{\rm Pl}}\frac{1}{\epsilon}\Big|_{k=aH} \quad , \tag{1.52a}$$

$$\triangle_t^2(k) = 2\,\triangle_h^2(k) = \frac{2}{\pi^2}\frac{H^2}{M_{\rm Pl}}\Big|_{k=aH} \quad , \tag{1.52b}$$

The primordial power spectra are parametrised by an amplitude A and a spectral index n

$$\triangle_s^2(k) = A_s(k_*)\left(\frac{k}{k_*}\right)^{n_s(k_*)-1+\frac{1}{2}\alpha_s(k_*)\ln\left(\frac{k}{k_*}\right)} , \tag{1.53a}$$

$$\triangle_t^2(k) = A_s(k_*)\left(\frac{k}{k_*}\right)^{n_t(k_*)} , \tag{1.53b}$$

where, k_* is an arbitrary reference or 'pivot scale'. Notice that for historical reasons the convention for defining the scalar spectral index is $n_s - 1$. The scalar power spectrum is parametrised using an additional parameter called the 'running' α_s which quantifies the rate of change of spectral index with $\ln k$.

The amplitude of the tensor fluctuations is often normalised relative to the scalar fluctuation amplitude. We can define a tensor to scalar ratio r as

$$r = \frac{\triangle_t^2}{\triangle_s^2} = 16\epsilon\Big|_{k=aH} \quad , \tag{1.54}$$

The energy scale of Inflation is directly linked to r as

$$V^{\frac{1}{4}} \sim \left(\frac{r}{0.01}\right)^{\frac{1}{4}} 10^{16}\mathrm{GeV}. \tag{1.55}$$

In the slow-roll approximation, the scalar and tensor spectra, their spectral indices and the tensor to scalar ratio are given by

$$\triangle_s^2 \approx \frac{1}{24\pi^2}\frac{V}{M_{\rm Pl}^4}\frac{1}{\epsilon_V}, \tag{1.56a}$$

$$\triangle_t^2 \approx \frac{2}{3\pi^2}\frac{V}{M_{\rm Pl}^4}\frac{1}{,} \tag{1.56b}$$

$$n_s - 1 = 2\eta_V - 6\epsilon_V, \tag{1.56c}$$

$$n_t = -2\epsilon_V, \tag{1.56d}$$

$$r = 16\epsilon_V, \tag{1.56e}$$

all these quantities being calculated at the horizon crossing $k = aH$.

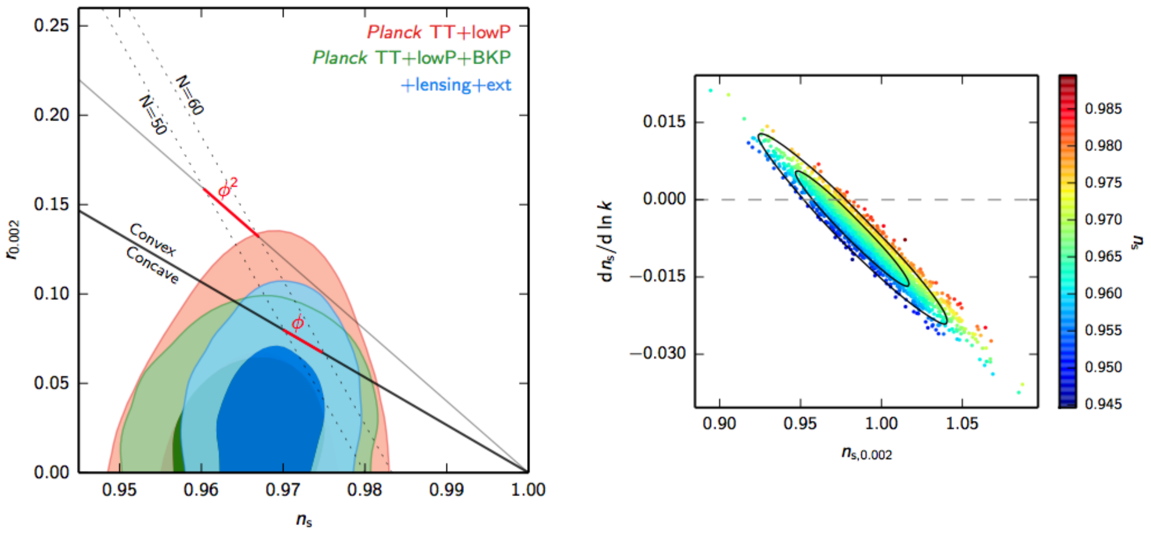

Figure 1.5: *Left*: The joint constraint on the tensor to scalar ratio r and the scalar spectral index n_s, from a joint *Planck* and BICEP analysis, assuming a base CDM model with r as an additional parameter. *Right*: This figure shows the constraints on the running of the spectral index. This is done by adding running as an additional parameter and taking $r = 0$ over a base ΛCDM model. (Figures taken from [15].)

At present, the best constraints on some of the Inflationary parameters have been obtained by the Planck satellite with the addition of external datasets such as the BICEP/Keck [15] [21]. The scalar spectral index provides a slight red tilt to the scalar power spectrum. A definitive measurement of the tensor to scalar ratio has not been possible yet and only upper limits are provided on r

(1.57a) $$n_s = 0.968 \pm 0.006,$$

(1.57b) $$r < 0.09, \quad 95\%\mathrm{CL},$$

(1.57c) $$\frac{\mathrm{d}n_s}{\mathrm{d}\ln k} = -0.0065 \pm 0.0076.$$

1.4 Imprints on the CMB : Anisotropies

As the inflationary phase comes to an end, it leaves behind an almost scale independent density fluctuation on the matter and radiation in the Universe, as well as an expected background of almost scale independent gravitational waves. The density fluctuations at different length scales remain frozen as long as their corresponding comoving modes k are outside the horizon $(k < aH)$. After the end of Inflation, the Hubble radius starts to increase, progressively more and more modes enter the horizon and are able to evolve. Starting with the smallest scales first, the gravitational pull of baryonic and dark matter and pressure from the radiation density undergoes a balancing act. Gravity causes over-dense regions to collapse and radiation pressure opposes it. Moreover, the baryonic matter is strongly coupled to the radiation field through Compton scattering. This interplay between the different components, set up on an expanding FRW frame, gives rise to standing waves in the hot plasma that evolve over time. At the epoch of 'Decoupling', the radiation is free to stream through the newly transparent Universe and forms the Cosmic Microwave Background radiation. Having been in thermal equilibrium with the baryonic matter, the CMB radiation carries an imprint of the density fluctuations at the last scattering surface and hence acts as a direct probe of the physical processes that led to the production of these fluctuations. Discussions on which this section is based are [9] [22].

1.4.1 Primary Temperature Anisotropies

The primary CMB anisotropies are those that are intrinsic to the last scattering surface that were produced by physical processes leading up to and during last scattering. The primary temperature anisotropies predominantly evolved from the primordial scalar fluctuations $\mathfrak{R}$ and can be explained by three physical processes:

- The intrinsic temperature variation on the last scattering surface.
- The Sachs-Wolfe effect [23], which describes the gravitational red and blue-shifting of photons as they leave the gravitational potential well of the matter over and under-densities at the last scattering surface.
- Doppler shift due to the bulk motion of the baryonic matter at the last scattering surface.

Schematically, the anisotropies may be described by a scalar field Θ_{tot}, equal to the temperature anisotropies of the CMB radiation at the last scattering surface.

(1.58) $$\Theta_{\text{tot}} = \frac{\triangle T}{T} = [(\Psi + \Theta) - \hat{\mathbf{r}} \cdot \boldsymbol{v}]\Big|_{\tau=\tau_{\text{dec}}},$$

where, Θ is due to the baryonic density fluctuation, Ψ is the Newtonian gravitational potential and $\boldsymbol{v}$ is the velocity field of the bulk baryonic matter. These quantities have all been calculated at the last scattering surface $\tau = \tau_{\text{dec}}$. It is most convenient to work with the Fourier modes of these quantities as in the linear theory, each of the $k-\text{modes}$ evolve independently.

To determine the evolution of the modes that have re-entered the horizon we have to solve the complete set of equations of the perturbation theory. For the non-relativistic species these are the continuity equation, the Euler equation and the Poisson equation, and for the relativistic species it is the Boltzmann equation.

After the end of Inflation and before Decoupling, there were two distinct regimes, a radiation dominated one and a matter dominated one where the scale factor a evolved differently as given in (Table 1.1). We assume that the matter content is mostly composed of Cold Dark Matter(CDM) whose perturbation evolution is given by

$$\ddot{\delta}_{\text{CDM}} + 2\frac{\dot{a}}{a}\dot{\delta}_{\text{CDM}} - 4\pi G\bar{\rho}\delta_{\text{CDM}} = 0, \tag{1.59}$$

where δ_{CDM} is the CDM density perturbation and $\bar{\rho}$ is the mean density of the CDM. Since the CDM does not interact electromagnetically, the only forcing term is gravity. During the radiation dominated epoch, $\bar{\rho}$ is small and δ does not grow. In the matter dominated epoch, the solutions are $\delta_{\text{CDM}} \propto t^{\frac{2}{3}}$ and $\delta_{\text{CDM}} \propto t^{-1}$. The growing mode solution implies the gravitational potential Ψ is time independent.

The photon and ionised baryonic fluid are tightly coupled together by means of Compton scattering. Due to the strong coupling, its velocity field v_B, temperature T and the photon phase-space distribution function f_γ are completely determined by the baryonic density fluctuation δ_B. Θ is related to the baryonic density fluctuation by

$$\Theta(t) = \frac{1}{3}\delta_{\text{B}}(t). \tag{1.60}$$

Using units in which $c = 1$, the dynamics of the photon-baryon fluid for each individual k-mode is given by

$$\frac{\text{d}}{\text{d}\tau}\left[(1+R)\dot{\Theta}\right] + \frac{k^2}{3}\Theta = -\frac{k^2}{3}(1+R)\Psi, \tag{1.61}$$

where, $R = \frac{3\rho_B}{4\rho_\gamma}$ is the ratio of the baryon and photon energy density. This is the differential equation for a simple harmonic oscillator with a driving term on the right that is purely gravitational. It leads to a plane-wave solution for each Fourier mode propagating through the photon-baryon medium with a particular sound speed. Starting off with a flat spectrum at time $\tau = 0$, the oscillations evolve into a harmonic series of acoustic peaks corresponding to modes that were at their extremum at τ_{dec}. The Doppler shift due to the bulk motion $\boldsymbol{v}$ of the plasma has a plane wave solution too that is subdominant in amplitude and is out of phase by $90°$ in time and space with the other two effects.

The phenomenon of “Silk damping” is related to the thickness of the transition between the strongly coupled phase to the free-streaming of photons during Decoupling. Modes that were on scales smaller than the thickness of the last scattering surface get damped.

The temperature anisotropies measured on the sky are not computed in the Fourier space but in the real space as a function of the position $\hat{\text{n}}$ on the sphere. The temperature anisotropy field can be decomposed in the basis of the spherical harmonics

$$\frac{T(\hat{\mathrm{n}})-T_0}{T_0} = \frac{\triangle T(\hat{\mathrm{n}})}{T_0} = \sum_{lm} a_{lm} Y_{lm}(\hat{\mathrm{n}}),$$
$$a_{lm} = \int \mathrm{d}\Omega Y_{lm}(\hat{\mathrm{n}})^* \left(\frac{\triangle T(\hat{\mathrm{n}})}{T_0}\right). \tag{1.62}$$

If a_{lm} is a Gaussian random variable, as is predicted from Inflation, the information content is contained in the power spectrum

$$C_l^{TT} = \frac{1}{2l+1}\sum_m \langle a_{lm}^* a_{lm} \rangle \tag{1.63}$$

This is what is measured when we observe the CMB sky hence we want to translate the fluctuations we see in the $k-\mathrm{space}$ to the anisotropies in the $l-\mathrm{space}$. To obtain the primary anisotropies on the CMB, in the harmonic space, we project the fluctuations in $k-\mathrm{space}$ at the last scattering surface to $l-\mathrm{space}$. The projection operator is obtained by the Bessel function $j_l(kD_*)$, where $D_* = \tau_0 - \tau_*$ is the distance from us to the last scattering surface, a $(\ldots)_*$ meaning it's value at the last scattering surface, and the anisotropies are given by

$$a_l(k) = \Theta_{\mathrm{tot}}(\tau_*) j_l(kD_*) \tag{1.64}$$

This gives us the temperature anisotropy power spectrum in terms of the primordial inflationary power spectrum as

$$C_l^{TT} = 4\pi \sum_{lm} Y_{lm}(\hat{\mathrm{n}}) \left[(-i)^l \int \frac{\mathrm{d}^3 k}{(2\pi)^3} a_l(k) Y_{lm}^*(\hat{\mathrm{k}})\right] \tag{1.65}$$

The Bessel function $j_l(kD_*)$ is strongly peaked at $kD_* \approx l$ and hence most of the power in the mode k is mapped to its corresponding mode in l.

In an expanding FRW frame, the potential well of the intervening matter over-densities decay over time and this becomes more pronounced during an accelerating dark energy dominated phase, as it is at the present epoch. The CMB photons that traverse these potential wells see a shallower potential well coming out than when falling into it leading to an energy boost. This is known as the “Sachs-Wolfe effect”. The change in the temperature is quantified by integrating this effect along the line of sight from the last scattering surface to us and is given by

$$\left(\frac{\triangle T}{T}\right)_{\mathrm{ISW}} = \int \left[\dot{\Psi}(\tau) - \dot{\Phi}(\tau)\right] \mathrm{d}\tau, \tag{1.66}$$

where, Φ and Ψ have their usual meaning.

Close to the Decoupling epoch the CMB also undergoes an early ISW effect. This is due to the fact that the radiation energy density is non-negligible after Decoupling and radiation pressure damps any fluctuation of the potential that enter the horizon, well into the matter dominated epoch. The effect is on the large scales corresponding to modes which oscillate on time scales comparable to the potential decay time.

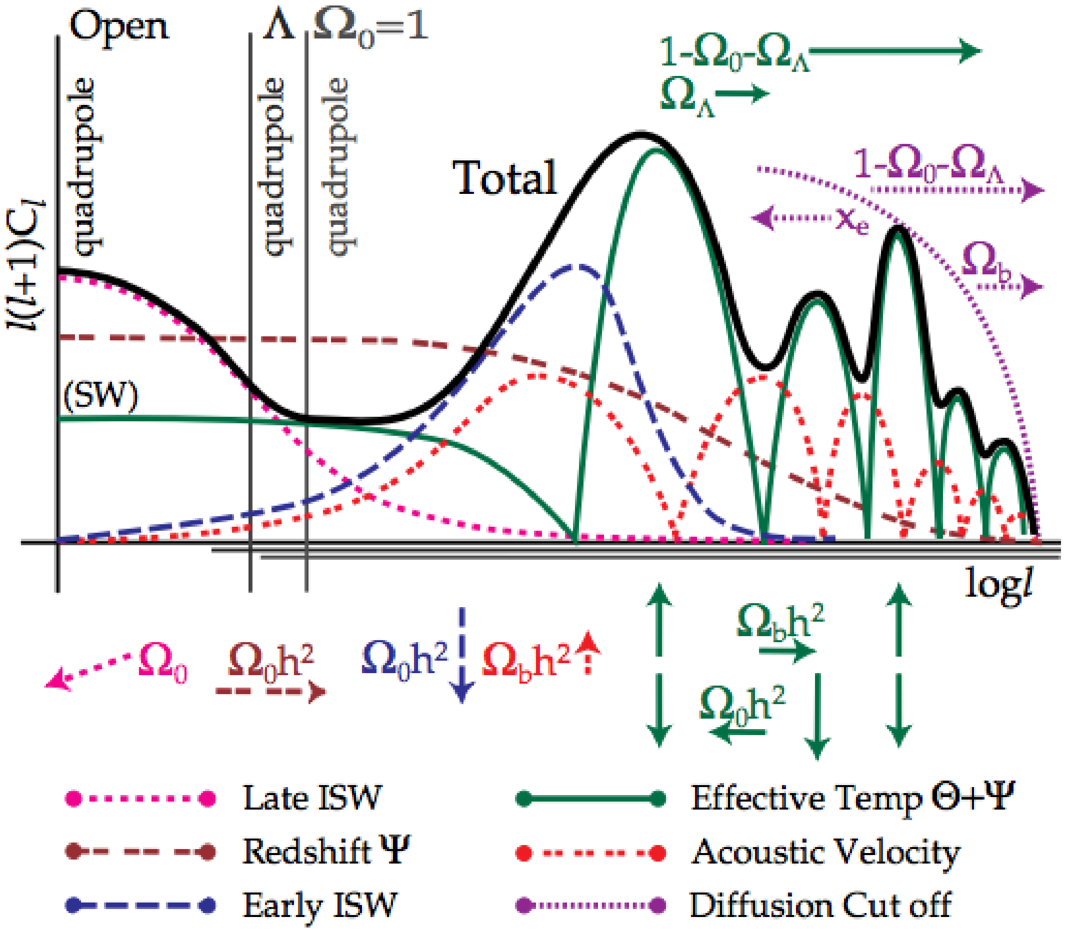

Figure 1.6: The figure shows how the different processes contribute to the temperature power spectrum. The acoustic peaks (green) are given by the perturbations in the matter density fluctuations and the gravitational potential, also showing the Sachs-Wolfe plateau at low multipoles. The bulk velocity (dashed red) produces fluctuations which are subdominant and out of phase by 90° to the previous process. The Late ISW (dashed pink) shows a significant contribution at the low multipoles and the diffusion damping (Silk damping) envelope (dotted pink) shows the suppression of power at high multipoles. (Figure taken from [24].)

1.5 Polarisation of the CMB

The CMB radiation, as shown above, encodes the information of the matter density fluctuation and the bulk velocity at the last scattering surface in the temperature power spectrum and thus acts as a direct probe of the physical processes that take place before Decoupling. Compton scattering of photons with the free electrons partially polarises the CMB and the polarisation signal contains additional information. Most importantly, the production of gravitational waves from the Inflationary epoch are expected to produce a distinct signature on the CMB polarisation and is therefore the most powerful probe to test the parameters of Inflation and differentiate between different models that produced the primordial fluctuations.

1.5.1 Representation of Polarisation

In the previous section we have described how the temperature anisotropy field, given by a scalar quantity as a function of position on the sky, can be decomposed in a basis of spherical harmonics. The complete radiation field, including intensity and polarisation, can be represented in the basis of the Stokes parameters (I, Q, U, V) [25]. The Stokes V parameter is not known to be generated by any processes relevant to the CMB and hence will be dropped. Unlike the scalar I, the Stokes parameters Q and U are dependent on the local reference frame at the point of measurement, and hence, we wish to perform a linear transformation to quantities which are scalar and invariant upon rotation of the local coordinate frame. Upon a rotation by an angle ψ, the Q and U Stokes parameters transform as,

$$(Q \pm iU)' = e^{\mp 2i\psi}(Q \pm iU) \tag{1.67}$$

The quantity $(Q \pm iU)$ is thus a spin-2 quantity and must be decomposed in a basis of spin weighted spherical harmonics. We can thus decompose all three Stokes parameters in the following manner,

$$(Q \pm iU)(\hat{\mathrm{n}}) = \sum_{l}\sum_{m} a_{\pm 2,lm}\, {}_{\pm 2}Y_{lm}(\hat{\mathrm{n}}) \tag{1.68}$$

where, Y_{lm} and ${}_{\pm 2}Y_{lm}$ are the spherical harmonic functions and the spin-weighted harmonic functions respectively. The harmonic coefficients can be easily obtained from (Equation 1.67) by employing the orthogonality property of the harmonic functions,

$$a_{2,lm} = \left[\frac{(l+2)}{(l-2)}\right]^{-\frac{1}{2}} \int \mathrm{d}\Omega\, Y^{*}_{lm}(\hat{\mathrm{n}})\,\bar{\eth}^{2}(Q + iU)(\hat{\mathrm{n}}) \tag{1.69a}$$

$$a_{-2,lm} = \left[\frac{(l+2)}{(l-2)}\right]^{-\frac{1}{2}} \int \mathrm{d}\Omega\, Y^{*}_{lm}(\hat{\mathrm{n}})\,\eth^{2}(Q - iU)(\hat{\mathrm{n}}) \tag{1.69b}$$

where, $\eth$ and $\bar{\eth}$ are raising and lowering operators of the harmonic functions as given in [26]. We now define a linear combination of these harmonic coefficients as follows,

$$a_{E,lm} = -\frac{1}{2}\left(a_{2,lm} + a_{-2,lm}\right) \tag{1.70a}$$

$$a_{B,lm} = -\frac{i}{2}\left(a_{2,lm} - a_{-2,lm}\right) \tag{1.70b}$$

These quantities behave differently under a parity transformation. E remains unchanged and B reverses sign.

If the fluctuations on the CMB sky are Gaussian, the statistics of these fluctuations can be characterised completely by the two point correlation functions and hence by their harmonic transforms, the power-spectra. Four non-vanishing spectra can be constructed from the quantities defined above

$$C^{EE} = \frac{1}{2l+1}\sum_m \left\langle a^*_{E,lm} a_{E,lm} \right\rangle, \tag{1.71a}$$

$$C^{BB} = \frac{1}{2l+1}\sum_m \left\langle a^*_{B,lm} a_{B,lm} \right\rangle, \tag{1.71b}$$

$$C^{TE} = \frac{1}{2l+1}\sum_m \left\langle a^*_{T,lm} a_{E,lm} \right\rangle, \tag{1.71c}$$

with the fourth spectrum C^{TT} defined earlier. When the polarisation amplitude is represented on the sky using 'rods' of a given magnitude P at a certain orientation α, in the local coordinate system, they are defined as

$$P = \sqrt{Q^2 + U^2}, \tag{1.72a}$$

$$\alpha = \frac{1}{2}\tan^{-1}\left(\frac{Q}{U}\right), \tag{1.72b}$$

1.5.2 Thomson Scattering of Photons

The Thomson scattering is the low energy limit of Compton scattering and is the principal scattering mechanism at the last scattering surface. Qualitatively, the process of Thomson scattering re-emits polarised radiation from incident unpolarised radiation that is direction dependent. An anisotropic radiation field, such as was present at the last scattering surface, would thus create a net polarisation in the direction of the observer. To quantify the polarisation of the radiation we consider the Stokes (I, Q, U) parameters. In the rest frame of the electron, the Stokes parameters of the scattered radiation due to an anisotropic field of incident unpolarised radiation are given by [27]

$$I_{\rm sca} = \frac{3\sigma_{\rm T}}{16\pi\sigma}\int d\Omega(1+\cos^2\theta)I_{\rm inc}(\theta,\phi), \tag{1.73a}$$

$$Q_{\rm sca} = \frac{3\sigma_{\rm T}}{16\pi\sigma}\int d\Omega\sin^2\theta\cos(2\phi)I_{\rm inc}(\theta,\phi), \tag{1.73b}$$

$$U_{\rm sca} = -\frac{3\sigma_{\rm T}}{16\pi\sigma}\int d\Omega\sin^2\theta\sin(2\phi)I_{\rm inc}(\theta,\phi), \tag{1.73c}$$

where, $\sigma_{\rm T}$ is the Thomson scattering cross-section. Decomposing the incident radiation into its spherical harmonic components, the scattered Stokes (I, Q, U) can be restated as

$$I_{\rm sca} = \frac{3\sigma_{\rm T}}{16\pi}\left[\frac{8}{3}\sqrt{\pi}a_{00} + \frac{4}{3}\sqrt{\frac{\pi}{5}}a_{20}\right], \tag{1.74a}$$

$$Q_{\rm sca} = \frac{3\sigma_{\rm T}}{4\pi}\sqrt{\frac{2\pi}{15}}{\rm Re}(a_{22}), \tag{1.74b}$$

$$U_{\rm sca} = -\frac{3\sigma_{\rm T}}{4\pi}\sqrt{\frac{2\pi}{15}}{\rm Im}(a_{22}), \tag{1.74c}$$

where a_{22} is the spin-2 quadrupole coefficient in the harmonic decomposition of the incident radiation field $I_{\rm inc}$. Thus we see that an incident field of unpolarised radiation produces polarised radiation if the electron, in its rest frame, sees a quadrupole anisotropy in the incident radiation. It's also to be noted that only the $m = \pm 2$ quadrupole moment, which coincide with anisotropies in the plane orthogonal to the direction of the observer, produce a net polarisation. Along the line of sight of the observer, the net effect will be determined by how each type of quadrupole anisotropy $(m = 0, \pm 1, \pm 2)$ project onto $m = 2$. A review of CMB polarisation, relevant for this and the next subsection is given in [28].

1.5.3 Sources of Quadrupole

The CMB photons that travel to us from the last scattering surface are polarised by quadrupolar anisotropies in the radiation field the electron sees in its rest frame. The different ways such a quadrupole can be generated are listed below.

- Scalar : The scalar modes are related to the perturbations in the density field that were shown previously. As the electron-photon fluid is accelerated towards an over-density, it sees the radiation field in the radial direction being redshifted away from it whereas in the perpendicular direction it sees a blue-shifting. This leads to the electron, in its rest frame, seeing a quadrupole anisotropy. Considering the line of sight from the electron at the last scattering surface to us, the net polarisation pattern is radial to the over-density. The converse happens when the electron comes out of an under-dense region and the net polarisation is oriented tangentially to the under-density.

- Vector : The vector perturbations give the velocity field a divergence-free but non-zero curl component. Vector modes are expected to decay very fast, so at the time of last scattering they are not expected to have any contribution.

- Tensor : The tensor modes are related to the metric perturbations during Inflation leading to the production of gravitational waves. As gravitational waves pass through the plasma they cause a compression and rarefaction in orthogonal directions leading to the formation of quadrupolar anisotropies in the rest frame of the electron. Depending upon the polarisation state of the gravitational wave, it produces a curl-like feature in the polarisation vector field on the sky as well as the type of pattern describes for scalar modes.

The polarisation patterns described above are illustrated in (Figure 1.7). The two classes of patterns are known as the E and B modes and are produced by different sources of anisotropies. These are directly related to the anisotropies $a_{E,lm}$ and $a_{B,lm}$ and hence provide a convenient method of probing the source of the perturbations. Tensor perturbations produce both E and B mode polarisation as well as contribute sub dominantly to the temperature anisotropies. However, scalar perturbations can only produce E mode polarisation and temperature anisotropies. *Ab initio*, the scalar and tensor perturbations were produced by inflation, thus observation of primordial B-modes are currently the best method of probing the physics and energy scale of Inflation.

1.6 Late time Cosmology with the CMB

The CMB photons that have been freed from the strong coupling with the ionised baryonic matter at the last scattering surface have been travelling to us for the rest of the history of the

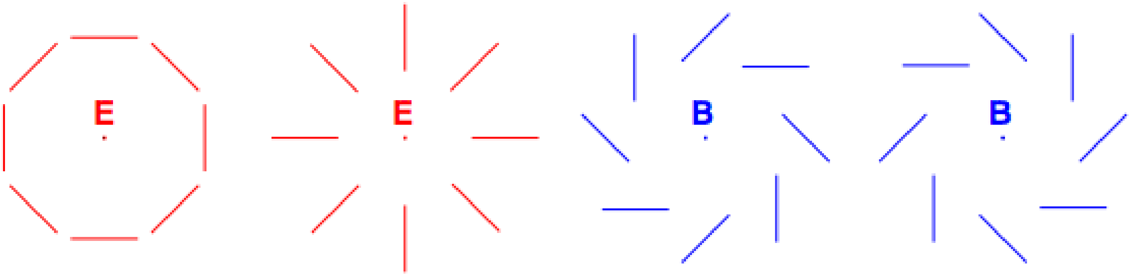

Figure 1.7: The polarisation patterns created by different sources of quadrupolar anisotropy seen by the electrons at the last scattering surface. The E modes are a curl-free pattern, generated by both scalar and tensor perturbations while the B modes are a divergence-free pattern, flipping under a parity transformation, produced by tensor perturbations that are due to primordial gravitational waves. (Figure taken from [29].)

Universe. The CMB therefore not only acts as a probe of the physical processes that happened prior to last scattering but also acts as a backlight to all the intervening matter between us and its source. The CMB photons keep on gravitationally interacting with the intervening matter field along the line of sight. These interactions cause the trajectory of these photons to be altered and hence distort the primary CMB sky. With the birth of the first stars, the UV radiation emitted by them caused the neutral Hydrogen to re-ionise and hence scatter the CMB photons. The CMB photons are also inverse Compton scattered by high energy electrons in galaxy clusters, which alters the shape of its spectra. The influence of all these effects is encoded on the CMB temperature and polarisation power spectra as secondary anisotropies as well as on the matter power spectrum.

1.6.1 Weak gravitational lensing

The CMB photons on their way from the last scattering surface to us encounter the intervening matter distribution. The interaction of the photons with the gravitational potential of the clusters, which are primarily made up of dark matter, lead to deviations in their trajectories. This causes what is known as weak gravitational lensing, small deflections in the photon trajectories that are small enough to be treated accurately up to first order approximations. The lensing of the primary CMB anisotropies conserves its brightness but remaps the anisotropies across the sky. The angular deflection field α of a CMB photon from the last scattering surface to us, after multiple deflections by gravitational potentials Ψ, under the Born approximation [30] is given by

$$\alpha = -2\int_0^{\chi_*} \mathrm{d}\chi \frac{f_K(\chi_* - \chi)}{f_K(\chi_*) f_K(\chi)} \nabla_{\hat{n}} \Psi(\chi\hat{n}; \tau_0 - \chi) \tag{1.75}$$

where, in a flat FRW universe, $f_K(\chi) = \chi = r$ is the comoving distance, $\nabla_{\hat{n}}$ is the gradient operator along the line of sight, and $\tau_0 - \chi$ gives the time at which the photon was at position $\chi\hat{n}$ and the integration is from the observer at the origin to the last scattering surface χ_*. The angular deflection is also known as the deflection field and is a function of the position $\hat{n}$ on the sky.

Using the formula for the deflection angle (Equation 1.75) we may define a lensing potential $\psi(\hat{n})$ such that $\alpha(\hat{n}) = \nabla_{\hat{n}}\psi$, an effective potential that can be used for calculating the effect of weak lensing on the CMB anisotropies [30]. Similar to the way we defined the temperature anisotropy power spectrum, we may expand the lensing potential in Harmonic space to define the lensing power spectrum

$$\psi(\hat{n}) = \sum_{lm} \psi_{lm} Y_{lm}(\hat{n}), \tag{1.76a}$$

$$\langle \psi_{lm} \psi^*_{lm} \rangle = \delta_{ll'} \delta_{mm'} C_l^{\psi\psi}. \tag{1.76b}$$

A useful connection between Inflation and the lensing potential may be drawn from the fact that the gravitational potentials the photon encounters are all derived from the evolution of the initial scalar perturbations produced during inflation. The lensing potential therefore can be written in terms of the initial scalar power spectrum $\mathscr{P}_{\mathfrak{R}}$, assuming a linear evolution, as

$$C_l^{\psi\psi} = 16\pi \int \frac{\mathrm{d}k}{k} \mathscr{P}_{\mathfrak{R}} \left[\int_0^{\chi_*} \mathrm{d}\chi T_\psi(k; \tau_0 - \chi) j_l(k\chi) \left(\frac{\chi_* - \chi}{\chi_* \chi} \right) \right]^2, \tag{1.77}$$

where $T_\psi(k,\tau)$ is the transfer function that evolves the primordial scalar fluctuation $k-\mathrm{modes}$ to the potentials Ψ at time τ such that $\Psi(k,\tau) = T_\psi(k,\tau)\mathfrak{R}_k$.

Of prime importance to us is the calculation for the effect of the lensing potential on the CMB power spectra. Following the derivation in [30][31], under the flat sky approximation valid for small deflections, and assuming no primary B-mode signal, the lensed power spectra are

$$C_l^{TT} = (1 - l^2 R^{\psi\psi}) C_l^{TT} + \int \frac{\mathrm{d}^2 \boldsymbol{l}'}{(2\pi)^2} \left[\boldsymbol{l}'.(\boldsymbol{l} - \boldsymbol{l}) \right]^2 C^{\psi\psi}_{|\boldsymbol{l}-\boldsymbol{l}'|} C^{TT}_{\boldsymbol{l}'}, \tag{1.78a}$$

$$C_l^{EE} = (1 - l^2 R^{\psi\psi}) C_l^{EE} + \int \frac{\mathrm{d}^2 \boldsymbol{l}'}{(2\pi)^2} \left[\boldsymbol{l}'.(\boldsymbol{l} - \boldsymbol{l}) \right]^2 C^{\psi\psi}_{|\boldsymbol{l}-\boldsymbol{l}'|} C^{EE}_{\boldsymbol{l}'} \cos^2 2\left(\phi_{\boldsymbol{l}'} - \phi_{\boldsymbol{l}}\right), \tag{1.78b}$$

$$C_l^{TE} = (1 - l^2 R^{\psi\psi}) C_l^{TE} + \int \frac{\mathrm{d}^2 \boldsymbol{l}'}{(2\pi)^2} \left[\boldsymbol{l}'.(\boldsymbol{l} - \boldsymbol{l}) \right]^2 C^{\psi\psi}_{|\boldsymbol{l}-\boldsymbol{l}'|} C^{EE}_{\boldsymbol{l}'} \cos 2\left(\phi_{\boldsymbol{l}'} - \phi_{\boldsymbol{l}}\right), \tag{1.78c}$$

$$C_l^{BB} = \int \frac{\mathrm{d}^2 \boldsymbol{l}'}{(2\pi)^2} \left[\boldsymbol{l}'.(\boldsymbol{l} - \boldsymbol{l}) \right]^2 C^{\psi\psi}_{|\boldsymbol{l}-\boldsymbol{l}'|} C^{EE}_{\boldsymbol{l}'} \sin^2 2\left(\phi_{\boldsymbol{l}'} - \phi_{\boldsymbol{l}}\right), \tag{1.78d}$$

where $\boldsymbol{l}$ are the Fourier modes under the flat sky approximation and $R^{\psi\psi}$ represents half of the total deflection angle power, given as

$$R^{\psi\psi} = \frac{1}{2} \langle |\alpha|^2 \rangle = \frac{1}{4\pi} \int \frac{\mathrm{d}l}{l} l^4 C_l^{\psi\psi}. \tag{1.79}$$

The effect of $R^{\psi\psi}$ in (Equation 1.78) is a rms deflection of $\sim 2.7'$ and the integral effectively convolves the primary CMB signal with the lensing power spectrum. At large and intermediate scales this leads to a smoothing of the peaks of the spectra. At high multipoles, where the primary signal is small due to diffusion damping, the fractional change in the amplitude of the spectra is large. The biggest implication is for the CMB B-modes, where even in the absence of any primordial signal, lensing transfers significant E-mode power to the B-modes leading to a white-noise like spectrum equivalent to $5.1\mu K$ at low multipoles. This lensing B-mode signal will thus mask any primordial B-mode signal that is subdominant to it.

The lensing of the CMB provides us an important method of probing the sum of the neutrino masses M_ν, reviews on the topic presented in [36][37]. Neutrino oscillation rules out massless neutrino species, and experiments have set a lower limit of $58\mathrm{meV}$ on the sum of neutrino

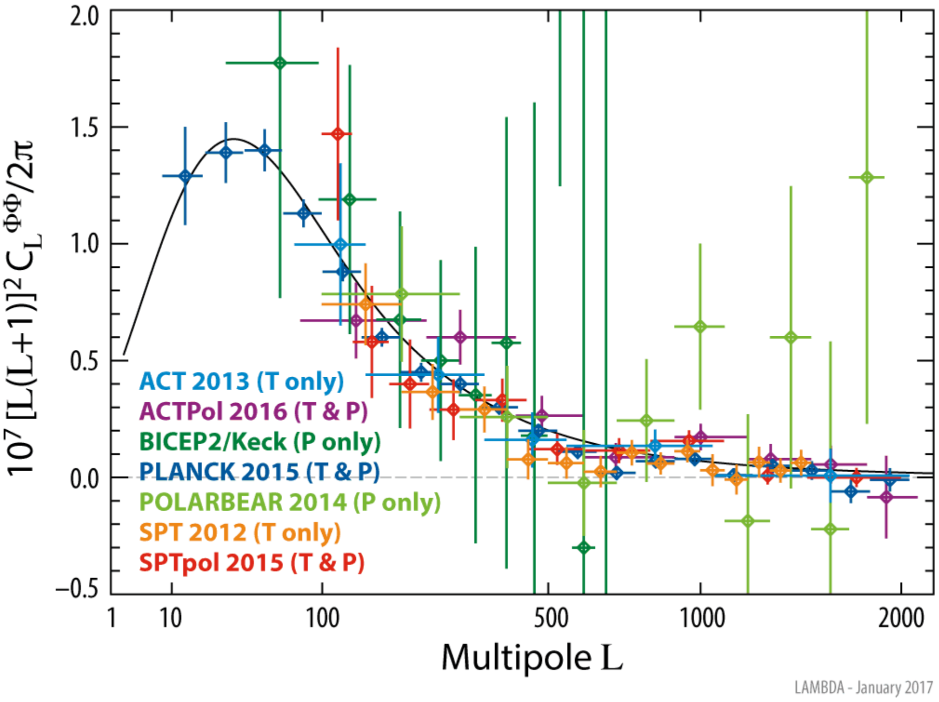

Figure 1.8: The figure illustrates the latest measured lensing power spectrum $C_L^{\phi\phi}$ from ACTpol[32], BICEP/Keck[33], Planck[34] and POLARBEAR[35]. The measured points are compared to the theoretically predicted spectrum. (Figure taken from *LAMBDA*.)

masses [38]. Massive neutrinos are expected to have a non negligible effect on the formation of structures, especially at late times when its contribution to the matter density is non-negligible. After the non-relativistic transition of neutrinos, free streaming causes a damping of the neutrino density fluctuations at small scales. On the matter power spectrum, this leads to a suppression on scales below the free-streaming scale. The magnitude of the suppression is proportional to the contribution of the neutrino mass to the total matter density.

A sub eV neutrino mass will not affect the primary CMB anisotropy directly as the neutrinos were relativistic at Recombination but are expected to modify the background evolution and the generation of secondary anisotropies. Massive neutrinos can affect the CMB anisotropies by a shift in the redshift of matter-radiation equality, a change in the angular diameter distance to the last scattering surface and by a change in the late ISW effect. These effects are however degenerate with other cosmological parameters such as H_0 and measurement of the late ISW effect is cosmic variance limited [37]. The effectiveness of the CMB power spectra in constraining neutrino mass is limited and the most important probe is therefore through the measurement of the matter power spectrum.

$$M_\nu < 0.23\mathrm{eV}, \quad 95\%\mathrm{CL}, \text{Planck TT+lowP+lensing+ext} \tag{1.80a}$$

$$N_{\mathrm{eff}} = 3.04 \pm 0.33, \quad \text{Planck TT,EE,TE+lensing+ext.} \tag{1.80b}$$

The current measurement on the sum of neutrino masses by the *Planck* mission [15] has set an upper limit and set constraints on the effective degrees of freedom N_{eff}. A deviation of N_{eff}

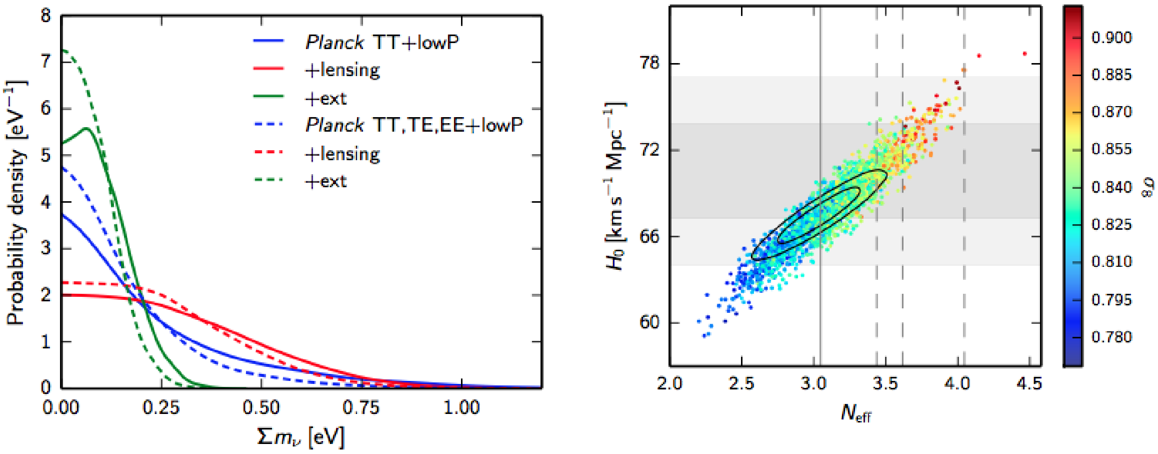

Figure 1.9: *Left*: Constraints on the sum of neutrino mass $\sum m_\nu$ from different datasets. *Right*: The effective degree of freedom $N_{\rm eff}$ constrain against H_0 from *Planck* TT+lowP chain. Higher value of $N_{\rm eff}$ favour H_0 closer to other probes but it increases σ_8. Solid black lines are from *Planck* TT,EE,TE+lowP+BAO. (Figures taken from [15].)

from 3.046 will suggests the presence of additional degrees of freedom such as axions [39]. The neutrino masses also come in two hierarchies, and a constraint on M_ν below 0.1eV will rule out the inverted hierarchy.

1.6.2 Reionisation

After the epoch of Recombination, the free electrons were captured to produce neutral Hydrogen and Helium, however, observation of the Gunn-Peterson effect in the quasar spectrum [40] showed that the Inter Galactic Medium (IGM) was almost fully ionised by redshift $z \approx 6$.

The reionisation history is a matter of debate. Current understanding states that with the birth of the first stars, the UV radiation from these re-ionised the neutral Hydrogen in the IGM between $z \approx 12$ to $z \approx 6$. The CMB photons Compton scattering with the free electrons have the effect of suppressing power in the TT spectrum inside the Hubble horizon at the Reionisation epoch, typically above $l \approx 10$. Most importantly, the quadrupole anisotropy seen by the free electrons produce an additional polarisation signal in the TE and EE spectra characterised by a bump at low l. The angular scale subtended by the polarisation signal from Reionisation depends upon the epoch at which the photons scattered, hence the position of the Reionisation bump is directly related to the epoch of Reionisation $z_{\rm re}$. The amplitude of the bump is directly related to the Thomson scattering optical depth τ and is insensitive to the details of the Reionisation history. The bulk motion of the electrons also induce a diffuse kinetic Sunyaev-Zeldovich effect (described in next subsection), and the k-SZ power at $l = 3000$, $A_{\rm kSZ}$ is another observable from CMB data. [41] provides a review of reionisation, compares different reionisation parametrisation models, observables and constraints from the *Planck* data.

The difficulty in measuring Reionisation lies in the fact that these effects are degenerate with other parameters such as the sum of neutrino masses M_ν and with the scalar spectral index n_s. The low-l in polarisation has not been measured yet where the most prominent reionisation signature lies. Quoted below is the constraint on the Thomson optical depth τ, for an instantaneous reionisation history. Also, the reionisation epoch $z_{\rm re}$ and the duration of reionisation Δz using CMB anisotropy and k-SZ data for a symmetric redshift model are [41]

$$\tau = 0.058 \pm 0.012, \quad \text{PlanckTT} + \text{low-}l \text{ EE} \tag{1.81a}$$

$$z_{\text{reio}} = 7.8 \pm 0.9, \tag{1.81b}$$

$$\Delta z < 2.8. \quad 95\%\text{CL} \tag{1.81c}$$

Future measurements of the $\text{low} - l$ polarisation spectra are expected to give an order of magnitude better constraint on these parameters [42].

1.6.3 Sunyaev-Zeldovich effect

CMB photons that pass through the hot intra-cluster gas of galaxy clusters inverse Compton scatter with the free electrons. This causes a distortion in the frequency spectrum of the CMB by up-scattering low energy photons to higher energy pivoting about 217GHz. The amplitude of the distortion is proportional to the volume-integrated pressure of the cluster which directly relates to the cluster mass. This effect is known as the Sunyaev-Zeldovich effect and is a redshift-independent method of studying galaxy clusters up to high redshifts, limited only by the noise cutoff of the survey. Apart from the regular thermal SZ effect, the peculiar velocity of the clusters introduces a Doppler shift in the re-radiated photons and appears as an additional distortion, subdominant to the t-SZ, to the thermal spectrum. Reviews of these effects and Cosmology using SZ are [43][44].

The t-SZ effect offers a unique and alternative method of probing the cosmological parameter space as it directly detects the evolution of cluster counts with redshift. This is a key feature of the evolution of density perturbations and is sensitive to the underlying cosmology, dark matter distribution, dark energy equation of state and neutrino mass. Current observations by high resolution instruments such as ACT, SPTpol and Planck have improved the statistics on cluster counts with t-SZ to allow for cosmological parameter estimation [45] [46] [47]. Together with external datasets from galaxy surveys, cluster counts provide alternative constraints on Ω_m and σ_8.

1.7 Current Status of Power Spectrum Observation

At present, the CMB TT power spectrum has been measured with a high signal to noise ratio up to high multipoles by several experiments. The *Planck* satellite gives the best measurement on the low to intermediate scales [48] but is limited at the high multipoles due to its beam size. The high multipoles have been probed by ground experiments like ACTPol [49], and SPTpol [50].

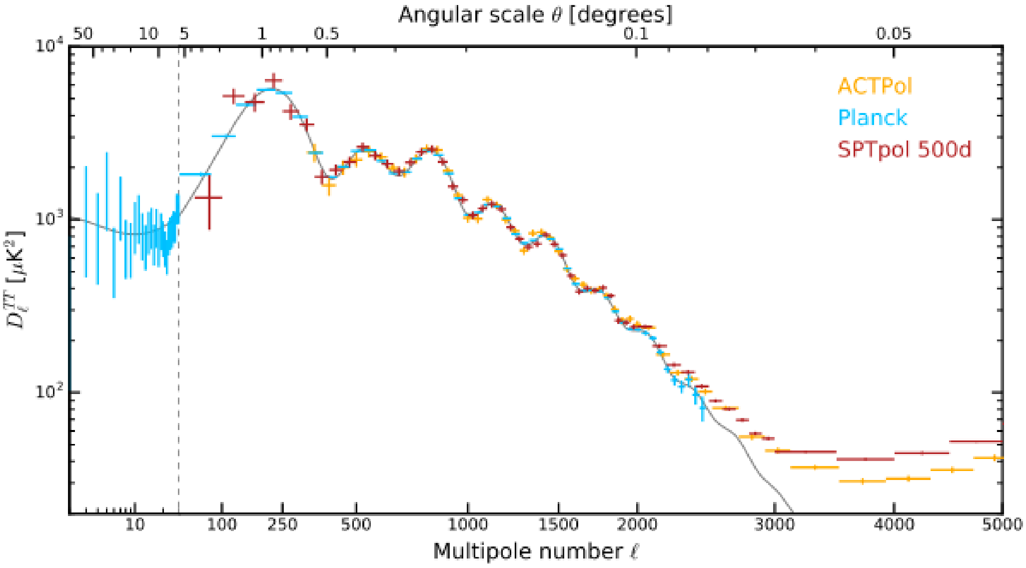

Figure 1.10: The figure illustrates the best measurements of the CMB TT spectrum by the various experiments. As can be seen, the TT spectrum has been strongly constrained up to high multipoles. The large sky coverage of *Planck* allows it to probe the low-l spectrum not accessible from the ground. The higher angular resolution of the ACTPol and SPTpol, due to their large mirror aperture, allows them to probe the high multipoles. The deviation at high-l from the ΛCDM model (grey line) is due to the signal being dominated by emission from radio galaxies, dusty star forming galaxies and the SZ effect. (Figure taken from [50].)

For polarisation, the EE auto spectrum and TE cross spectrum have been fairly constrained by the current generation of probes (Figure 1.11) up to high values of l. *Planck* provides the strongest constraints up to intermediate l's, BICEP/Keck [51] at the largest scales, and SPTpol [50] gives the strongest measurements to date at the high multipoles. Currently, the sensitivity in measuring B-modes is being pushed beyond the lensing spectrum in a effort to detect the primordial CMB B-modes. The strongest constraints on the lensing B-mode spectrum comes from BICEP/Keck [52] on the large scales with intermediate scales being probed by POLARBEAR [35] SPTPol [50] and ACTpol. The measurement of polarisation is limited by the overall instrument sensitivity, diffuse galactic emissions and systematic effects.

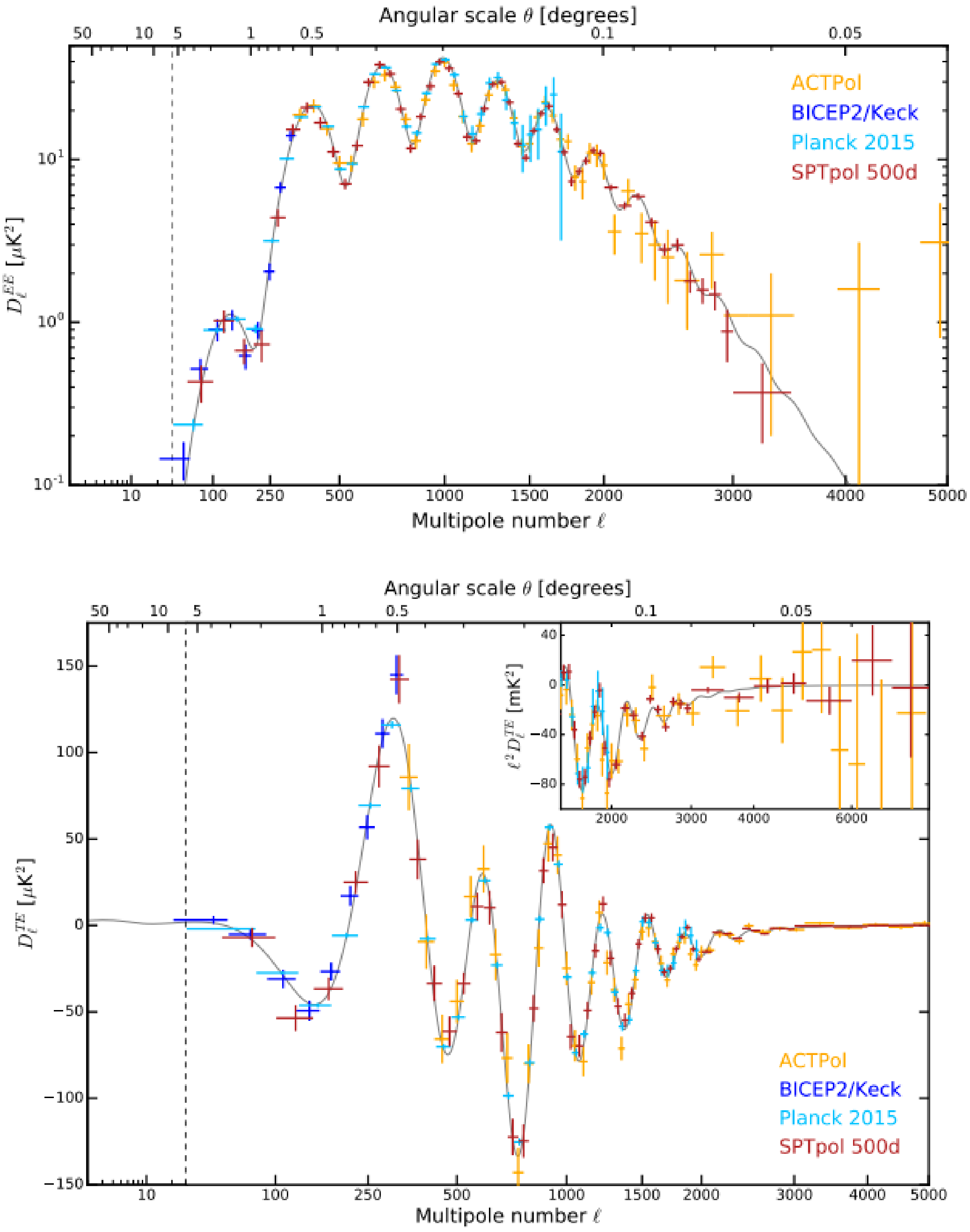

Figure 1.11: The figures illustrates the best measurements of the CMB TE and EE spectrum by the various experiments. The low-l where the reionisation bump is expected to lie is absent. Planck is limited to measurements below $l = 1750$ in EE. The $500\mathrm{sq.deg}$ measurement by SPTpol gives the best current measurement at high-l in both TE and EE. The discrepancy in the EE spectrum between SPTpol and ACTPol are attributed to different galactic masks used. (Figures taken from [50].)

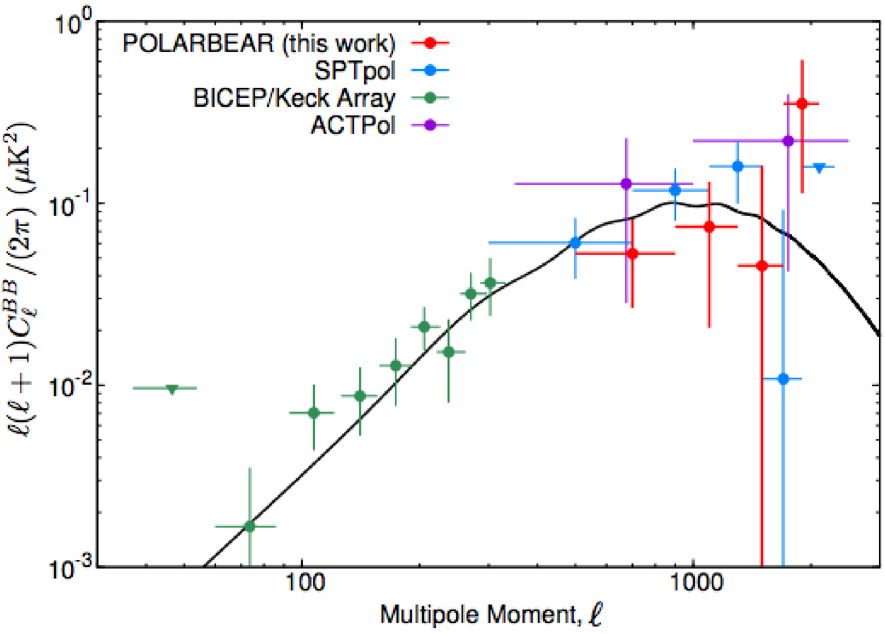

Figure 1.12: The figures illustrates the best measurements of the CMB BB spectrum by the various experiments. The best measurement of the lensing B-mode spectrum at low-l is from BICEP2/Keck [52]. The higher multipoles are best measured by POLARBEAR [53]. Error bars are given at 1σ and upper limits at 2σ CL. (Figure taken from [53].)

1.7.1 Limit on power spectrum estimation

The reconstructed maps of the CMB sky contain contributions from the detector noise, foregrounds and systematic effects. On top of this, the primary CMB signal is affected by the secondary anisotropies due to the CMB photons traversing the intervening Universe between the last scattering surface and us. From our vantage point in the Universe we are able to observe just a single representation of the CMB sky that was produced on a constant time hypersurface, hence this puts up a theoretical limit on the precision with which we can estimate the power spectra.

Since out modern detectors are nearly photon noise limited, let us consider the theoretical maximum to which we can measure the CMB power spectra assuming we have an instrumental noise with a white spectrum. The detectors observe the sky with an instrumental beam which has a smearing effect on the sky. A perfectly Gaussian beam has the effect of attenuating the multipole signal exponentially [54], and the beamed spectra is given by

$$C_l^{\text{beamed}} = \begin{cases} C_l \exp\left[-\sigma_b^2 \{l(l+1)\}\right] & \text{TT} \\ C_l \exp\left[-\sigma_b^2 \{l(l+1)-4\}\right] & \text{EE, BB} \end{cases} \tag{1.82}$$

where σ_b is the width of the symmetric Gaussian beam.

It is standard practice to observe the de-beamed spectra in order to compare with theoretical models. This is achieved by inverting the equations (Equation 1.82). This however has the unfavourable effect of exponentially boosting the white noise spectrum at high multipoles. Together with white noise, long timescale drifts and correlated noise produce a $1-\mathrm{over}-f$

spectrum given by

$$P(f) = \sigma^2 \left[\left(\frac{f_k}{f} \right)^\alpha + 1 \right], \tag{1.83}$$

where, σ is the white-noise rms at high frequencies, f_k is a knee frequency and α is the slope of the spectra at low frequencies. Typical values of white noise rms, knee-frequency and slope, expected for a next generation space experiment such as CORE , are $40\mu\mathrm{K}\sqrt{\mathrm{s}}$, $20\mathrm{mHz}$ and 1 respectively.

Apart from the detector noise contribution, the fact that we are just observing a single sky realisation puts a statistical limit to our measurement. By averaging over all the a_{lm} for each l to obtain C_l, we are left with an intrinsic uncertainty called the Cosmic Variance. Considering the simple situation of an uniformly sampled sky map with a noise residual of ω, normalised to a unit solid angle, the standard deviation due to detector noise and Cosmic Variance is given by [55],

$$\Delta C_l = \sqrt{\frac{1}{f_{\mathrm{sky}}} \frac{2}{2l+1}} \left[C_l + \omega^{-1} B_l^{-2} \right] \tag{1.84}$$

where, B_l^2 is the exponential part in (Equation 1.82) and f_{sky} is the fraction of the sky that has been observed.

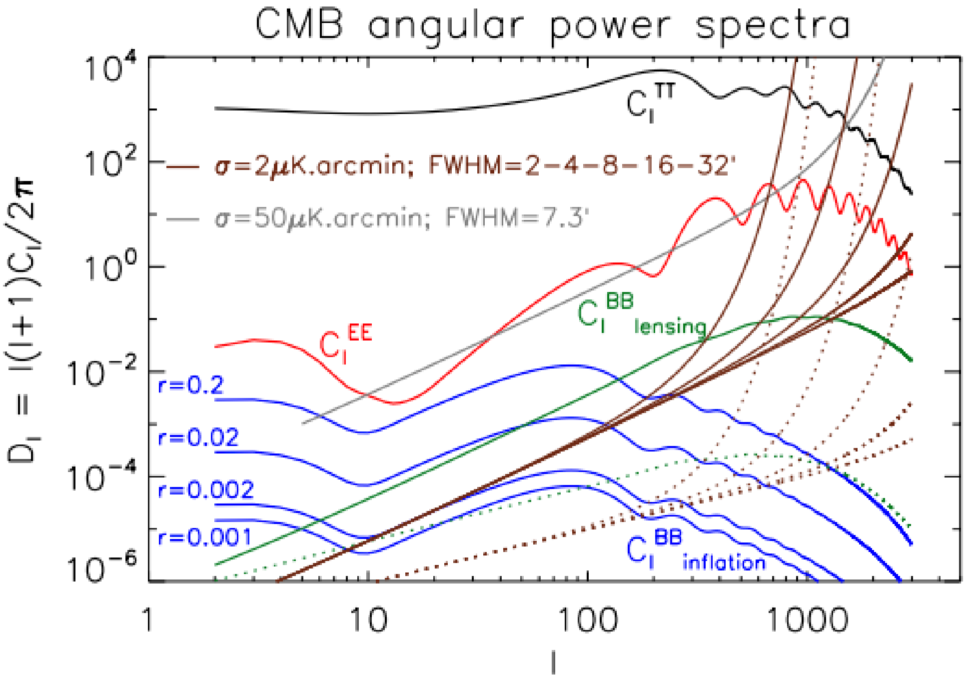

Figure 1.13: The effect of de-beaming the white-noise from an uniformly sampled CMB map is shown for two cases of noise amplitude $2\mu\mathrm{K.arcmin}$ with a $7.3'$ beam FWHM, and $50\mu\mathrm{K.arcmin}$ for a variety of beam FWHM of $2'$, $4'$, $8'$, $16'$, $32'$. Shown in dotted lines is the cosmic variance from lensing B-modes (green) and from the noise itself (brown). (Figure taken from [56].)

A major source of nuisance in the CMB frequencies of interest is the presence of galactic

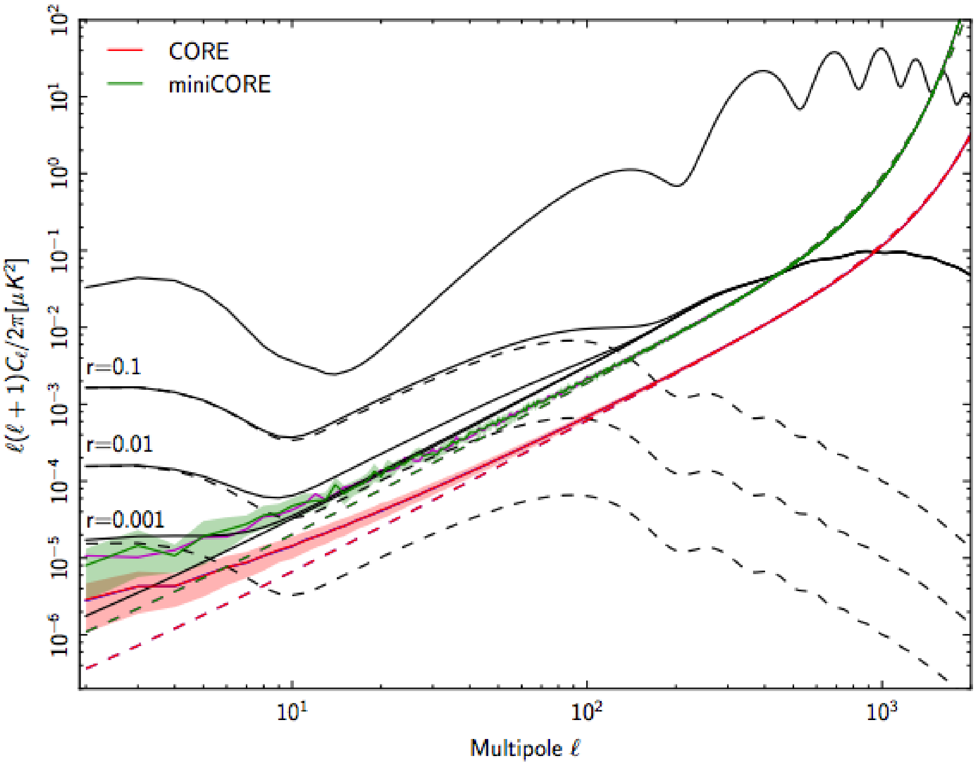

Figure 1.14: The noise power spectrum obtained using the specifications of the CORE proposal for the CMB channels between $130\mathrm{GHz}$ and $220\mathrm{GHz}$ simulated using a $1-\mathrm{over}-f$ noise with $f_k = 50\mathrm{mHz}$. The dashed lines show the expected white-noise power spectrum whereas the solid lines show the $1-\mathrm{over}-f$ residuals. (Figure taken from [57].)

foreground emissions as well as certain extra-galactic radio sources. Below $100\mathrm{GHz}$, the main contributors of signal to the CMB channels are Synchrotron, Bremsstrahlung and anomalous dust emission. Above $100\mathrm{GHz}$ the astrophysical sources are dominated by thermal dust emission. Apart from these there are the molecular lines such as from CO which has strong emission lines at $115\mathrm{GHz}$ and its multiples. Among the astrophysical sources, the synchrotron is expected to be up to 75% polarised and thermal dust at greater than 10%. Unlike the CMB temperature anisotropies, the CMB polarisation signal is subdominant to the polarised galactic emissions throughout the sky. Measurement of the CMB polarisation signal is therefore severely restricted and requires estimation and subtraction of the foreground emissions. Another source of nuisance in the case of estimation of primordial CMB B-modes is the lensing B-mode signal which adds a white-noise like signal up to intermediate scales equivalent to $5.1\mu\mathrm{K.arcmins}$.

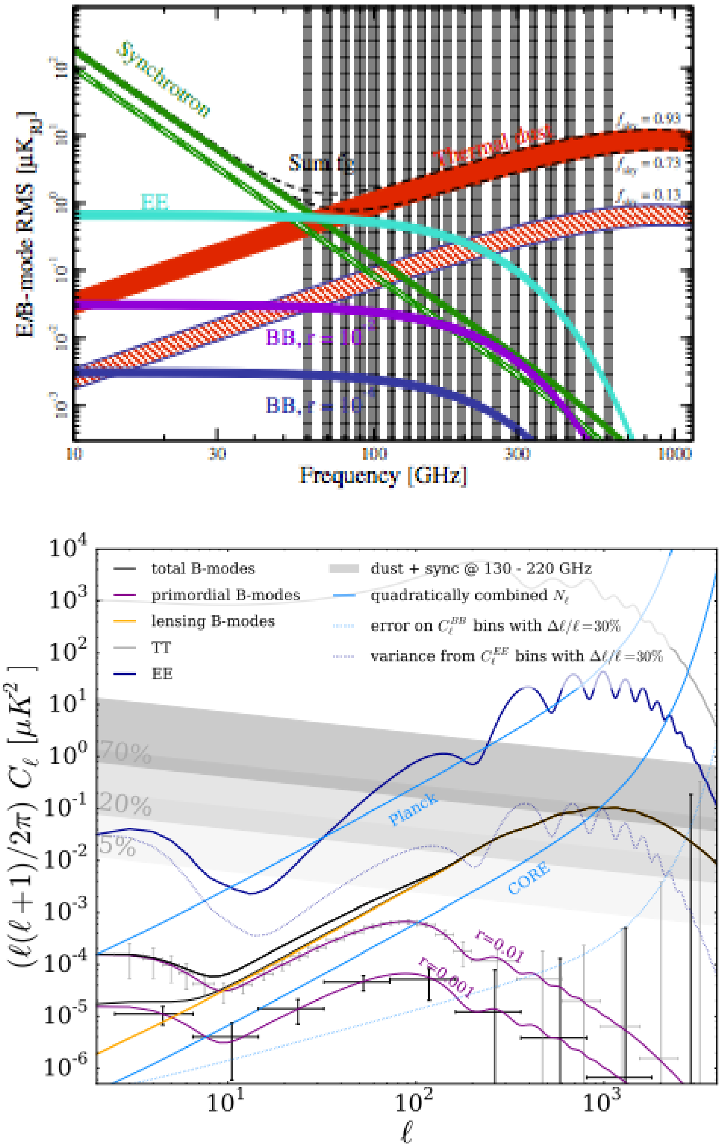

Figure 1.15: *Top*: The brightness temperature spectra of different polarised diffuse emissions from the galaxy, at $40'$ smoothing, are shown compared to the E and B mode CMB spectra. The primordial B-mode power has been shown for fiducial values of $r = 10^{-2}, 10^{-4}$ and shows that the polarised synchrotron emission dominates throughout and in the best 13% of the sky, the thermal dust signal still dominates at the proposed frequencies. The vertical bands are the observation bands for the proposed CORE mission. Figure taken from [58]. *Bottom*: The foreground emission in the angular power spectrum compared to fiducial values of B-mode spectra at $r = 10^{-2}, 10^{-3}$ is shown. The grey bands correspond to 70%, 20% and 5% of the best part of the sky and shows the range of emission from 130GHz to 220GHz. Using smaller fractions of the sky less contaminated by foreground help but is detrimental at low multipoles as it boosts the Cosmic Variance. (Figures taken from [57].)

CHAPTER 2

MOTIVATION FOR A CMB SPACE MISSION

Over the past three decades, observation of the Cosmic Microwave Background radiation by successive generations of experiments from the ground, balloons and space have brought significant advances in the field of Cosmology. Among these, the landmark achievements have been brought by the previous three generations of CMB space missions, namely *COBE*, *WMAP* and *Planck* . *COBE/DMR* provided us with the first measurement of the CMB temperature anisotropies and *COBE/FIRAS* established the radiation spectra as a near perfect black body. The *WMAP* probe brought us into the domain of precision measurement of cosmological parameters. The *Planck* mission extracted almost all the information possible from the temperature anisotropy spectrum, it provides a legacy survey of the CMB temperature sky as well as many of the foregrounds over several frequency bands, and also provides us with one of the cleanest measurements, up to date, of the E-mode spectra and lensing power spectrum.

Despite impressive advances in Cosmology, several open questions still remain regarding our Universe. Prime among these are the ones regarding the earliest epochs. We do not know whether the Universe underwent an Inflationary phase or if some other mechanism is responsible for the homogeneity on large scales and seeding of the early Universe with density fluctuations. We also know that only a small fraction (5%) of the matter-energy density is visible baryonic matter, the rest being dark matter (26%) and dark energy (69%). The nature of the latter two have remained elusive till now. The Universe is known to have gone through a phase where the light from the first stars re-ionised the neutral Hydrogen. The CMB is sensitive to this effect but as of yet we have only been able to achieve preliminary measurements of the physics of this epoch between $z \sim 6$ and $z \sim 10$. The mass of the neutrino species is yet another question of importance both for the formation of cosmological structures, and for the physics of elementary particles. Even among parameters strongly constrained by CMB observations, there exists strong tension with other probes and with internal data subsets. Whether these tensions are due to statistical excursions, interpretation errors, or are a sign of new physics remains to be elucidated with more precise observations.

2.1 The Science Case

The observation of the CMB polarisation signal has opened up a new window to observe the physics of the Universe. It complements the measurements that have been done using temperature anisotropies alone. The science goals that can be achieved by a next generation CMB polarisation mission can be broadly divided into the following sectors.

Inflation: The primary science driver for a future CMB polarisation space mission is the detection of a primordial CMB B-mode signal. Detection of this signal is currently the single most effective way of probing Inflation as it is generated solely from gravitational waves from the Inflationary epoch. Inflation also predicts that these B-modes peak on large scales $(l \approx 80)$ meaning they are best probed with a large sky coverage best accessible from space. With the current upper limits set by the Planck and BICEP/Keck experiments on the tensor to scalar ratio $r < 0.09$ at a 95% confidence level [15], it is necessary to probe this parameter at higher sensitivities. The CORE proposal states a polarisation sensitivity of $1.7\mu\mathrm{K.arcmin}$ [56] and CMB-S4 a $1\mu\mathrm{K.arcmin}$ over half the sky [59]. This will push down the sensitivity on r to about $\delta r \approx 0.001$ if contamination by foreground emission can be eliminated. This is sufficient to detect an Inflationary B-mode signal predicted by the most popular models of Inflation. A single field slow-roll Inflation model predicts, using (Equation 1.56), $r \approx 0.1$ which is at mild tension with current measurements and using a 3σ upper limit on n_s, a $r \approx 0.05$. The R^2 inflation predicts $r \approx 0.0035$ and $r > 0.0008$ using the 3σ limit on n_s. A smaller value of r is however not improbable, as predicted from small field Inflationary models. A null detection of an Inflationary B-mode signal above $r = 0.001$ will go a long way in reducing the set of possible Inflationary models and promote the development of alternative models of the early Universe.

Neutrinos: Neutrinos are known to be massive due to neutrino oscillation and experiments currently set a lower limit to the sum of neutrino masses $M_\nu > 58\mathrm{meV}$ [38]. Cosmological probes set an upper limit of $M_\nu < 0.23\mathrm{eV}$ [15]. Massive neutrinos with $M_\nu < 1\mathrm{eV}$ are expected to affect the CMB anisotropies by modifying the background evolution and through late time effects. However, these effects are degenerate with those due to other cosmological parameters such as H_0. Measurement of the CMB lensing spectrum will break the degeneracies, and is a promising way of probing the mass of neutrinos.

The non-negligible contribution of neutrino mass to the overall matter density will suppress structure formation at late times [37]. This will lead to a near constant suppression of the lensing power spectrum on scales $l > 100$. Combining a CORE like mission with other cosmological probes of matter distribution is expected to be sensitive to $\sigma(M_\nu) = 16\mathrm{meV}$ which would give a 4σ detection at the lower bound of the neutrino mass range [42]. There exists two possible neutrino mass hierarchies. Constraining the upper bound to $< 100\mathrm{meV}$ will rule out the inverted hierarchy.

A stronger constraint on the number of degrees of freedom $\sigma(N_{\mathrm{eff}}) = 0.041$ can also be achieved using CMB polarisation data from a CORE like mission [42]. A deviation of N_{eff} from 3.046 will suggest the existence of additional degrees of freedom such as axions [39].

Standard Cosmological Model: The nature of Dark Matter and Dark Energy is unknown to us at present. Constituting $\sim 95\%$ of the matter energy density of the Universe, this leaves a big gap in our knowledge. The measurement of other parameters such as H_0, σ_8 and Ω_k by Planck also shows tension with alternative probes as well as with internal data subsets. H_0 measured by Planck [15] and by using Cepheid+SNe data [16] show a $\sim 3\sigma$ deviation. Cluster count with CMB using the t-SZ effect provides an alternate method of measuring the evolution of large scale structures. Measurement of Ω_m and σ_8 independently using cluster counts and CMB anisotropy data shows a discrepancy [15]. All these fundamental cosmological parameters affect the CMB as well as the evolution history of the matter and galaxy distribution leading up to the present epoch. The CMB offers us three tools, namely its temperature and polarisation power spectra, the lensing spectrum and t-SZ cluster counts. Together, these are demonstrated to better constrain the cosmological parameters [57] [60] for a CORE like mission. Tensions that may remain will prompt a modification and re-evaluation of the standard Cosmological Model.

Reionisation: The Reionisation epoch is poorly understood and its effects on the CMB spectra are degenerate with those from other parameters such as n_s. The reionisation history of the Universe is important as it impacts the understanding of the formation of the first stars and galaxies, and their evolution. The CMB polarisation spectra are particularly sensitive to the reionisation optical depth τ and the redshift of the epoch of reionisation. It produces a bump at $l < 30$ in the polarisation power spectra. Forecasts for CORE show the ability to constrain the redshift of the reionisation epoch an order of magnitude better than Planck and gives $\sigma(\tau) = 0.0021$ [42].

2.2 Proposed Space Missions

The massive science possibilities that can be realised by a comprehensive CMB Polarisation space mission has prompted several proposals over the past few years. A few variants of the CORE mission proposal have been made in the past few years to ESA including COrE+ and COrE. On the US side, a mission concept study, EPIC/CMBpol was carried out, and a Fourier transform spectrometer, PIXIE, to observe simultaneously in 400 frequency bands over two decades of frequencies was proposed. As of 2017, these proposals have not met with success. The LiteBIRD mission, proposed to JAXA is the only mission undergoing a phase of study. Currently, a preliminary study for a “probe-class” mission is underway in the US for a possible proposal in the early $2020\mathrm{s}$ to NASA.

I give a brief overview of the two future CMB probes that I have worked on during my time as a doctoral student.

2.2.1 CORE

The CORE mission was proposed to ESA in 2016 in answer to the “M5” call for a space mission. It is a polarimetric imager designed to observe the CMB polarisation sky in order to exploit the scientific information available in the E and B modes.

The primary science goal of CORE is to detect a primordial B-mode signal with a sensitivity on r at $\delta r < 0.0003$ signal. It will also observe the lensing B-modes and lensing of E modes by large scale structures. It is designed to probe the neutrino mass scale at 4σ at $60\mathrm{meV}$. It will provide additional constraints on the principal cosmological parameters with a combination of polarisation, SZ cluster counts and lensing data [42][56][61]. Due to its large frequency coverage it will provide a legacy survey of the galactic foreground emission and improve the understanding of galactic magnetic fields.

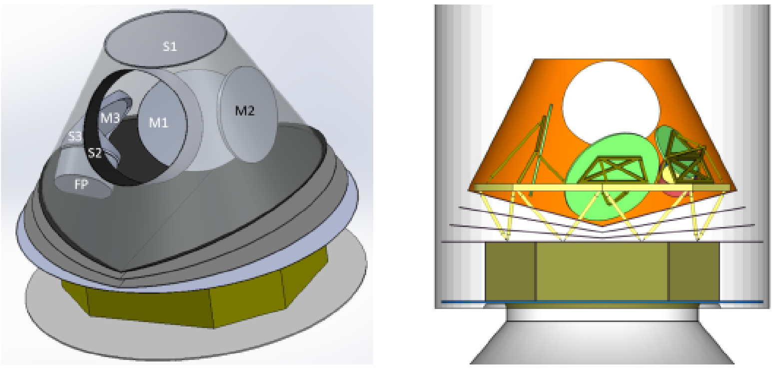

Figure 2.1: The Conceptual sketch of the main elements of CORE. (Figure taken from [56].)

The principal features of the CORE mission design are as follows [56]:

- CORE will perform a full sky survey for a mission duration of 4 years. It will complete a full sky scan every 6 months.
- It will be placed in a Lissajous orbit around the second Sun-Earth Lagrange point ($\mathrm{L2}$).
- It will scan the sky with a combination of two rotational motions. The entire instrument will perform a long precession (4 days) about the anti-solar axis, and a fast spin (120 seconds) about the spacecraft's principal axis of symmetry. In the baseline design, the spin axis is at $30\,°$ from the anti-solar axis and the optical axis is at $65\,°$ from the spin axis.
- It will observe the microwave sky in 19 frequency channels between $60\mathrm{GHz}$ and $600\mathrm{GHz}$. Six of these channels from $130\mathrm{GHz}$ to $220\mathrm{GHz}$ will be dedicated primarily to CMB observation. Six channels from $60\mathrm{GHz}$ to $115\mathrm{GHz}$ will mainly monitor low-frequency and astrophysical foregrounds. Seven channels from $255\mathrm{GHz}$ to $600\mathrm{GHz}$ will monitor thermal dust emission. The bandwidth of each channel is taken to be 30% of the central frequency.
- Two main options have been proposed for the telescope design, a Gregorian or a crossed-Dragone design. The crossed-Dragone design will have a $1.2\mathrm{m}$ aperture for primary mirror.
- The focal plane will have 2100 cryogenically-cooled, polarisation-sensitive Kinetic Inductance Detectors (KIDS).
- The total aggregate polarisation sensitivity achieved will be $1.7\mu\mathrm{K.arcmin}$ with the full array. With the CMB channels alone, the aggregate polarisation sensitivity will be $2\mu\mathrm{K.arcmin}$.
- For a $1.2\mathrm{m}$ crossed-Dragone design, the lowest resolution is $\sim 18'$ for the $60\mathrm{GHz}$ channel and the highest is $\sim 2'$ for the $600\mathrm{GHz}$ channel. The CMB frequency bands will be between $\sim 9.5'$ to $\sim 5.2'$ in resolution.
- The baseline design calls for no half-wave plate to actively modulate the polarisation.

- The instrument is designed such that the payload module is passively cooled to about $40\mathrm{K}$. This is done by keeping it in the shadow of the service module and thermally decoupling it using highly reflective V-grooves. The instrument is designed as symmetric as possible to avoid thermal drifts from modulation of the solar flux as the spacecraft scans.

2.2.2 LiteBIRD

LiteBIRD is a next generation CMB polarisation mission proposed to JAXA in 2008 and is currently undergoing a phase of study. Its primary objective is to measure the CMB primordial B-modes with a sensitivity on r at $\delta r < 0.001$ [62].

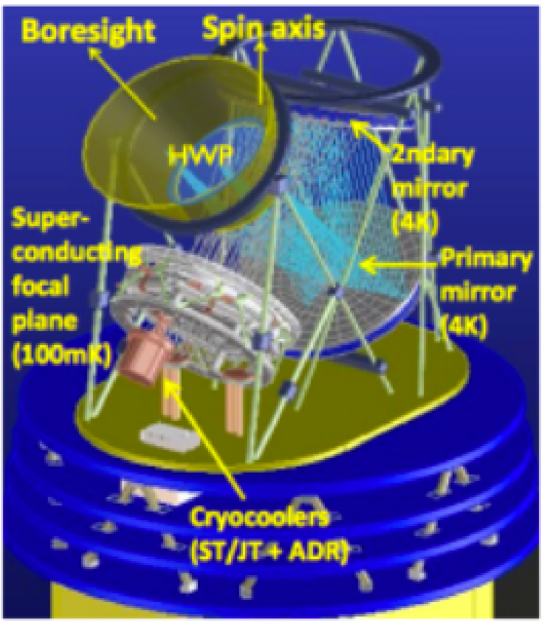

Figure 2.2: The schematic overview of the LiteBIRD instrument. (Figure taken from [62].)

The principal features of the LiteBIRD mission design are as follows [62]:

- Provide a full sky observation of the CMB polarisation sky for a mission duration of 2 years.
- The telescope will be placed at the second Sun-Earth Lagrange point ($\mathrm{L2}$) similar to CORE.
- It will scan the sky in a combination of two rotational motions similar to CORE. It will have a fast precession period of ~ 93 minutes and a slow spin period of 600 seconds. The optical axis will be at 30° to the spin axis and the spin axis will subtend an angle of 65° to the anti-solar axis.
- It will observe in 6 frequency channels from $60\mathrm{GHz}$ to $280\mathrm{GHz}$ with a bandwidth in each channel of 30% of the frequency centre.

- The optical design includes a crossed-Dragone telescope with an aperture stop and primary and secondary mirrors. The aperture of the primary mirror will be $30\mathrm{cm}$.

- The polarisation will be actively modulated by an achromatic half-wave plate placed at the aperture.

- It has the option of using either TES bolometers or MKIDS. If bolometers are used, it will employ 2022 detectors on the focal plane.

- It will have a mean aggregate sensitivity of $1.8\mu\mathrm{K.arcmin}$ for the whole array and $2.9\mu\mathrm{K.arcmin}$ for the combined $100\mathrm{GHz}$ and $140\mathrm{GHz}$ channels.

- The beams will be significantly larger than CORE due to its smaller aperture. The resolution ranges from $16'$ at $280\mathrm{GHz}$ to $75'$ at $60\mathrm{GHz}$.

2.3 Practical Advantages of Space

Observing the radiation in the microwave frequencies from space has several advantages over ground based telescopes. These have been demonstrated by the previous three generations of CMB space missions. The following points illustrates that.

- **Access to frequency bands:** The CMB frequency spectrum peaks at around $160\mathrm{GHz}$ for a Planckian spectrum of $2.73\mathrm{K}$. The best frequencies to observe the CMB therefore range from a few GHz to a few hundred GHz. The galaxy also emits radiation both in intensity and polarisation in the microwave frequencies through different physical processes as discussed in (1.7.1). Any measurement of B-mode signal is practically impossible at any sky fraction or at any angular scale without any foreground subtraction. To estimate the foreground emissions it is necessary to observe the microwave sky at several frequency bands about the CMB peak [63]. The CORE mission proposes 19 bands ranging from $60\mathrm{GHz}$ to $600\mathrm{GHz}$ [56] whereas the PIXIE [64] study aimed at 400 spectral bands over two decades of frequency. Space provides unrestricted access to the entire microwave frequency range for CMB observation whereas observation from the ground is restricted by the presence of water vapour in the atmosphere. This produces sharp absorption bands, leaving only a few windows for CMB observation at $30\mathrm{GHz}$, $95\mathrm{GHz}$, $150\mathrm{GHz}$ and $220\mathrm{GHz}$. The atmospheric windows are illustrated in (Figure 2.3).

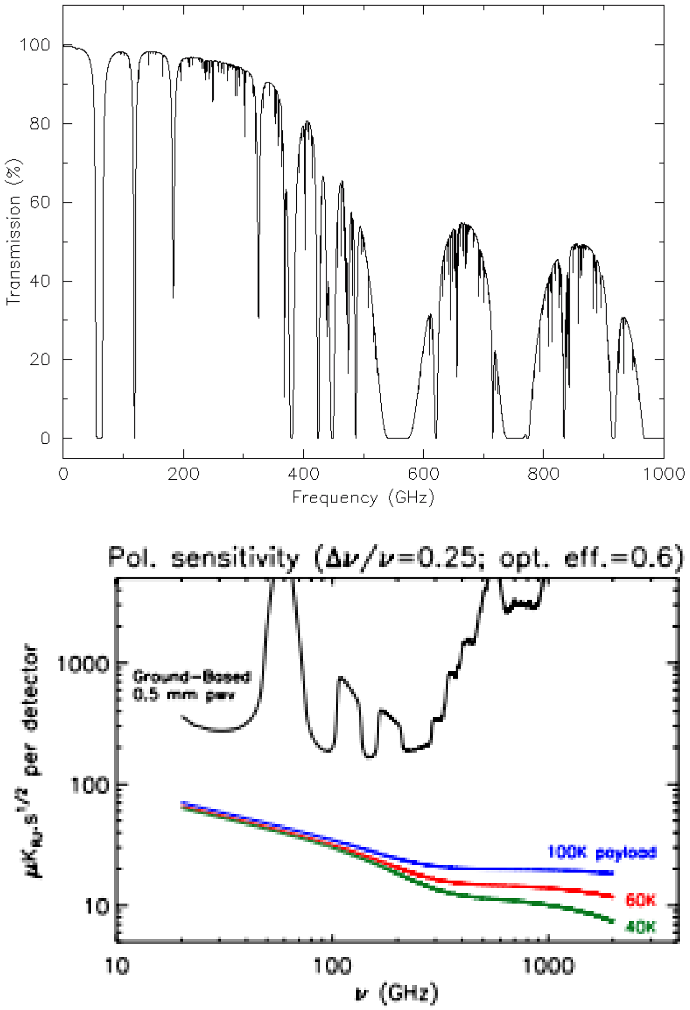

Figure 2.3: The top panel shows the atmospheric transmission in the GHz frequency range assuming $0.5\mathrm{mm}$ of integrated precipitable water vapour. Conditions experienced on the Atacama plateau are better than this for under 25% of the time [65]. The bottom panel shows the sensitivity achieved by a single polarisation sensitive detector, assuming a frequency bandwidth $\Delta\nu/\nu$ of 0.25 and 60% optical efficiency. The coloured lines represent the corresponding sensitivity from space with different payload temperatures. (Figure taken from [56].)

- **Thermal Stability and Sensitivity:** Observing from space, especially the Sun-Earth Lagrange Point 2 $(\mathrm{L2})$ provides a very stable and cold environment for systems to function. The low thermal loading in the cold environment allows detectors to be photon noise limited. Ground experiments have to deal with water vapour and oxygen molecules in the Earth's atmosphere, which emit significant radiation in most of the microwave frequency range suitable for CMB observation and add to the thermal loading of the detectors. Moreover, the temporal and spatial variations of the atmospheric transmission and emission [65] make calibration difficult and contribute to correlated noise and systematics. The difference between the raw polarisation sensitivity per detector achieved by a space-borne observatory and by a ground-based experiment is illustrated by (Figure

2.3). The number of detectors required can be reduced by a couple orders of magnitude for a space mission. To mitigate the effects of the atmosphere, detailed modelling of atmospheric emissions and their contribution to correlated noise need to be made [65]. Filtering techniques are also required at the analysis stage such as [66]. A space mission completely avoids the complications that arise due to the atmosphere.

- **Large sky coverage:** A space mission allows us to easily perform a complete scan of the sky with a sufficiently uniform scan density. This allows us to probe the low-l multipoles in the power spectrum where the ISW effect is dominant in the TT spectrum, the reionisation bump $(l < 10)$ in the EE spectrum (and primordial BB), and a lot of the expected primordial B-mode signal in the recombination bump $(l < 100)$. This is not possible or severely restricted from the ground as the entire sky is not visible from all points on Earth. This restricts measurement to low-l, with the BICEP/Keck array managing go down to as low as $l = 70$.

2.4 Summary and Discussion

Improvements in the observation of the CMB polarisation signal have provided us new means of extracting cosmological and astrophysical information. Several prediction from fundamental physical theories can be probed through a careful observation of the CMB polarisation sky in the foreseeable future (2.1). The possible science results that can be achieved through a CMB polarisation mission are numerous and have been details in several papers over the years including the most recent ones [56][67][42][60][61][59].

To achieve the required science goals a CMB space mission is ideal for providing the required sensitivity to polarisation over a large sky fraction and without the complexities faced by ground experiments. A CMB space mission will benefit from a full access to all relevant CMB frequency bands, a full sky coverage and a cold and stable environment to function in (2.3). Several such missions have been proposed over the last few years with the latest being CORE. Currently, LiteBIRD is the only programme undergoing a study phase.

CHAPTER 3

SCAN STRATEGY

The scanning strategy employed to observe the sky is an important aspect of a future CMB Polarisation space mission. The scanning strategy has a direct impact upon the polarisation sensitivity as well as on calibration, map making and severity of systematic effects.

The drivers behind a successful scan strategy for a future CMB polarisation space mission that proposes to meet the science goals mentioned above are:

- Provide a uniform sky coverage over a large sky fraction. Ideally, the cleanest parts of the sky away from the galactic centre should have the highest sensitivity to polarisation possible. This allows us to probe the low multipoles not possible from ground. If not for each individual detector, a full sky coverage should be possible using the detector set for each individual frequency band.

- Provide a good cross-linking of scan patterns and redundancy of measurement to ensure each sky pixel is sampled many times and at several angles of the detector polarisation axis. This ensures the ability to reconstruct all sky polarisation maps using single detectors. Single detector maps have the advantage of not encountering contamination from certain systematic effects that affect pair differencing experiments. (We study this in detail in the subsequent chapters). For CORE and LiteBIRD we achieve a complete scan of the entire sky in half a year and achieve a symmetric scan at each ecliptic latitude in one year.

- Observe the same sky pixel on both short and long time scales to increase the effectiveness of calibration and estimation of long time drifts in the signal. Revisiting the pixels on a time scale that is the inverse of the knee-frequency of low frequency drifts reduces their impact.
- Position the instrument in a suitable orbit with proper shielding to ensure thermal stability and reduce the absolute temperature of the payload. A stable environment will reduce long time drifts that may be correlated between detectors and reducing the absolute temperature of the payload will reduce the thermal loading.

3.1 The CORE scan strategy

The CORE instrument was proposed to be put into a Lissajous orbit about the second Sun-Earth Lagrange point ($L2$). As a departure from the *Planck* scanning strategy, which employed large circular scans crossing near the ecliptic poles, CORE as well as LiteBIRD will employ a combination of two rotational motions, a precession of the entire payload and a spin (Figure 3.1). This will enable cross-linking of scan paths and a passive modulation of the detector polarisation angle. Additionally, there will be the motion around the Sun over a period of 1 sidereal year. There have been different incarnations of the CORE mission with related instrument design over the past few years and they share the scanning philosophy employed in the latest proposal for the $M5$ slot.

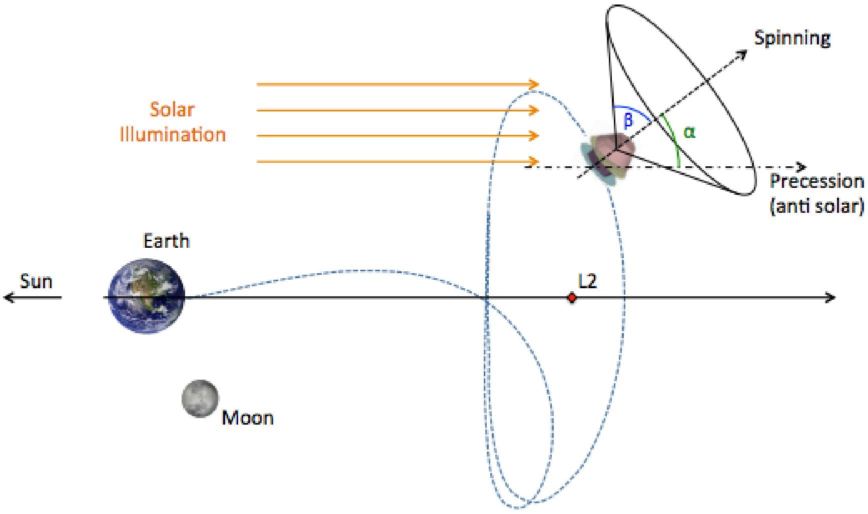

Figure 3.1: Illustration of the orbit of the proposed CORE mission about the $L2$ Lagrange point. The instrument will perform three rotational motions; a long precession about the anti-solar axis, a fast rotation about the spin axis and a rotation about the Sun over 1 sidereal year.

3.2 Scan Parameters

The scanning pattern of an instrument such as CORE or LiteBIRD , that will be placed at the Sun-Earth $L2$ Lagrange point, can be determined from a simple set of scan parameters. By varying these parameters, we can achieve different configurations of scan strategies, each of which will impact the effectiveness of different aspects of the mission. In order to determine the possible limits and optimise the different scan parameters we calculate how they are related to each other, and to the design requirements and physical restrictions. We shall refer to (Figure 3.2) to first define the scan parameters and then calculate our required relations.

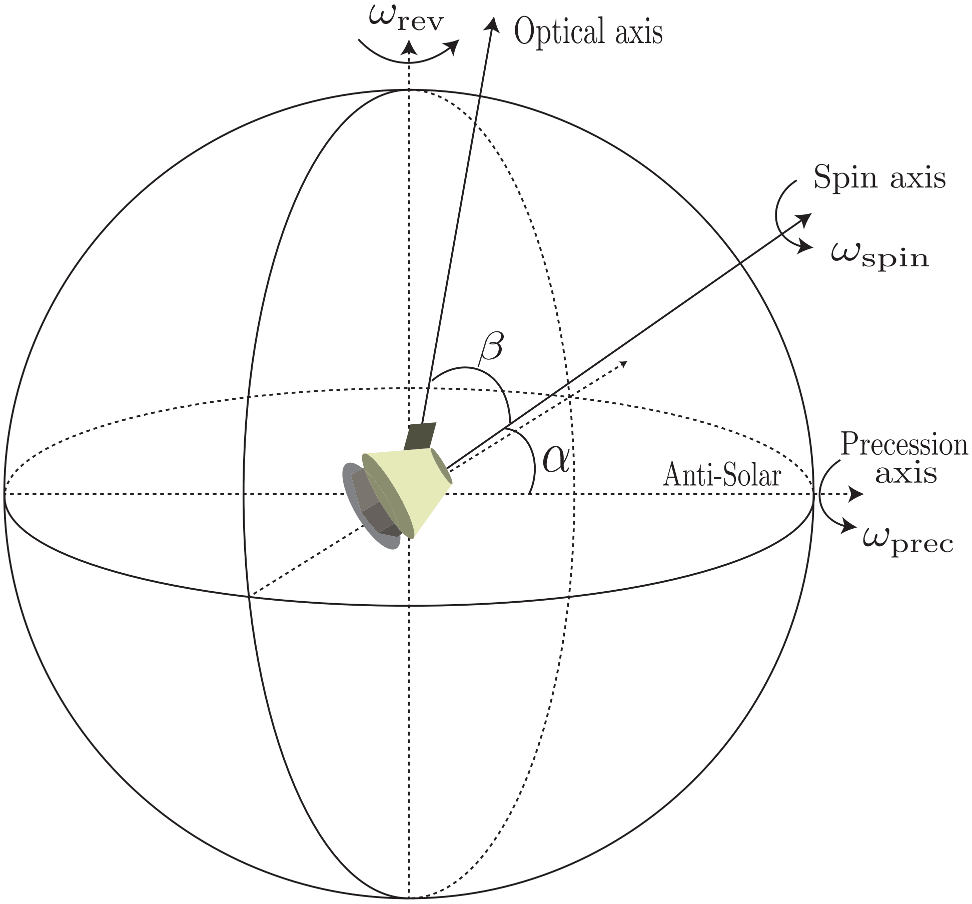

Figure 3.2: The figure illustrates a CORE type scan strategy with the instrument placed at the origin of our reference frame. The different rotations and their corresponding axes are marked.

The key scan parameters and properties for a CORE type scan strategy are as follows,

- Revolution of the entire system around the Sun in a period of 1 sidereal year with angular velocity ω_{rev}.
- Spinning of the instrument about its spin axis with a period of T_{spin} and angular velocity ω_{spin}.
- Opening angle of the optical axis from the spin axis with an angle of β.
- Precession of the instrument about the Anti-Solar axis with a precession period of T_{prec} and angular velocity ω_{prec}.
- Precession axis aligned with the Anti-Solar axis and the spin-axis making an angle of α with the precession axis.
- The detectors will be sampling with a sampling frequency of f_{samp} and time between each sample being T_{samp}.
- The instrument revolves around the sun over a period of 1 sidereal year, $T_{\rm rev}$ and is a constant.

Although these parameters can have a wide range of values, mission requirements place certain constraints upon them. We calculate now how these restrictions limit the range of our parameters and how they are related to each other.

Note that we have not included a half-wave plate when defining the scan parameters since we are studying primarily the case for the CORE mission. Addition of a half-wave plate to actively modulate the polarisation angle constitutes a completely different class of scan strategies.

- **Radiation shielding and Thermal Stability** : The thermal load on the instrument is determined by the amount of incident solar radiation. Hence, the precession axis is ideally oriented along the Anti-Solar axis. Radiation from the Sun, Earth and Moon should never enter the enclosure of the payload. To ensure this, the Solar aspect angle θ_{Sun} must never exceed a maximum value $\theta_{\text{Sun}}^{\text{MAX}}$ determined by the geometry of the shielding. Similar relations apply for θ_{Earth} and θ_{Moon}.

- **Full Sky Maps** : The instrument optical axis makes an angle of $\alpha+\beta$ with the anti-solar axis. The detectors being spread out over the focal plane, the extreme most detectors will be offset from the optical axis, when projected onto the sky, by an angle of $\triangle\beta^{\text{MAX}}$. Hence, for all the detectors to be able to scan the entire sky over a period of 6 months we must impose the relation,

  $$\alpha+\beta-|\triangle\beta^{\text{MAX}}| \geq 90° \tag{3.1}$$

  Not conforming to this requirement leaves out unobserved holes at the Ecliptic poles. Full sky coverage by all detectors is, however, not a strict requirement and a full sky coverage by all frequency bands can be achieved with appropriate distribution of detectors over the focal plane.

- **Co-scan Sampling** : The CORE proposal calls for a dense scan along the direction of scanning. We can visualise the optical axis tracing out consecutive circles on the sky, each of length $360\times60\times\sin(\beta)$ arcminutes. The angular separation between consecutive data samples $\theta_{\parallel}$, in arcminutes, is

  $$\theta_{\parallel} = 360\times60\times\sin(\beta)\times\frac{T_{\text{samp}}}{T_{\text{spin}}} \tag{3.2}$$

  The instrument beam determines the smoothing scale of the sky. As a rule of thumb we want 4 samples along the scan direction per beam full width half maximum (FWHM). In the CMB frequencies, the CORE proposal has, for example, a beam of $8.51'$ FWHM at 130GHz [56]. Hence, we want $\theta_{\parallel}$ to be close to $2'$.

- **Cross-scan Sampling** : Due to the precession, the spin axis will trace out a circle of length $360\times60\times\sin(\alpha)$ arcminutes. Each of the circles traced out by the optical axis will be centred on this circle and spaced consecutively at angular separation of $\theta_{\perp}$. In arcminutes, it is

  $$\theta_{\perp} = 360\times60\times\sin(\alpha)\times\frac{T_{\text{spin}}}{T_{\text{prec}}} \tag{3.3}$$

A dense scan of the sky requires similar constraints on $\theta_\perp$ to that of $\theta_\parallel$ that depend on the beam size. It is preferred to have consecutive circles close to each other that do not to leave large gaps.

3.3 Classification of Scan Strategies

Using the relations described in section (3.2) we now classify and calculate examples of possible scan strategies for a CMB space mission. We first make a classification of the different possible scenarios due to choices of scan parameters.

- **$\alpha < \beta$ vs $\alpha > \beta$:** Due to the two rotational motions of the instrument, the optical axis traces out an annular pattern on the sky over the period of one precession, and under the special case of $\alpha = \beta$ it traces out a disc. The major and minor radii of the annular pattern are given by $\alpha + \beta$ and $|\alpha - \beta|$ respectively. With different values of α and β we encounter two scenarios of the scan path cross-linking when $\alpha - \beta$ is either positive or negative. The two scenarios are illustrated in (Figure 3.3).

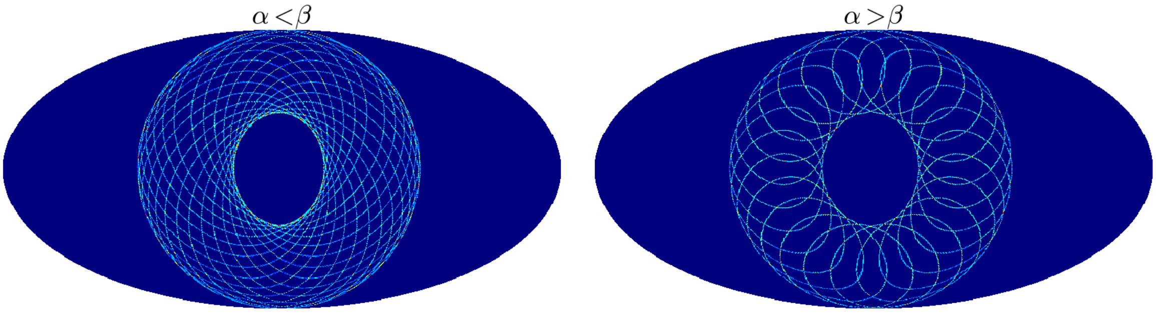

Figure 3.3: The two scenarios for the combination of the α and β scan parameters give markedly different cross-linking patterns. In this illustration, the first scenario has $\alpha = 30°$ and $\beta = 60°$, and the second scenario has $\alpha = 60°$ and $\beta = 30°$. The spin periods have been exaggerated so as to illustrate clearly the cross-linking patterns.

Choosing either case has implications for single detector scans. In the case with $\alpha > \beta$, the range of angles by which each sky pixel is visited is large for most of the sky. This ensures a good conditioning of the covariance matrix (described in (4.2)) and the ability to construct single detector intensity and polarisation maps. The alternative case of $\alpha < \beta$ visits each sky pixel with fewer variations of the detector angle and hence would require at least 2 detectors with orthogonal polarisation angles to reconstruct sky maps over a short period. It however observes regions of the sky that are separated by a large angular distance over a short time period and might prove advantageous for calibration.

- **Long vs short precession period:** The relation between the two major time periods T_{prec} and T_{spin} determines the manner in which the sky is filled up. A long precession period allows for consecutive circles to be closely packed along consecutive spin periods. Conversely, a short precession period that is comparable to the spin period leaves out large gaps which are filled up during successive precession periods. The effect of this is clearly visible in the figure (Figure 3.4). Configuration A with a long precession period and a dense cross-scan sampling produces a much more uniform coverage per precession period as compared to configurations B and C which have a short precession period.

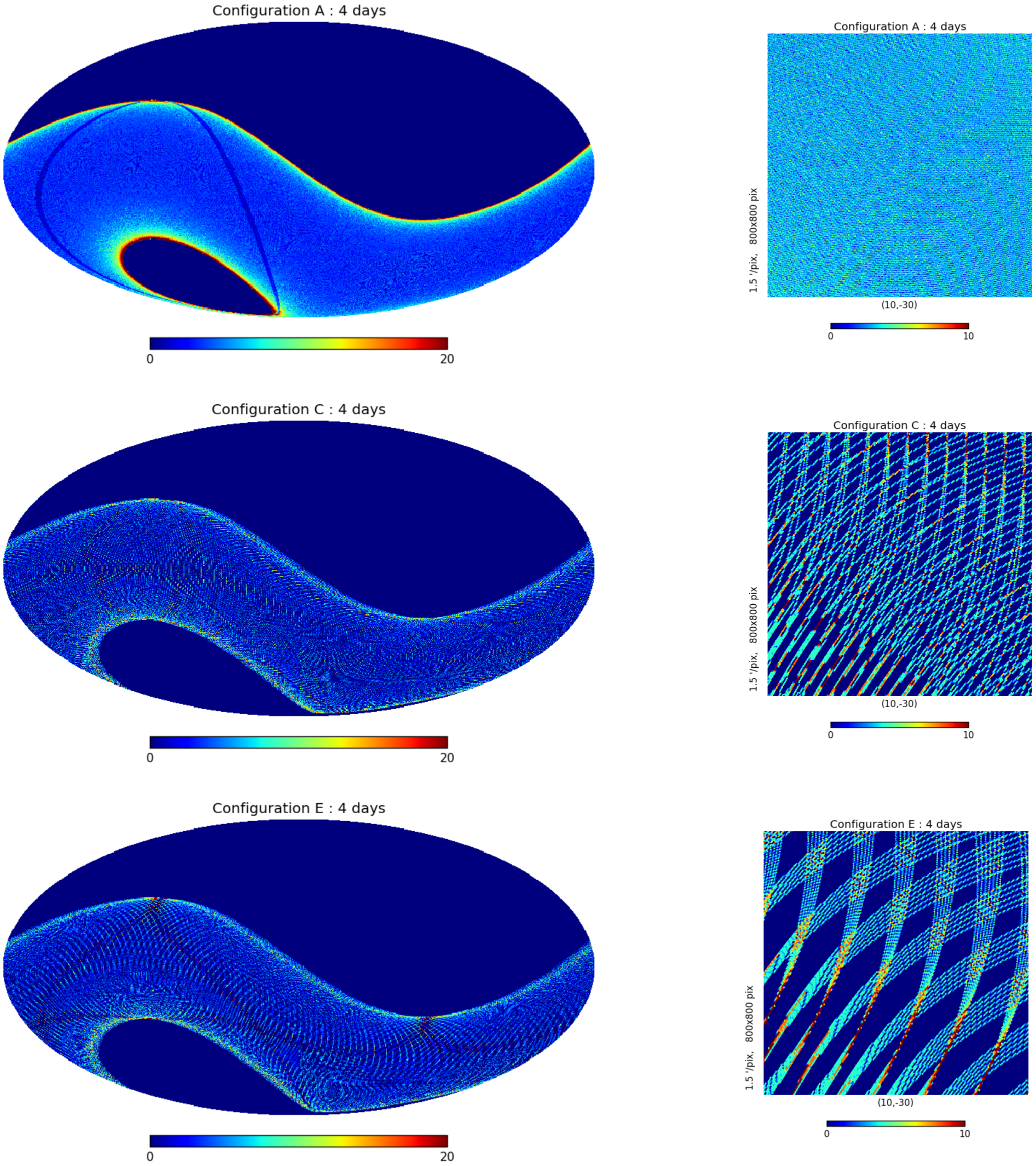

Figure 3.4: Mollview and gnomview plots at (lat,lon) $=(10°,-30°)$ for the hitcount maps for Configurations A, C and E for a duration of 4 days. This demonstrates the effect of a dense scan (Configuration A) against a sparse scan (Configuration C and E) achieved by having a long and short precession period respectively. The effect of having the ratio of $T_{\rm prec}$ to $T_{\rm spin}$ as irrational is demonstrated by the difference between Config C and Config E.

3.4 Example Scan Strategies

Using the above derived relations, five unique cases of scan strategies are listed below with an attempt to cover the different classes of scan strategies that can be possible. These strategies can be classified as having either a long (Configurations A and B) or a short (Configurations C, D, and E) precession period. We also classify according to the relation between the precession (α) and opening (β) angles. For the case of $\alpha < \beta$ we have Configuration A and the rest have $\alpha > \beta$. In all these cases we have kept the sum $\alpha + \beta = 95°$ so as to achieve a full sky coverage over a period of half a year. Configurations A and B correspond to scan strategies developed for a CORE like mission whereas C, D and E are those that are being developed for LiteBIRD.

Two other variants of this class of scan strategies need mention. The *Planck* satellite utilised a large opening angle $\beta = 85°$ to scan distant regions of the sky on large circles with a high redundancy on a short timescale. This proved advantageous in terms of calibration, map-making and other aspects of data analysis, however, the strategy was ill suited for polarisation observation as the same pixel was approached at practically the same angle by each detector.

The opposite of the *Planck* case was that proposed for PIXIE where $\beta = 0$. This would have allowed each sky pixel to be observed by several angles of the detector polariser on very short timescales.

Name	α	β	T_{prec}	T_{spin}	f_{samp}	$\theta_{\parallel}$	$\theta_{\perp}$
Configuration A	$30°$	$65°$	4 days	120 s	85 Hz	$1.92'$	$3.75'$
Configuration B	$50°$	$45°$	4 days	90 s	85 Hz	$2.00'$	$4.31'$
Configuration C	$65°$	$30°$	1.603 hours	600 s	10 Hz	$1.80'$	$33.92°$
Configuration D	$50°$	$45°$	1.603 hours	600 s	10 Hz	$2.55'$	$28.68°$
Configuration E	$65°$	$30°$	1.55 hours	600 s	10 Hz	$1.80'$	$35.08°$

Table 3.1: Scan configurations

An important observation that can be made between the scan strategies adopted by the two classes of future proposed missions CORE and LiteBIRD is the scan density. While CORE goes for a very tight scan density with $\theta_{\perp}$ being a few times smaller that the beam size in the CMB frequencies [56], the fast precession of LiteBIRD means that it will have a very sparse cross-scan sampling. This can be visualised from the scan density obtained after 4 days of scanning using the three Configurations A, C and E in (Figure 3.4).

For the case of fast precession, it runs the risk of scan circles from consecutive precession periods overlapping creating resonance patterns that also show up in the polarisation sensitivity maps (Figure 3.8). To overcome such a situation a solution proposed in [68] of using irrational numbers as the ratio between spin and precession periods is used to construct Configuration C and D. The effect of using such ratios is evident from (Figure 3.4) by comparing configurations C and E. For configuration E, the scan paths from consecutive precession periods pass very close to each other and over the course of several periods gives rise to resonance patterns on the sky. This effect will be more prominent on a longer scan duration and affect polarisation sensitivity as we will see in section (3.6).

3.5 Sky Coverage and Cross-Linking

The sky coverage over a single precession period, by each annular ring in (Figure 3.3), can be calculated by integrating over the surface traced out (in the ecliptic coordinates) by the optical axis. It is given by,

$$
\begin{aligned}
f_{\text{sky}} &= \frac{1}{4\pi}\int_{|\alpha-\beta|}^{\alpha+\beta} 2\pi \sin(\theta)\, d\theta, \\
&= \frac{1}{2}\left[\cos\left(|\,\alpha-\beta\,|\right) - \cos\left(\alpha+\beta\right)\right]. \qquad (3.4)
\end{aligned}
$$

For example, assuming a dense scan like that of Configuration A, we achieve a sky coverage of $\approx 46\%$.

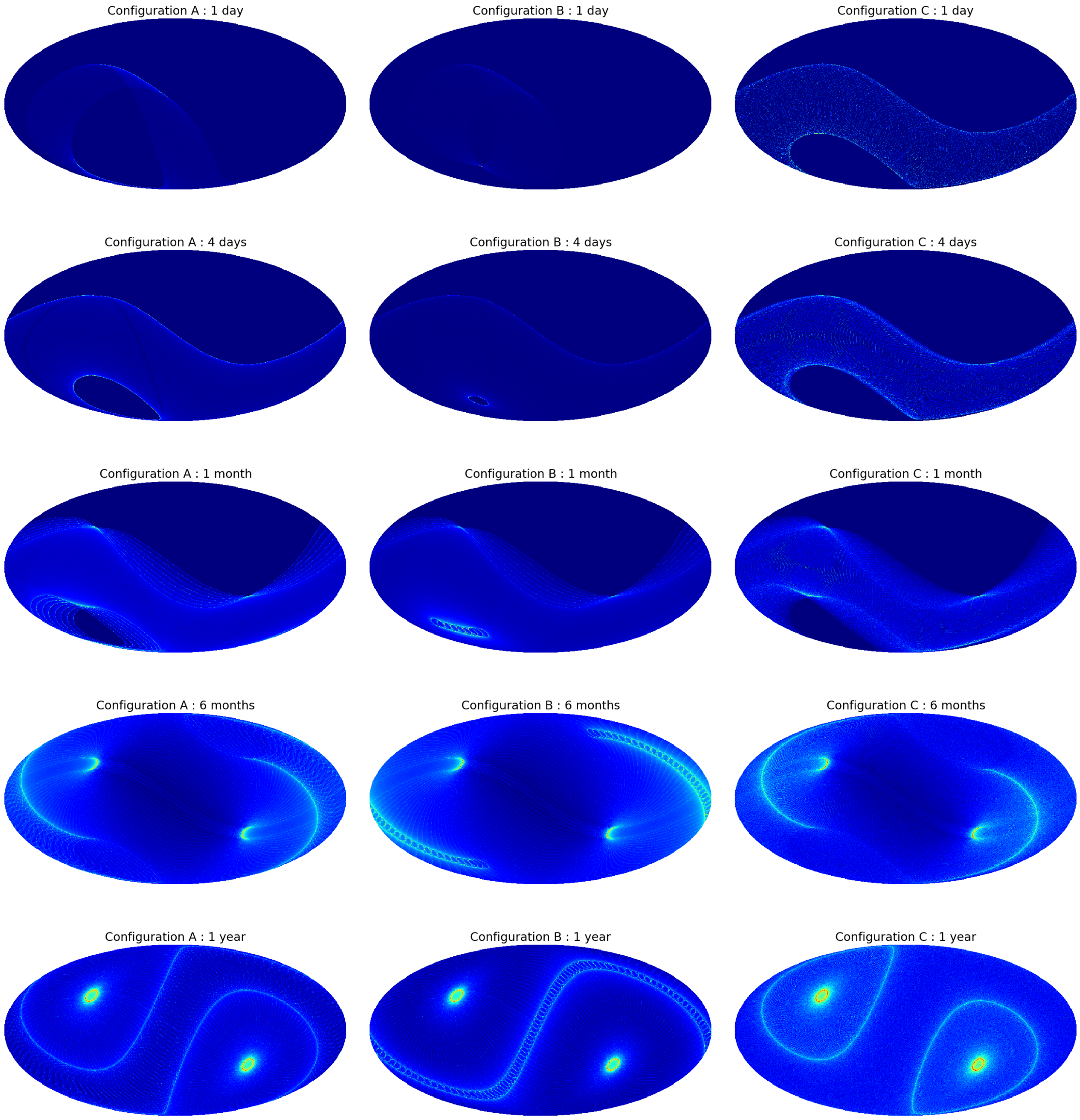

Figure 3.5: These figures illustrate the evolution of the hitmap for three configurations A, B and C of scan parameters. The scan Configurations so chosen belong to three different sets of α and β scan parameters used in (Table 3.1). The three sets of (α,β) are: $(30°,65°)$ for A, $(50°,45°)$ for B, $(65°,30°)$ for C.

Over the course of a year, the sky is progressively filled up, as shown in (Figure 3.5), making a full sky coverage in 6 months for all 5 configurations that have been studied. This is ensured by fulfilling the full sky coverage condition (Equation 3.1). Despite each detector performing a full sky coverage in 6 months, there is an asymmetry along each ecliptic latitude. A symmetry under rotation about the ecliptic polar axis is only achieved after a full year of scanning. There are, however, finer structures in the scan density produced on the ecliptic latitudes. This is caused by the annular ring from a single precession repeating itself every precession period after having moved by an angular distance of $2\pi T_{\mathrm{prec}}/T_{\mathrm{year}}$ on the ecliptic equator. This effect is more pronounced for long precession periods as in configurations A and B.

The CORE and LiteBIRD like scan strategies also produce three distinctive regions of scan. They produce a band about the ecliptic equator with a width of $2|\alpha-\beta|$, a circular patch at the ecliptic poles of radius $\alpha+\beta-90°$ and the remaining region between these two forming the third. Each of these regions have a different cross-linking pattern, scan density and polarisation sensitivity and is determined by the choice of scan parameters.

3.6 Polarisation Reconstruction and Sensitivity

The Stokes I, Q and U maps are reconstructed from the timestream data using the map-making equation (Equation 4.7). Since, for each *HEALPix* pixel, we have 3 unknowns, it is necessary for each pixel to be observed with three unique polarisation angles between 0 and π. Without any half-wave plate to actively modulate the polarisation angle, the scanning strategy alone must guarantee this if single detector maps are to be generated. For example, the Planck scanning strategy was ill suited for this purpose as it allowed very little variation of the polarisation angle per detector. The scanning strategy for the CORE proposal and LiteBIRD provides better angular coverage by means of the scanning strategy alone.

The 6 independent elements of the pixel-pixel covariance matrix (Equation 4.8) provide us a measure of the sensitivity achieved by any particular scan. The diagonal terms measure the noise variance and the off-diagonal terms give a measure of the cross-correlation between the Stokes (I,Q,U) parameters for each *HEALPix* pixel. It can be taken as a measure of the quality of scanning and ability to reconstruct accurate polarisation maps for different scanning strategies. A good scan strategy is characterised by a covariance matrix that is close to the ideal case. The ideal case is when the off-diagonal terms tend to 0 and the II term tends to half of the QQ and UU terms (Equation 4.11). The histograms of the diagonal terms for a good scan strategy should be compact about their mean values without having considerable tails and the histogram of the off-diagonal terms should be negligible and as close to zero as possible.

We plot here in (Figure 3.6) and (Figure 3.7) the evolution of the 6 independent terms in the pixel covariance matrix for Configurations A and B. These also represent the two cases of $\alpha-\beta$ as discussed before. The effect of having two detectors with orthogonal polarisation axes is also compared to the single detector case. In the *HEALPix* convention, for the single detector, the initial angle of the polarisation axis was at $0°$ when the optical axis was at its highest point at the beginning of the scan. The second detector in the 2 detector case was at $90°$. The choice of these angles influence the shape and distribution of the polarisation terms in the covariance matrix. A rotation of $45°$ of the initial polarisation axis will flip the covariance matrix elements for the Q and U terms.

The mean theoretical sensitivity for each of the cases is drawn with the vertical lines to provide a reference. All simulations and calculations have been done in galactic coordinates.

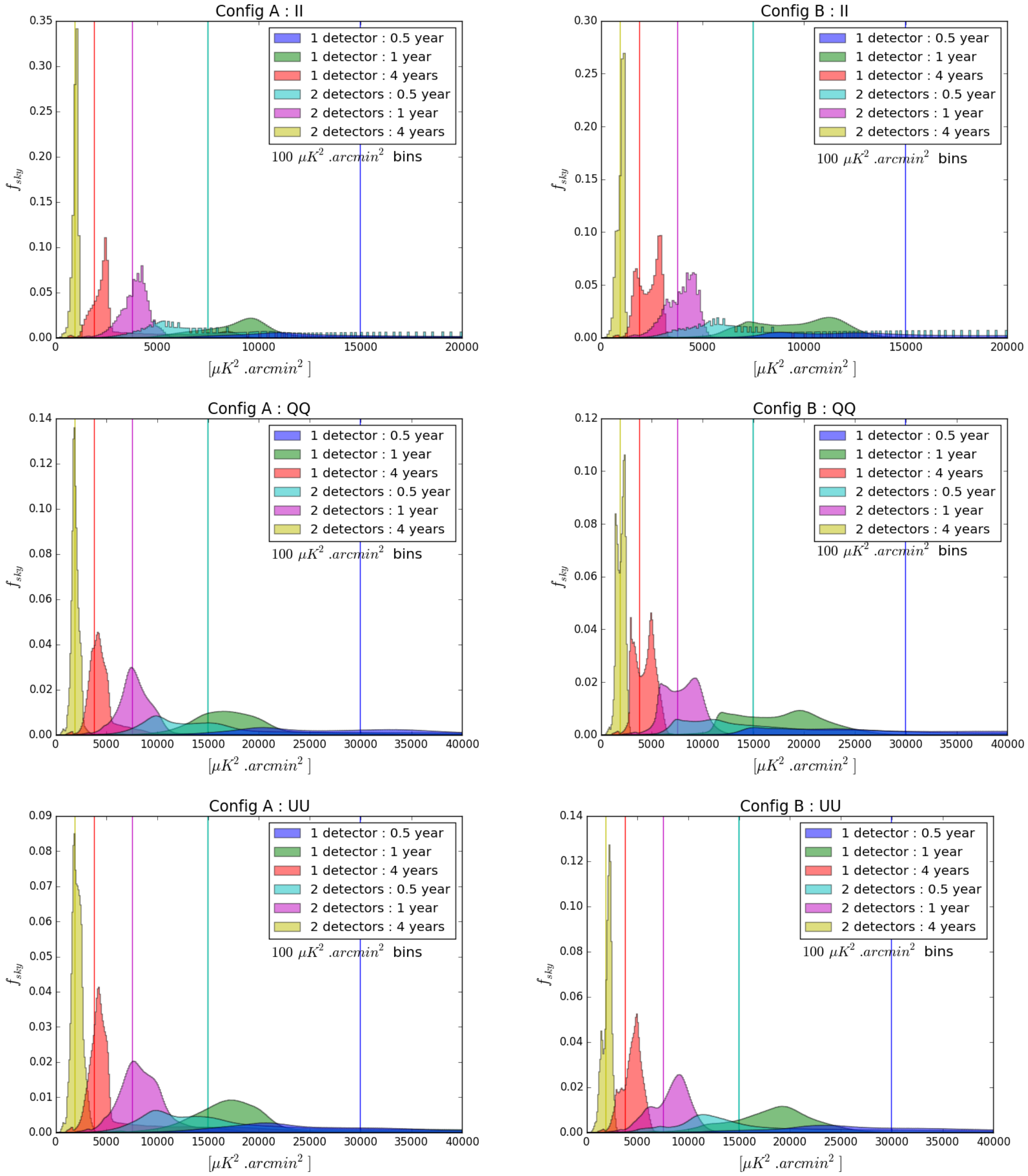

Figure 3.6: Evolution of the diagonal covariance matrix elements over the course of a survey. The case for a single detector and a detector pair with orthogonal polarisation direction is demonstrated. The vertical lines show the theoretical mean sensitivity for the given scan period.

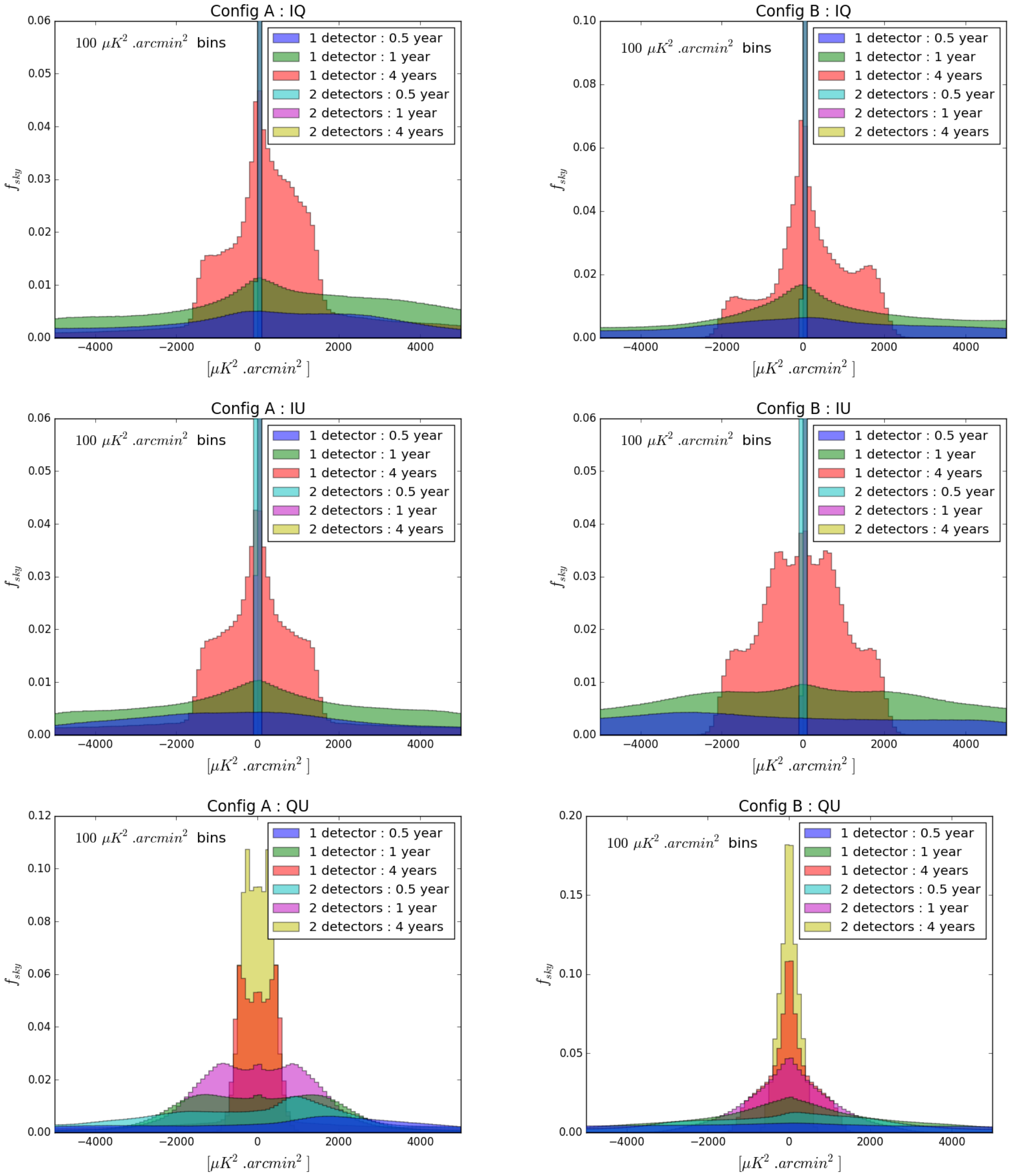

Figure 3.7: Evolution of the off-diagonal covariance matrix elements over the course of a survey. The case for a single detector and a detector pair with orthogonal polarisation direction is demonstrated.

The first conclusion to be drawn from these two sets of plots is that for the single and double detector case, the diagonal elements have a considerable tail for scan periods of half a year for both configuration A and B. A considerable number of pixels are therefore at a much higher noise variance than the ideal value depicted by the vertical lines. The off-diagonal term for the single detector alone for a half year scan is spread very widely about 0. We can infer that with a single detector is is not possible to make an all sky map for a scan period of half a year with either configuration A or B. The detector pair will be capable of making all sky polarisation maps but a significant number of pixels will have a high noise variance.

For the case of a full year scan with a single detector, either configuration fare significantly better than the half year scan with much tighter diagonal terms but still with a high noise variance when compared to the theoretical mean. The configuration B fares visibly better for TT and QQ and less so for UU, as can be seen from the significantly more sky coverage below the theoretical mean. The asymmetry between Q and U can be attributed to the choice of polariser angles.

The significant improvement for configuration B over A for a four year scan with a single detector is clearly visible from the lack of a thick tail in all 6 of the covariance terms.

For scans with the orthogonal detector pair, the covariance matrix terms are distributed in a compact manner about the mean and the cross terms are significantly narrower, the IQ and IU being practically 0.

An important aspect to investigate is what is the sensitivity going to be and how it is distributed on the sky when a full survey of 4 years is conducted by an array of detectors. We consider here an array of 36 detectors, arranged on the focal plane on 9 parallel rows, each separated by $9.875'$. Each row contains 4 detectors in an optimal configuration. The maps so obtained are rescaled for a set of 144 detectors, the full $145\mathrm{GHz}$ channel for the CORE proposal. The presence of the ideal configuration produces a pixel covariance matrix that is proportional to (Equation 4.11). Due to this the polarisation sensitivity is independent of the orientation of the detector polarisers, as was in the previous case of single and detector pair, and is governed solely by the hitcount distribution on the sky. The polarisation sensitivity is simply given by the elements QQ or UU of the covariance matrix. All simulations and calculations were done in the galactic coordinate system. The noise considered is white and simulated for the $145\mathrm{GHz}$ channel in [56] at a per detector sensitivity of $39.9\mu\mathrm{K}\sqrt{\mathrm{s}}$.

We plot in (Figure 3.8) the polarisation sensitivity map for all five cases of scan strategies in (Table 3.1). We also plot the cumulative histogram and histogram for the same polarisation sensitivity maps in (Figure 3.9) (Figure 3.10).

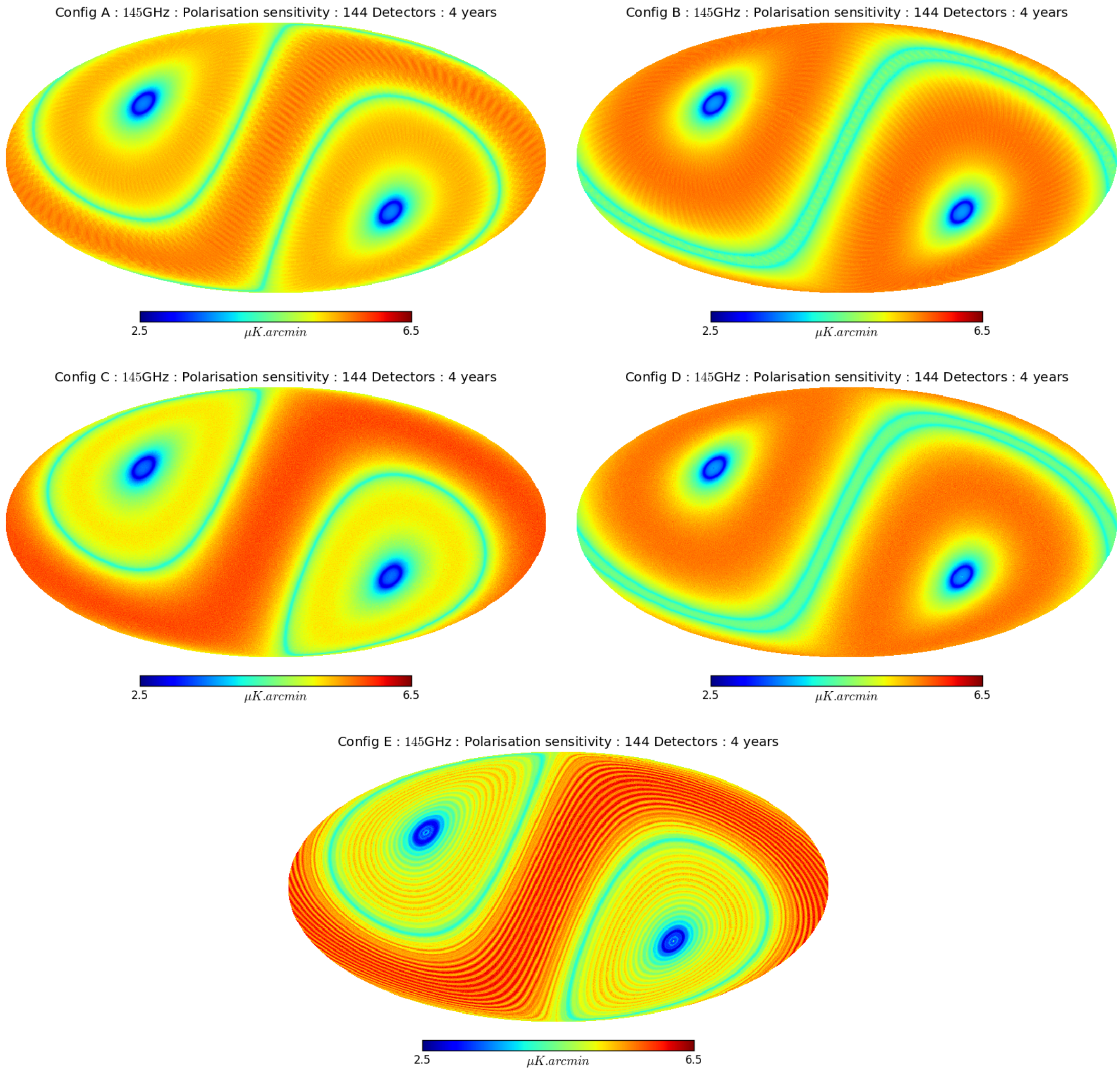

Figure 3.8: These polarisation sensitivity maps display the QQ component of the covariance matrix that has been rescaled to units of $\mu\mathrm{K.arcmin}$. This directly shows the sensitivity to polarised signal from a scan of 4 years by a set of 144 detectors spread over a section of the focal plane.

We see that all 5 configurations have a significant spread about the mean theoretical sensitivity of $\approx 5.1\mu\mathrm{K.arcmin}$ ranging from about $\sim 4.0\mu\mathrm{K.arcmin}$ to $\sim 6.0\mu\mathrm{K.arcmin}$ as can be quantified from the histogram (Figure 3.10). Beyond this, a very small sky fraction is covered by all the example configurations, except E.

The best constraint on the sensitivity is for configurations A,B and D. A and B being the class of CORE like scan strategies and D sharing the same angles α and β as B. Surprisingly, configuration C with a higher α and smaller β has two distinct regions of high and low sensitivity, with the high sensitivity region being concentrated in the patch of radius $90° - |\alpha - \beta|$ around the ecliptic poles. This sensitivity profile is shared by A but less distinctly. For B and D the situation is reversed with the patch around the poles being less sensitive than the equatorial band.

All 5 strategies show a deeply scanned region at the ecliptic poles at $\approx 3\mu\mathrm{K.arcmin}$.

The worst performance is by configuration E which shows several undesirable features. It has visible resonance patterns, due to a poor choice of precession and spin period, which contributes adversely to its polarisation sensitivity. Although it shares the same α and β angles with configuration C, it lacks its good features of a peak at high sensitivity. E in fact has a strong peak above $\sim 6.0\mu\mathrm{K.arcmin}$, highest among all the 5 sample strategies.

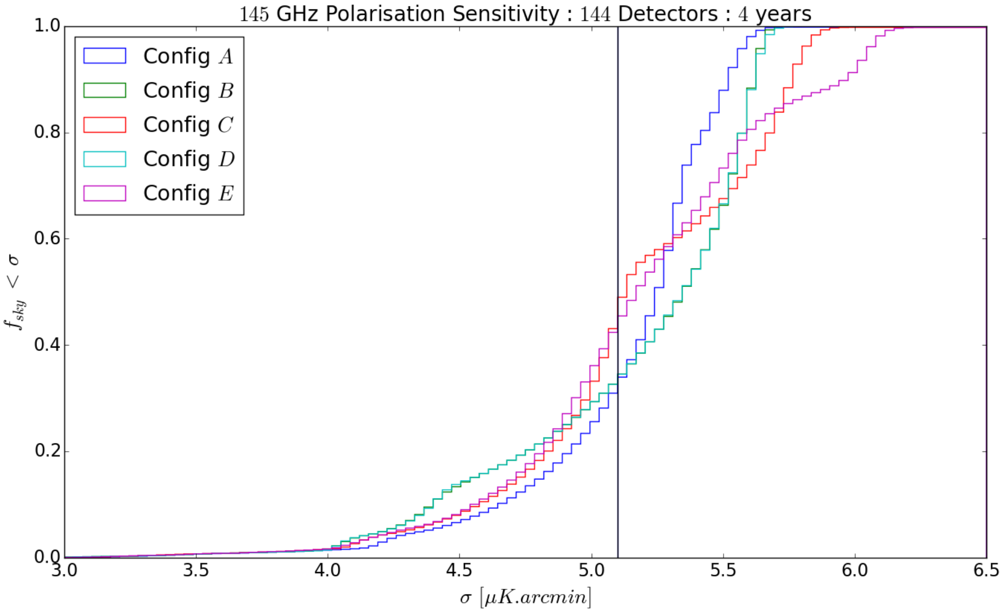

Figure 3.9: Polarisation sensitivity cumulative histogram. $0.03\mu\mathrm{K.arcmin}$ bins.

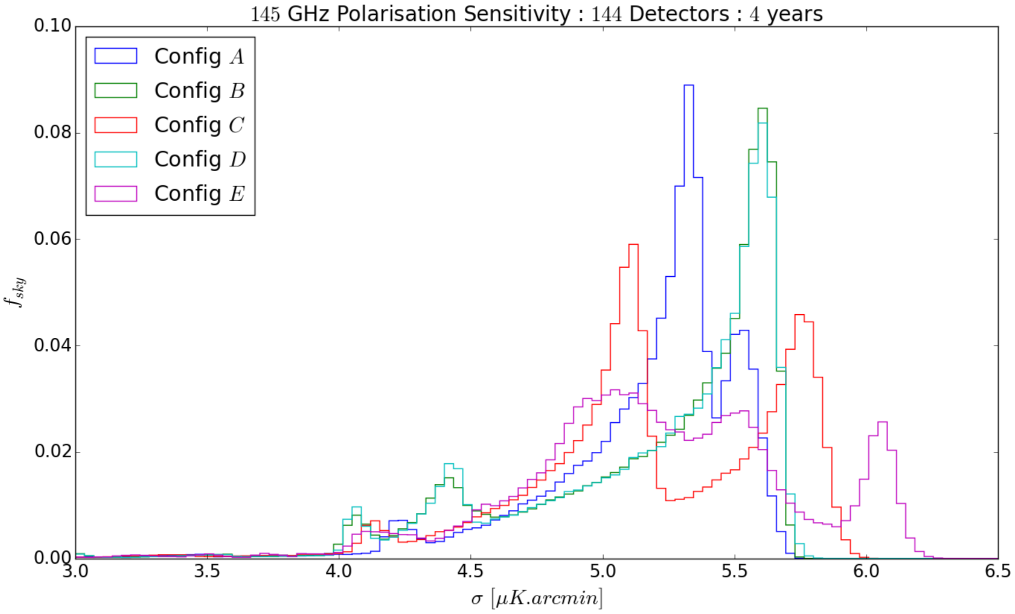

Figure 3.10: Polarisation sensitivity histogram. $0.03\mu\mathrm{K.arcmin}$ bins.

3.7 Summary and Discussion

The scan strategy is an important design driver for a CMB polarisation space mission. It has a direct impact on the ability to reconstruct polarisation and the mission's polarisation sensitivity. It also impacts calibration and data analysis techniques. The scan strategy of a mission can be defined in terms of a few scan parameters (3.2) and can be classified by the specific choice of these parameters (3.3). The CORE and LiteBIRD like scan strategies observe the entire sky in a symmetric fashion in 1 year (3.5). They provide a passive modulation of polarisation angles by scanning alone, the quality of which depend on the particular choice of the parameters.

I observe that a single detector scan over 6 months does not have the ability to reconstruct an all sky-map for either configuration A or B. This improves over time as the sky pixels are observed at more and more angles. Configuration B is better suited for single detector map making. This is in general the case for the class of strategies with $\alpha > \beta$ of which B is a example. The polarisation sensitivity maps, for a 4 year scan with the full $145\mathrm{GHz}$ channel of CORE [56], show the variation of the sensitivity over the map and divides it into 3 distinct regions (3.6). All the example strategies have comparable sky coverage at any particular sensitivity but their distribution is different (Figure 3.9) (Figure 3.10). Configuration E is, however, undesirable due to the production of artefacts from resonant scan patterns.

CHAPTER 4

SYSTEMATICS CORRECTION MAP MAKING

Current generation CMB experiments employ arrays of detectors such as Transistor Edge Sensors (TES) or Kinetic Inductance Detectors (KIDS) to scan the sky in the microwave frequencies. For example, *Planck* employed 74 bolometers in 9 frequency bands from 30 to $857\mathrm{GHZ}$ [69], SPT-3G employs $15{,}234$ bolometers with multi-chroic pixels in three frequency bands at 95, 150 and $220\mathrm{GHz}$ [70] and the CORE mission proposal has 2100 detectors in 19 frequency bands [56]. Assuming that photon noise is the main contributor to the overall noise budget, as is the case with space missions such as *Planck* and as planned for future space mission such as CORE or LiteBIRD, the only way to achieve higher sensitivity is to add more detectors. Aggregating the signal obtained from several detectors reduces the noise on the final maps. As discussed in the (Chapter 2), the next generation of CMB experiments will aim at going down to a sensitivity of the order of $\delta r \sim 10^{-3}$ equivalent to achieving a sensitivity of $\sim 2\mu\mathrm{K.arcmin}$ on the map.

In reality, observing the CMB sky signal is not trivial and the next major challenge in CMB polarisation data analysis is going to be in the domain of foreground subtraction, systematics correction and delensing [63][57][61]. As seen in Planck, the error due to systematic effects from the instrument chain or from detector non-idealities already surpass the stochastic noise. Cleaning the contamination from systematic effects needed extensive end-to-end simulations, characterisation of the time-ordered-data (TOD) and development of correction methods [71][72][73]. For future space missions, the systematics will contribute a significant amount to the error budget and will restrict our search for primordial CMB B-modes if not properly addressed to minimise their impact. It is thus vitally important to tackle the problem of systematics at three different levels. Firstly, optimise instrumental designs to minimise the level of systematics. Secondly, optimise the scanning strategy in order to reduce the effect or to allow for better control of systematics at the analysis stage. Thirdly, model the known forms of systematic effects and develop methods to estimate and correct for these effects at the data analysis stage. In this thesis we focus on the latter two. The previous chapter discussed some important points about the scanning strategy and how it affects the reconstruction of I, Q, U polarisation maps. In this chapter we develop a map-making technique that mitigates some of the main systematic effects at the analysis stage, and de-biases our measurement of the polarisation maps.

4.1 Known Systematics in Past and Current Experiments

In the context of a future CMB space mission it is convenient to start from the set of systematic effects that have been observed in the *Planck* mission. Several sources of systematic effects were studied in [74] and in [72] and serve as a reference. Some of the most important effects that have been noted are beam asymmetry and mismatch, gain mismatch and stability, bandpass mismatch, pointing uncertainty and polarisation angle uncertainty (Table 4.1).

Name	Origin	Description	Major mode of leakage
Bandpass Mismatch	Spectral Filters	Edges and shape of the spectral filters vary from detector to detector. Can be thought of as a spectral source-dependent gain variation between detectors.	I → P
Beam Mismatch and Asymmetry	Optical beams	Beam shape differs from an ideal Gaussian form.	I → P E → B
Pointing Uncertainty	Attitude control, pointing reconstruction	Detector pointing at location different from that given by reconstructed pointing data	I → P E → B
Polarisation misalignment	Detectors	Uncertainty in polarisation calibration. Polarisation axis misaligned with measured direction.	E → B
Gain mismatch and stability	Detectors and Calibration	Gain calibration mismatch between detectors. These could also be variable over time.	I → P

Table 4.1: Different types of systematic effects are listed in this table mentioning the source of the effect, a short description and the mode by which the signal leaks (I = Intensity, P = Polarisation).

In general these systematic effects produce a leakage of signal from intensity to polarisation and from E to B modes. This was shown by extensive end-to-end simulations in [74] for the *Planck* LFI channels and their impact on the polarisation maps and spectra was demonstrated. To correct for such leakages, algorithms such as ‘SRoll’ [75] (for HFI) had to be developed along with sophisticated data analysis techniques. It is safe to say that the specific systematic effects and the manner in which they affect an experiment depends strongly upon the instrumental design and configuration. The effects listed in (Table 4.1) are relevant for any pair-differencing polarimetric imager such as CORE or LiteBIRD.

We study the impact of these systematic effects for the case of the CORE proposal in [57]. We do not implement a half-wave plate since the baseline design for CORE is without one. In the subsequent chapters we demonstrate the effect bandpass mismatch and beam ellipticity individually and in detail.

We proceed to develop a general framework for modelling the effect of systematics in a pair-differencing CMB experiment. Our approach is to develop a map making algorithm that filters out the intensity to polarisation leakage and produce unbiased polarisation maps.

4.2 Map Making

Map making is a key procedure in the analysis of CMB datasets and is the main theme for the subsequent chapters. Hence we give a brief review of map-making as applied to CMB observation. Some useful reviews on the topic include [76][77][78][79].

The signal acquired by the individual detectors is in the form of time-ordered data streams. Data in this format is not directly useful for the study of CMB anisotropies. The easiest way to extract useful cosmological information is to convert the raw time-ordered-data (TOD) to the CMB anisotropy power spectra. Going from the TOD to the power spectra is the domain of CMB data analysis and involves several stages. The initial stage which deals with data selection, cleaning and calibration does not fall within the scope of this thesis and varies widely from experiment to experiment. The next major stage in data analysis is to reconvert the cleaned and calibrated data back to sky maps and is known as map-making. These maps thus represent the anisotropies in the microwave sky as was observed by the instrument. Since these maps also contain contribution from diffuse galactic sources, extra-galactic compact sources and galaxy clusters, these components need to be estimated and cleaned to obtain the CMB anisotropy sky. This process known as foreground estimation and subtraction is an important step in obtaining maps of CMB signal alone but is not a focus of this thesis. Several map-making and foreground separation tools have been developed over the years for analysing CMB datasets, such as [80][81][82][83].

Once we have obtained the cleaned and calibrated timestream data with the monopole and dipole subtracted out we are ready to reconstruct the sky map. Making sky maps has an added advantage,

- Analysis of sky maps is a more intuitive approach than working with TODs. The astrophysical structures and the CMB anisotropies, predicted from theory, have a particular spatial distribution which become much more trivial to analyse from sky maps than from timestreams.

- Map making serves as a method of compressing time-ordered data of the order of PetaBytes down to a few sky maps of the size of a few GigaBytes.

- The noisiness of the raw timestream is reduced when the data is binned onto sky pixels. This makes it visually and analytically more trivial to observe the spatial structures on the sky.

To develop the map making process we first formalise our data model. Consider a detector, observing the sky at any particular frequency. We can write down the anisotropy signal observed at time index t as,

$$d_t = I_{\hat{\mathrm{p}}(t)} + Q_{\hat{\mathrm{p}}(t)} \cos\left(2\psi_t\right) + U_{\hat{\mathrm{p}}(t)} \sin\left(2\psi_t\right) + n_t, \tag{4.1}$$

where the sub-scripts represent the time and position of the measurement, $\hat{\mathrm{p}}(t)$ being the position observed at time t, d is the signal observed by the detector, (I, Q, U) are the Stokes parameters at the given position, ψ is the angle subtended by the detector polariser to the $North - South$ axis in the local coordinate frame and n is the random detector noise.

Sky maps reconstructed from the time-ordered data, consisting of $\mathcal{N}_{\mathrm{samp}}$ data points, will be projected onto pixelised *HEALPix* maps of size $\mathcal{N}_{\mathrm{pix}}$ and $p(t)$ will now represent the pixel observed in which the position vectors $\hat{\mathrm{p}}(t)$ fall in. The equation (Equation 4.1) can be formulated in the matrix-vector notation as

$$\boldsymbol{d} = \mathrm{A}\boldsymbol{S} + \boldsymbol{n}, \tag{4.2}$$

where, A represents the $\mathcal{N}_{\mathrm{samp}} \times \mathcal{N}_{\mathrm{pix}}$ pixel to time domain projection matrix. A is a sparse matrix with one non-zero entry per row given by

$$\mathrm{A}_{tp(t)} = \begin{bmatrix} 1 & \cos\left(2\psi_t\right) & \sin\left(2\psi_t\right) \end{bmatrix}, \tag{4.3}$$

$\boldsymbol{S}$ is the $\mathcal{N}_{\mathrm{pix}}$ sized vector of pixel-ordered Stokes parameters with each element given by

$$\boldsymbol{S}_p = \begin{bmatrix} I_p \\ Q_p \\ U_p \end{bmatrix}, \tag{4.4}$$

and $\boldsymbol{n}$ is the $\mathcal{N}_{\mathrm{samp}}$ element vector of the time-ordered noise in the timestream.

The total data set may be from a collection of independent detectors where their individual timestreams have been concatenated into a single vector $\boldsymbol{d}$ in the expression (Equation 4.2) and the projection matrix A being accordingly redefined. In order to reconstruct the sky map we need to invert the system given in (Equation 4.2) ensuring no loss in information [84]. Since we are solving for 3 unknowns (I, Q, U), this is possible only when we have at least 3 independent equations in the data set for any particular sky pixel. This is achieved by observing the same sky pixel with different polariser angles. Ensuring this condition, the map-making problem boils down to finding the best estimator of the Stokes parameters $\widehat{\boldsymbol{S}}$ given our knowledge of A and $\boldsymbol{d}$. The standard procedure is the Generalised Least Square (GLS) mapmaking, by minimising the chi-square,

$$\chi^2 = (\boldsymbol{d} - \mathrm{A}\boldsymbol{S})^T \mathrm{C}_{\mathrm{n}}^{-1} (\boldsymbol{d} - \mathrm{A}\boldsymbol{S}), \tag{4.5}$$

where C_{n} is the noise covariance matrix of size $\mathcal{N}_{\mathrm{samp}} \times \mathcal{N}_{\mathrm{samp}}$ given by

$$\mathrm{C}_{\mathrm{n}} = \langle n^* n \rangle. \tag{4.6}$$

In general, the noise n can be correlated between different detectors and between time samples, with a particular correlation length, and this leads to the noise covariance matrix C_{n} assuming the form of a Toeplitz matrix [85]. In the case where the noise parameters are stationary, the noise is uncorrelated between different time samples and has a white spectrum, C_{n} assumes a diagonal form and it simplifies down to $\sigma\mathbb{1}$, where σ is the standard deviation of the white noise.

Minimising the chi-square in equation (Equation 4.5) leads us to the minimum variance estimator for the Stokes parameters $\boldsymbol{S}$ given by

$$\hat{\boldsymbol{S}} = [\mathrm{A}^T \mathrm{C}_\mathrm{n}^{-1} \mathrm{A}]^{-1} \mathrm{A}^T \mathrm{C}_\mathrm{n}^{-1} \boldsymbol{d}. \tag{4.7}$$

The term $[\mathrm{A}^T \mathrm{C}_\mathrm{n}^{-1} \mathrm{A}]^{-1}$ is the covariance matrix and is a block matrix of size $\mathcal{N}_\mathrm{pix} \times \mathcal{N}_\mathrm{pix}$ with each block being a 3×3 matrix. As mentioned earlier, in the general case where C_n is not diagonal, the covariance matrix is also not diagonal. Estimation of the Stokes parameters is then possible only by a full conjugate gradient solution. However, in the case of a stationary white noise for which the noise covariance matrix is proportional to an identity matrix, we can simply drop the noise covariance term from our estimator.

In this thesis we work primarily with white noise and we discuss some properties of the estimator in the white noise case. The covariance matrix assumes a block diagonal form where each block element along the diagonal corresponds to a *HEALPix* pixel. The block for the pixel p is given by,

$$[\mathrm{A}^T \mathrm{C}_\mathrm{n}^{-1} \mathrm{A}]_p^{-1} = \frac{\sigma^2}{\mathcal{N}_\mathrm{hits}} \begin{bmatrix} 1 & \langle \cos(2\psi) \rangle & \langle \sin(2\psi) \rangle \\ \langle \cos(2\psi) \rangle & \frac{1}{2}(1 + \langle \cos(4\psi) \rangle) & \frac{1}{2}\langle \sin(4\psi) \rangle \\ \langle \sin(2\psi) \rangle & \frac{1}{2}\langle \sin(4\psi) \rangle & \frac{1}{2}(1 - \langle \cos(4\psi) \rangle) \end{bmatrix}^{-1}, \tag{4.8}$$

where $\langle \cdots \rangle$ represents an average over all the values that fall in the pixel p and $\mathcal{N}_\mathrm{hits}$ is the hitcount in that pixel.

The $[\mathrm{A}^T \mathrm{C}_\mathrm{n}^{-1} \boldsymbol{d}]$ part of the estimator re-bins the time-ordered data back to the pixel ordered space. It is a vector of size $\mathcal{N}_\mathrm{pix}$ with each element being given by

$$[\mathrm{A}^T \mathrm{C}_\mathrm{n}^{-1} \boldsymbol{d}]_p = \frac{1}{\sigma^2} \begin{bmatrix} \sum d \\ \sum \cos(2\psi)\, d \\ \sum \sin(2\psi)\, d \end{bmatrix}, \tag{4.9}$$

where the sum is over all samples which fall in the pixel p.

As we stated earlier, in the case of a stationary white noise, the noise terms σ^2 cancel out and we may write out our map-making expression as,

$$\hat{\boldsymbol{S}} = [\mathrm{A}^T \mathrm{A}]^{-1} \mathrm{A}^T \boldsymbol{d}. \tag{4.10}$$

4.2.1 Ideal Configuration

The diagonal elements in the covariance matrix are composed of sums of sines and cosines. By purely geometrical means, it is thus possible to make the off-diagonal terms go to 0. This is possible when the angles ψ are distributed evenly over π [86]. Modern CMB observation is carried out by detectors at right-angles from each other, either in the same focal plane pixel or in neighbouring pixels. Thus, an ideal configuration can be achieved with a set of 4 detectors at angles of $45°$. In reality, these 4 detectors need to be placed at different positions on the focal plane but it is possible to have an arrangement such that by a simple time-translation, the detectors may be considered as pointing at the same sky pixel. Under such an ideal configuration, the covariance matrix is given by,

$$[\mathrm{A}^T\mathrm{C}_\mathrm{n}^{-1}\mathrm{A}]_p^{-1} = \frac{\sigma^2}{N_{hits}}\begin{bmatrix}1 & 0 & 0\\ 0 & 2 & 0\\ 0 & 0 & 2\end{bmatrix} \tag{4.11}$$

In reality, we can never expect the covariance matrix to be exactly that of the ideal case. With careful focal plane designing or in the case of single detector map-making, with enough detector angles over several visits to the sky-pixel, we can expect the covariance matrix to approach the ideal case.

4.3 Signal Leakage due to Non-Idealities and Signal Mismatch

Detectors in the same frequency band under identical conditions of pointing and polariser orientation will observe the sky differently. This mismatch in the observed signal can be attributed to two reasons. Firstly, to random detector noise consisting of an uncorrelated part with a white spectrum and a correlated part having a 1-over-f spectrum. Secondly, to systematic effects due to non-idealities in the instrument design and performance, as listed in (Table 4.1). Sky maps made from individual detectors will thus be different from each other and a global map-making with the signal from several detectors taken together will result in the leakage of a spurious signal onto the global map. We formulate how such a non-ideality in the detectors or a mismatch in the observed signal projects onto the sky maps.

Let us consider a set of detectors $\{i\}$ observing the sky in a particular frequency band, with each of them observing a small variation $\delta\boldsymbol{d}^i$ with respect to the signal that should be observed under ideal circumstances. The data model for each detector will thus read,

$$\boldsymbol{d}^i = \boldsymbol{I} + \boldsymbol{Q}\cos\left(2\psi^i\right) + \boldsymbol{U}\sin\left(2\psi^i\right) + \delta\boldsymbol{d}^i(\psi^i) + \boldsymbol{n}^i \tag{4.12}$$

The source of the spurious signal is assumed to be very general and can be due to any number of reasons. We make the assumption that the variations across the detectors are not correlated and are independent of each other. Disregarding the contribution from the noise, it is the extra term $\delta\boldsymbol{d}^i$, unique to each detector, that is going to produce maps that are slightly different from each other and potentially produce a leakage when global maps are made.

In general the spurious signal will have contributions from the sky intensity as well as the polarisation signal. The intensity part will be independent of the polarisation angle. We may separate the spurious part as,

$$\delta\boldsymbol{d} = \delta\boldsymbol{d}_{Int} + \delta\boldsymbol{d}_{Pol}(\psi) \tag{4.13}$$

We look at what happens when we combine the measurement done by the set to make a single global map of the Stokes parameters. Let $\delta\boldsymbol{d}$ be the concatenated vector from all detectors and let $(\delta\widehat{\boldsymbol{I}}, \delta\widehat{\boldsymbol{Q}}, \delta\widehat{\boldsymbol{U}})$ be the leakage observed in the global sky maps. This map is made using the map-making equation (Equation 4.7) and the leakage map is given by

$$\begin{bmatrix}\delta\widehat{I}\\ \delta\widehat{Q}\\ \delta\widehat{U}\end{bmatrix}_p = [\mathrm{A}^T\mathrm{C}_\mathrm{n}^{-1}\mathrm{A}]_p^{-1}\frac{1}{\sigma^2}\begin{bmatrix}\sum\delta d\\ \sum\cos\left(2\psi\right)\delta d\\ \sum\sin\left(2\psi\right)\delta d\end{bmatrix} \tag{4.14}$$

Thus, the spurious term $\delta\boldsymbol{d}$ is projected onto the I, Q and U maps in a predictable way given by the map-making equation.

4.4 Modelling the Systematic Effects for Pairs

The primary approach by several CMB experiments to reconstruct the polarisation signal on the sky is to take the signal from a pair of orthogonally polarised detectors and differencing the signal from such a pair.

As we have described earlier, current CMB observations are made with polarisation sensitive detectors. Different detectors are arranged at a variety of angles on the focal plane in order to observe the same sky pixel with different angles. This can also be done for a single detector over the course of a year by employing a suitable scan strategy. This allows us to resolve the 3 Stokes parameter maps of I, Q and U. Let us consider the most general data model for one such detector (i)

$$\boldsymbol{d}^i = \boldsymbol{I}^i + \boldsymbol{Q}^i \cos\left(2\psi^i\right) + \boldsymbol{U}^i \sin\left(2\psi^i\right) + \boldsymbol{n}^i, \tag{4.15}$$

where notations follow the same convention as in section (4.2). We must note that due to non-idealities of the detectors, bandpass filters and other instrumental components, the Stokes signal (I,Q,U) will be offset from detector to detector. The polarisation angle too might be slightly offset from its preferred position. All of these will thus result in slightly different observed signals among a set of similar detectors and will manifest as a leakage onto the final sky map.

Future space missions such as CORE or LiteBIRD will have a focal plane populated by several detectors in the same frequency band with their polariser axis at different orientations. For example, the *Planck* focal plane had detectors with their polariser axis at $45°$ with each other. Future space mission with several tens of detectors in the same band can afford to have an even closer arrangement at $22.5°$. These detectors can either be single or dual polarisation sensitive. In the first case, the detector pairs along the scan direction will have their polariser axis rotated at right angles from each other, and in the second case with a pair of orthogonally polarised detectors in same focal plane pixel [87]. Taking the differenced signal of such a pair of detectors labelled (a) and (b), we get the following,

$$\begin{aligned}
\boldsymbol{d} &= \frac{1}{2}\left(\boldsymbol{d}^a - \boldsymbol{d}^b\right) \\
&= \frac{1}{2}\left[\left\{\boldsymbol{I}^a - \boldsymbol{I}^b\right\} + \left\{\boldsymbol{Q}^a \cos\left(2\psi^a\right) - \boldsymbol{Q}^b \cos\left(2\psi^b\right)\right\} + \left\{\boldsymbol{U}^a \sin\left(2\psi^a\right) - \boldsymbol{U}^b \sin\left(2\psi^b\right)\right\}\right] \\
&\quad + \frac{1}{2}\left(\boldsymbol{n}^a - \boldsymbol{n}^b\right)
\end{aligned} \tag{4.16}$$

Under the simplifying assumption that the noise is uncorrelated and independent between detectors, we can consider a simple white noise of stationary amplitude in each detector. It is not mandatory the level of white noise be the same in each detector but assuming it to be the same allows us to develop our formalism simply and clearly without noise-weighting different measurements. Assuming the random white noise, we formalise the statistics of the pair differenced noise $\boldsymbol{n} = \frac{1}{2}\left(\boldsymbol{n}^a - \boldsymbol{n}^b\right)$ as

$$\left\langle \boldsymbol{n}^a \right\rangle = \left\langle \boldsymbol{n}^b \right\rangle = 0 \tag{4.17a}$$

$$\left\langle \left(\boldsymbol{n}^a - \left\langle \boldsymbol{n}^a \right\rangle\right)^2 \right\rangle = \left\langle \left(\boldsymbol{n}^b - \left\langle \boldsymbol{n}^b \right\rangle\right)^2 \right\rangle = \sigma^2 \tag{4.17b}$$

$$\left\langle \boldsymbol{n} \right\rangle = 0 \tag{4.17c}$$

$$\left\langle \left(\boldsymbol{n} - \left\langle \boldsymbol{n} \right\rangle\right)^2 \right\rangle = \frac{1}{2}\sigma^2 \tag{4.17d}$$

4.4.1 Polarisation Misalignment

In the general situation shown in (Equation 4.16), the detector pairs are not perfectly oriented at right-angles to each other. The angle might be offset from $90°$ by a small value constituting a systematic effect itself. Considering that $\psi^a = \psi$ for the detector pair and $\delta\psi$ is the amount the angle is offset from $90°$, we can expand the cosine and sine terms in a Taylor series up to first-order to get

$$\begin{aligned} \cos\left(2\psi^b\right) &= \cos\left(2\psi + \pi + 2\delta\psi\right) \\ &= -\cos\left(2\psi\right) + 2\delta\psi \sin\left(2\psi\right) \end{aligned} \tag{4.18a}$$

$$\begin{aligned} \sin\left(2\psi^b\right) &= \sin\left(2\psi + \pi + 2\delta\psi\right) \\ &= -\sin\left(2\psi\right) - 2\delta\psi \cos\left(2\psi\right) \end{aligned} \tag{4.18b}$$

using this expansion, we can simplify our pair differenced model as

$$\begin{aligned} \boldsymbol{d} =& \frac{1}{2}\left[\left(\boldsymbol{I}^a - \boldsymbol{I}^b\right) + \left(\boldsymbol{Q}^a + \boldsymbol{Q}^b\right)\cos\left(2\psi\right) + \left(\boldsymbol{U}^a + \boldsymbol{U}^b\right)\sin\left(2\psi\right)\right] + \boldsymbol{n} \\ &+ \delta\psi\left[-\boldsymbol{Q}^b \sin\left(2\psi\right) + \boldsymbol{U}^b \cos\left(2\psi\right)\right] \end{aligned} \tag{4.19}$$

The first set of terms in the expression is what would have been observed if the detectors were perfectly aligned at right angles. The last set of terms is the correction required to obtain the actual signal observed by the pair. We note that the misalignment $\delta\psi$ expected is a small quantity and it couples only to the Stokes Q and U parameters. Hence the magnitude of the correction is going to be significantly smaller than the observed polarisation signal. This gives us the freedom to discard this term from our formulation of intensity to polarisation leakage and subsequent analysis. Nonetheless it will be interesting to estimate the level and nature of the leakage that is due to this particular effect. It is expected to give rise to a leakage of E-mode signal to B-modes.

It is also interesting to note the asymmetry in the correction term. Only the terms from the detector b appear. This, however, is trivial and depends upon our choice of selecting which detector to correct for the misalignment. If the correction to the angle was divided equally between the two detectors, the correction term would have contained the Stokes Q and U from both a and b.

4.4.2 First Order in Leakage Terms

The origin of the leakage can be understood by looking at the expression (Equation 4.19) without the detector misalignment correction term.

$$\boldsymbol{d} = \frac{1}{2}\left[\left(\boldsymbol{I}^a - \boldsymbol{I}^b\right) + \left(\boldsymbol{Q}^a + \boldsymbol{Q}^b\right)\cos(2\psi) + \left(\boldsymbol{U}^a + \boldsymbol{U}^b\right)\sin(2\psi)\right] + \boldsymbol{n} \tag{4.20}$$

We write down the Stokes terms in equation (Equation 4.20) to leading orders,

$$\boldsymbol{I}^a - \boldsymbol{I}^b = \Delta\boldsymbol{I}, \tag{4.21a}$$

$$\boldsymbol{Q}^a + \boldsymbol{Q}^b \approx 2\boldsymbol{Q}, \tag{4.21b}$$

$$\boldsymbol{U}^a + \boldsymbol{U}^b \approx 2\boldsymbol{U}, \tag{4.21c}$$

where $\boldsymbol{Q}$ and $\boldsymbol{U}$ are just the averaged values of the Stokes parameters seen by the detector pair. The Intensity signal is a few orders of magnitude greater than the Polarisation signal. Hence, the difference of the intensity is the term of interest as it is potentially of the same order as the polarisation terms and is hence kept. We are left with a reduced form of our data model with the leakage from the intensity term isolated. Our data model now reads

$$\boldsymbol{d} = \boldsymbol{Q}\cos(2\psi) + \boldsymbol{U}\sin(2\psi) + \frac{1}{2}\Delta\boldsymbol{I} + \boldsymbol{n}. \tag{4.22}$$

4.5 The Leakage as a Nuisance Term

Having isolated the intensity leakage term in our pair differenced data model, we are now ready to devise our modelling and correction strategy for the spurious signal.

Let us consider that the leakage term is due to several individual effects. We can expect that each individual leakage term can be modelled from some template derived from the intensity signal on the sky. We show this explicitly for the case of bandpass mismatch in (Chapter 6). This template $\boldsymbol{T}$ is projected onto the difference timestream $\boldsymbol{d}$ with a corresponding amplitude y. We may rewrite the data model as,

$$\boldsymbol{d} = \left[\boldsymbol{Q}\cos(2\psi) + \boldsymbol{U}\sin(2\psi)\right] + \sum_i y_i \boldsymbol{T}_i + \boldsymbol{n} \tag{4.23}$$

where the subscript i labels each of the leakage templates from different sources. This data model can be represented using vector-matrix notation as follows,

$$\boldsymbol{d} = \mathrm{A}\boldsymbol{S} + \mathrm{T}\boldsymbol{y} + \boldsymbol{n}, \tag{4.24}$$

where, A is now the reduced pointing matrix, whose non-zero element at each time sample t is given by

$$\mathrm{A}_{tp(t)} = \left[\cos(2\psi_t) \quad \sin(2\psi_t)\right], \tag{4.25}$$

$\boldsymbol{S}$ is the reduced set of pixel-ordered Stokes parameters, with the element at each pixel given by

$$\boldsymbol{S}_p = \begin{bmatrix} Q_p \\ U_p \end{bmatrix}. \tag{4.26}$$

T is the $\mathcal{N}_{\rm samp} \times \mathcal{N}_{\rm temp}$ sized set of all the leakage vectors given by

$$\mathrm{T} = \begin{bmatrix} \boldsymbol{T}_1 & \boldsymbol{T}_2 & \ldots & \boldsymbol{T}_{\mathcal{N}_{\rm temp}} \end{bmatrix}, \tag{4.27}$$

where each of the quantities $\boldsymbol{T}_i$ is itself a time-ordered vector of size $\mathcal{N}_{\rm samp}$. $\boldsymbol{y}$ is a $\mathcal{N}_{\rm temp}$ sized vector

$$\boldsymbol{y} = \begin{bmatrix} y_1 \\ y_2 \\ \vdots \\ y_{\mathcal{N}_{\rm temp}} \end{bmatrix}. \tag{4.28}$$

Our job is now to model the leakage templates in some way for each systematic effect and estimate their respective amplitudes.

4.6 Developing the Regression Algorithm

Our primary objective in the study of the systematic effects is to eventually remove the leakage from intensity to polarisation and have sky maps that are free from contamination. We demonstrate now the formulation of the algorithm to perform such a task. Looking at (Equation 4.24) we can consider the leakage term to be a pre-defined template T times the set of corresponding amplitudes $\boldsymbol{y}$. Our knowledge thus includes the observed pair-differenced signal $\boldsymbol{d}$, the projection matrix A and the set of leakage templates T. Using this we wish to find the unbiased estimator for the Stokes parameters $\widehat{\boldsymbol{S}}$.

4.6.1 The Estimators $\widehat{S}$ and $\widehat{y}$

We construct the generalised chi-square for our data model (Equation 4.24),

$$\chi^2 = [\boldsymbol{d} - \mathrm{A}\boldsymbol{S} - \mathrm{T}\boldsymbol{y}]^T \mathrm{C}_n^{-1} [\boldsymbol{d} - \mathrm{A}\boldsymbol{S} - \mathrm{T}\boldsymbol{y}] \tag{4.29}$$

In order to obtain our unbiased estimator $\widehat{\boldsymbol{S}}$ we employ an iterative technique. We first calculating the estimator for the set of amplitudes $\widehat{\boldsymbol{y}}$, substitute that in our χ^2 to then calculate our required estimator $\widehat{\boldsymbol{S}}$. Taking the derivative of the χ^2 with respect to $\boldsymbol{y}$ and setting it to zero gives us

$$\begin{aligned} &\nabla_{\boldsymbol{y}} \chi^2 = 0 \\ &\Rightarrow \widehat{\boldsymbol{y}} = [\mathrm{T}^T \mathrm{C}_n^{-1} \mathrm{T}]^{-1} \mathrm{T}^T \mathrm{C}_n^{-1} (\boldsymbol{d} - \mathrm{A}\boldsymbol{S}). \end{aligned} \tag{4.30}$$

Replacing the estimate of $\widehat{\boldsymbol{y}}$ in the chi-square yields

$$\chi^2 = \left[\left\{ \mathbb{1} - \mathrm{T} \left(\mathrm{T}^T \mathrm{C}_n^{-1} \mathrm{T} \right)^{-1} \mathrm{T}^T \mathrm{C}_n^{-1} \right\} (\boldsymbol{d} - \mathrm{A}\boldsymbol{S}) \right]^T \mathrm{C}_n^{-1} \left[\left\{ \mathbb{1} - \mathrm{T} \left(\mathrm{T}^T \mathrm{C}_n^{-1} \mathrm{T} \right)^{-1} \mathrm{T}^T \mathrm{C}_n^{-1} \right\} (\boldsymbol{d} - \mathrm{A}\boldsymbol{S}) \right]. \tag{4.31}$$

Let us now identify a couple of important terms from our new representation of the chi-square, which are

$$\mathrm{P_T} = \mathrm{T}\left(\mathrm{T}^T\mathrm{C}_n^{-1}\mathrm{T}\right)^{-1}\mathrm{T}^T\mathrm{C}_n^{-1}, \tag{4.32a}$$

$$\begin{aligned}\mathrm{F_T} &= \left\{\mathbb{1} - \mathrm{T}\left(\mathrm{T}^T\mathrm{C}_n^{-1}\mathrm{T}\right)^{-1}\mathrm{T}^T\mathrm{C}_n^{-1}\right\}\\ &= \{\mathbb{1} - \mathrm{P_T}\}.\end{aligned} \tag{4.32b}$$

These terms $\mathrm{P_T}$ and $\mathrm{F_T}$ and their properties will be studied in the following section. Making the substitutions of the terms into the chi-square and using the property that $\mathrm{F}_\mathrm{T}^T\mathrm{C}_\mathrm{n}^{-1}\mathrm{F_T} = \mathrm{C}_\mathrm{n}^{-1}\mathrm{F_T}$, we get

$$\chi^2 = [\boldsymbol{d} - \mathrm{A}\boldsymbol{S}]^T\,\mathrm{C}_n^{-1}\mathrm{F_T}\,[\boldsymbol{d} - \mathrm{A}\boldsymbol{S}] \tag{4.33}$$

Minimising this with respect to $\boldsymbol{S}$ will give us the estimator $\widehat{\boldsymbol{S}}$:

$$\begin{aligned}&\nabla_{\boldsymbol{S}}\chi^2 = 0\\ &\Rightarrow \widehat{\boldsymbol{S}} = \left[\mathrm{A}^T\mathrm{C}_n^{-1}\mathrm{F_T}\mathrm{A}\right]^{-1}\mathrm{A}^T\mathrm{C}_n^{-1}\mathrm{F_T}\boldsymbol{d}\end{aligned} \tag{4.34}$$

We perform a similar exercise to calculate $\widehat{\boldsymbol{y}}$. Minimising the chi-square in (Equation 4.29) with respect to $\boldsymbol{S}$ gives

$$\widehat{\boldsymbol{S}} = \left[\mathrm{A}^T\mathrm{C}_n^{-1}\mathrm{A}\right]^{-1}\mathrm{A}^T\mathrm{C}_n^{-1}(\boldsymbol{d} - \mathrm{T}\boldsymbol{y}) \tag{4.35}$$

Analogously to the previous case, we get the following terms:

$$\mathrm{P_A} = \mathrm{A}\left(\mathrm{A}^T\mathrm{C}_n^{-1}\mathrm{A}\right)\mathrm{A}^T\mathrm{C}_n^{-1}, \tag{4.36a}$$

$$\mathrm{F_A} = (\mathbb{1} - \mathrm{P_A}), \tag{4.36b}$$

and the estimator for the leakage amplitudes thus becomes

$$\widehat{\boldsymbol{y}} = \left[\mathrm{T}^T\mathrm{C}_n^{-1}\mathrm{F_A}\mathrm{T}\right]^{-1}\mathrm{T}^T\mathrm{C}_n^{-1}\mathrm{F_A}\boldsymbol{d}. \tag{4.37}$$

It is to be noted that the filtering approach that is developed here is similar to techniques that have been developed for destriping [88] and the filtering approach for POLARBEAR map-making [66].

4.6.2 Properties of the Estimators

Let us now analyse some properties of the estimators and terms defined in the previous section.

Space spanned by A and T

The operators and estimators derived in the previous section bring to light an important concept of map-making, that of spaces spanned by time-ordered vectors. Consider the map-making equation (Equation 4.10) and the data model (Equation 4.2). The estimate $\widehat{\boldsymbol{S}}$ is, by construction, the most likely value of the Stokes parameters on the sky. This means that $\mathrm{A}\widehat{\boldsymbol{S}}$ is the closest projection of the Stokes parameter on to the timestream. Writing this out

$$\mathrm{A}\widehat{\boldsymbol{S}} = \mathrm{A}\left(\mathrm{A}^T\mathrm{A}\right)^{-1}\mathrm{A}^T\boldsymbol{d} \tag{4.38}$$

we see that the operator $\mathrm{P}_\mathrm{A} = \mathrm{A}\left(\mathrm{A}^T\mathrm{A}\right)^{-1}\mathrm{A}^T$ we had defined earlier acts by projecting the most likely contribution of $\boldsymbol{S}$ in $\boldsymbol{d}$ onto the time-ordered space spanned by A. Using this analogy to vector spaces, we can define a space divided into sub-spaces spanned by the time-ordered vectors A and the set of templates $\{\boldsymbol{T}_i\}$. The exercise of finding the estimator $\widehat{\boldsymbol{S}}$ in (Equation 4.34) is therefore finding the projection of $\boldsymbol{d}$ on the sub-space of A by removing the contribution that project on to the sub-space spanned by the set $\{\boldsymbol{T}_i\}$.

Projection Operators P_A and P_T

The projection operators P_T and P_A as detailed in equations (Equation 4.32) and (Equation 4.36) are named such because they have the important property of projecting a variable onto the respective spaces spanned by T and A.

As is the general property of projection operators, the projection operators are idempotent,

$$\mathrm{P}_\mathrm{T}\mathrm{P}_\mathrm{T} = \left[\mathrm{T}\left(\mathrm{T}^T\mathrm{C}_\mathrm{n}^{-1}\mathrm{T}\right)^{-1}\mathrm{T}^T\mathrm{C}_\mathrm{n}^{-1}\right]\left[\mathrm{T}\left(\mathrm{T}^T\mathrm{C}_\mathrm{n}^{-1}\mathrm{T}\right)^{-1}\mathrm{T}^T\mathrm{C}_\mathrm{n}^{-1}\right] = \mathrm{P}_\mathrm{T} \tag{4.39a}$$

$$\mathrm{P}_\mathrm{A}\mathrm{P}_\mathrm{A} = \left[\mathrm{A}\left(\mathrm{A}^T\mathrm{C}_\mathrm{n}^{-1}\mathrm{A}\right)^{-1}\mathrm{A}^T\mathrm{C}_\mathrm{n}^{-1}\right]\left[\mathrm{A}\left(\mathrm{A}^T\mathrm{C}_\mathrm{n}^{-1}\mathrm{A}\right)^{-1}\mathrm{A}^T\mathrm{C}_\mathrm{n}^{-1}\right] = \mathrm{P}_\mathrm{A} \tag{4.39b}$$

The projection operators are symmetric under the condition that the noise is white and stationary.

$$\mathrm{P}_\mathrm{T}^T = \left[\mathrm{T}\left(\mathrm{T}^T\mathrm{T}\right)^{-1}\mathrm{T}^T\right]^T = \mathrm{P}_\mathrm{T} \tag{4.40a}$$

$$\mathrm{P}_\mathrm{A}^T = \left[\mathrm{A}\left(\mathrm{A}^T\mathrm{A}\right)^{-1}\mathrm{A}^T\right]^T = \mathrm{P}_\mathrm{A} \tag{4.40b}$$

The projection operator acting on $\boldsymbol{d}$ projects the components in the respective spaces of A or T.

$$\begin{aligned}\mathrm{P}_\mathrm{A}\boldsymbol{d} &= \left[\mathrm{A}\left(\mathrm{A}^T\mathrm{A}\right)^{-1}\mathrm{A}^T\right](\mathrm{A}\boldsymbol{S}+\mathrm{T}\boldsymbol{y}) \\ &= \mathrm{A}\boldsymbol{S} + \mathrm{P}_\mathrm{A}(\mathrm{T}\boldsymbol{y}), \end{aligned} \tag{4.41a}$$

$$\begin{aligned}\mathrm{P}_\mathrm{T}\boldsymbol{d} &= \left[\mathrm{T}\left(\mathrm{T}^T\mathrm{T}\right)^{-1}\mathrm{T}^T\right](\mathrm{A}\boldsymbol{S}+\mathrm{T}\boldsymbol{y}) \\ &= \mathrm{T}\boldsymbol{y} + \mathrm{P}_\mathrm{T}(\mathrm{A}\boldsymbol{S}). \end{aligned} \tag{4.41b}$$

If $\mathrm{T}\boldsymbol{y}$ contains no component in the space of A or conversely if $\mathrm{A}\boldsymbol{S}$ contains no component in the space of T, the last terms in (Equation 4.41) vanish.

Filtering Operators F_A and F_T

The operators F_A and F_T act on the time-ordered vector $\boldsymbol{d}$ and filter out the components in the respective spaces of A and T. Using the result from the projection operator (Equation

4.41), we get indeed

$$\begin{aligned}
\mathrm{F_A}\boldsymbol{d} &= \left\{\mathbb{1} - \mathrm{A}\left(\mathrm{A}^T\mathrm{A}\right)^{-1}\mathrm{A}^T\right\}(\mathrm{A}\boldsymbol{S} + \mathrm{T}\boldsymbol{y}) \\
&= \mathrm{A}\boldsymbol{S} + \mathrm{T}\boldsymbol{y} - \mathrm{A}\boldsymbol{S} - \mathrm{P_A}(\mathrm{T}\boldsymbol{y}) \\
&= \mathrm{T}\boldsymbol{y} - \mathrm{P_A}(\mathrm{T}\boldsymbol{y}), \qquad (4.42a)\\
\mathrm{F_T}\boldsymbol{d} &= \left\{\mathbb{1} - \mathrm{T}\left(\mathrm{T}^T\mathrm{T}\right)^{-1}\mathrm{T}^T\right\}(\mathrm{A}\boldsymbol{S} + \mathrm{T}\boldsymbol{y}) \\
&= \mathrm{A}\boldsymbol{S} + \mathrm{T}\boldsymbol{y} - \mathrm{A}\boldsymbol{S} - \mathrm{P_T}(\mathrm{A}\boldsymbol{S}) \\
&= \mathrm{A}\boldsymbol{S} - \mathrm{P_T}(\mathrm{A}\boldsymbol{S}). \qquad (4.42b)
\end{aligned}$$

4.6.3 Implementing the Algorithm

The estimator $\widehat{\boldsymbol{S}}$ is difficult to implement in the form of (Equation 4.34) computationally as the filtering operator $\mathrm{F_T}$ is of size $\mathcal{N}_{\mathrm{samp}} \times \mathcal{N}_{\mathrm{samp}}$ and is not sparse (but of low rank [66]). An alternative option is by an iterative method. This is the approach taken when correcting for systematic effects later on in the thesis.

We identify that the estimators (Equation 4.34) and (Equation 4.35) are identical with $\boldsymbol{y}$ replaced by $\widehat{\boldsymbol{y}}$ in the latter. In our iterative approach we first estimate the leakage amplitudes $\widehat{\boldsymbol{y}}$ (Equation 4.37) and using this we estimate the unbiased polarisation maps $\widehat{\boldsymbol{S}}$ (Equation 4.35). The estimator $\widehat{\boldsymbol{y}}$ can be further broken down by identifying that the projection operator $\mathrm{P_A}$ is in fact the map-making operator (Equation 4.7) followed by the re-projection of the map back into the space of A. The result of filtering the operands $\boldsymbol{d}$ and T is obtained by (Equation 4.42). Computationally, this is implemented by a sequence of map-making and re-observing the operands $\boldsymbol{d}$ and T. The covariance matrix $\left[\mathrm{T}^T\mathrm{F_A}\mathrm{T}\right]^{-1}$ is a dense square matrix of dimensions $\mathcal{N}_{\mathrm{temp}} \times \mathcal{N}_{\mathrm{temp}}$. For a small set of templates, this is computationally straightforward.

After estimating $\widehat{\boldsymbol{y}}$, it is a simple task of map-making (Equation 4.35) by subtracting out from the observed timestream vector $\boldsymbol{d}$ the leakage contribution from the templates $\mathrm{T}\boldsymbol{y}$. The end result is the set of maps of the Q and U Stokes parameters unbiased by the spurious leakage.

4.7 Summary and Discussion

The next generation of CMB polarisation space missions such as CORE and LiteBIRD will potentially be limited by systematic effects (4.1). If not accounted for these will lead to a leakage of signal from intensity to polarisation and bias the polarisation maps.

To correct for any intensity to polarisation leakage I have developed a regression method for a pair differencing CMB experiment. I formulated a general data model for a pair of orthogonally polarised detectors (4.4). The presence of systematic effects produce a mismatch between the detector signal and appears as a spurious term in the data model. The contribution from the intensity signal is the dominant term in the leakage. I modelled this spurious term as a nuisance which we wish to filter out (4.5) and produce unbiased maps of (Q,U). In order to filter out the leakage I constructed the maximum-likelihood estimator $\widehat{\boldsymbol{S}}$ (Equation 4.34) for the reduced set of Stokes parameters (4.6). This is implemented computationally by an iterative method (4.6.3). In essence, this algorithm fits a set of pre-defined templates T to the leakage signal. On estimating the leakage it is subtracted out of the timestream to produce unbiased polarisation maps.

The regression algorithm developed in this chapter is validated in the chapter (Chapter 6). It is then used to correct for the leakage of signal induced by the bandpass mismatch error. This algorithm is appropriate for any class of systematic effects that induce a signal mismatch between a pair of orthogonally polarised detector. Application of this technique requires a modelling of the leakage induced by the systematic effect and of the templates required to fit the spurious signal.

CHAPTER 5

THE SIMULATION CODE

Extensive simulation and analysis is required to test different aspects of a future CMB polarisation mission and assess its performance. To achieve the required science goals several stages of optimisation are required. For example, choosing an optimal scan strategy requires optimising the scan parameters by testing out each configuration with simulations of the time-ordered-data (TOD), and map-making. A future mission also requires a stringent control over systematic effects so that they do not contribute significantly to the noise budget. This requires accurate simulations of the major systematic effects, such as beam asymmetry and bandpass mismatch to assess their impact. New correction algorithms for correction of these effects need to be tested against the simulated data set and their performance evaluated. A future CMB mission employing an array of a few thousand detectors (CORE proposes 2100) will generate TODs of the order of PetaBytes over its full mission cycle. The volume of data poses an additional challenge and will require the use of optimised algorithms and data distribution models to perform large scale simulations and analysis tasks.

For the purpose of providing End-to-End simulation results, especially for the next generation of space mission like CORE and LiteBIRD, we have developed a simulation, map-making, and data analysis pipeline. The pipeline takes as input maps from the PSM in the *HEALPix* format, generates TODs and has the ability to emulate systematic effects such as beam asymmetry, bandpass mismatch, pointing errors and polarisation misalignment. Intensity and polarisation maps are reconstructed from the simulated timestream data using a maximum-likelihood mapmaker with an efficient data distribution model. Accompanying these core modules are a host of supporting library functions. The pipeline for simulation and correction of systematic effects is developed using these independent modules. We describe below some of the features of the new simulation pipeline that has been tailor made for the different simulation and analysis tasks for this thesis.

A git image of the simulation and analysis pipeline can be found at https://github.com/ranajoy-cosmo/core-plus.git

5.1 General Outline

The simulation package is coded primarily in the Python programming language in a modular fashion. OOP concepts have been used wherever necessary with the objective of modularity and re-usability. The Numpy, Healpy and Scipy packages are used extensively throughout much of the package.

The specifications for each simulation run, for example scan parameters, input maps to be used, beam shape, data paths, are provided through ‘config’ files and hence none of the simulation parameters is ‘hard-wired’ into the code. This feature together with the modularity allows the code to be very general and allows for fast development, testing of different scan strategies, building analysis pipelines, and testing of algorithms.

The important modules that have been developed are as follows.

- **Pointing module**
  The pointing library has the main class called ‘Pointing’, an instance of which can be used to generate time-ordered pointing data on the fly. The input parameters for the pointing class are the set of scan parameters developed in (3.2) and the initial position and orientation of the detector. The output products of the module are the position of the optical axis and detector polarisation direction at each time sample.

  The rotation operation is performed using a quaternion library, tailor made using optimised Numpy library functions as no suitable quaternion library was available during development. The use of quaternions has allowed for superior control over rotation of vectors as compared to Euler angles.

- **Beam module**
  This module contains the ‘Beam’ class whose instance generates a real-space pixelised beam map. It has options to either simulate beam maps given the parameters of the required beam, such as beam FWHM, ellipticity, orientation, offset, or it can load a predefined pixelised beam map generated from external sources.

- **Timestream simulation module**
  This is separated into two main modules, one containing the ‘Bolo’ class and the other performing the data distribution tasks. The ‘Bolo’ module performs the task of generating the timestream signal for each individual detector. It takes as input an external map in the *HEALPix* format, the pixelised beam map from the ‘Beam’ class and the pointing data from the ‘Pointing’ class. An useful feature is that the ‘Bolo’ class can be called from the mapmaking module and generate the time ordered data on the fly without requiring it to be stored to file.

- **Map-making module**
  This module performs the re projection of time ordered signal back on to the sky maps. The map-making module acts as a wrapper, mainly performing the data distribution tasks (detailed in the next section) and delegates the main functions of binning and generation of the covariance matrix to a separate module. This module has the functionality of generating T only, Polarisation only or (T,Q,U) maps.

5.2 Data Distribution Model

One of the most important and necessary features of any simulation and analysis pipeline for a future mission has to be its ability to handle large volumes of data efficiently. A future space mission such as CORE is expected to have a few thousand detectors, producing data of the order of PetaBytes over the course of its mission. The increasing volume of data can be handled on two fronts. Firstly, develop simulation and analysis techniques that are efficient in computation and memory usage. Secondly, exploit the massive parallelism that can be achieved with modern supercomputers.

Current supercomputers, such as ‘Edison’ at NERSC, have become limited by processor speed and hence the only way of scaling up any computation is through massive parallelism. Such system architectures offer two means of achieving parallelism, shared-memory or distributed-memory. Python is not suitable for the former and hence our simulation and analysis package has to rely completely on distributed-memory parallelism.

The process of simulating timestream data happens to be embarrassingly parallel, that is, there is no communication necessary between the individual parallel processes. The data streams are split up into equal chunks and generated independently of each other.

The process of map-making is however interesting and the need to generate large, high-resolution sky maps ($\mathrm{nside} = 4096$) prompted the development of a non trivial data distribution model. Our problem simplifies down considerably since we have considered throughout a diagonal pixel covariance matrix. The distribution of data in the map-making stage was achieved in two stages. Firstly, the chunked TODs were distributed among individual processes for re binning back onto the pixel space (Equation 4.9). The inverse covariance matrix was reconstructed from the chunked-up pointing data in a similar fashion, independently for each process. These arrays were chunked up pixel-wise and distributed among the processes. Due to the diagonal nature of the inverse covariance matrix, there are no cross terms between pixels, which allows us to invert the inverse covariance matrix per process individually. The map thus obtained per process is just a subset of the final map. The final map is obtained by concatenating the different map segments together. This procedure is illustrated in (Figure 5.1).

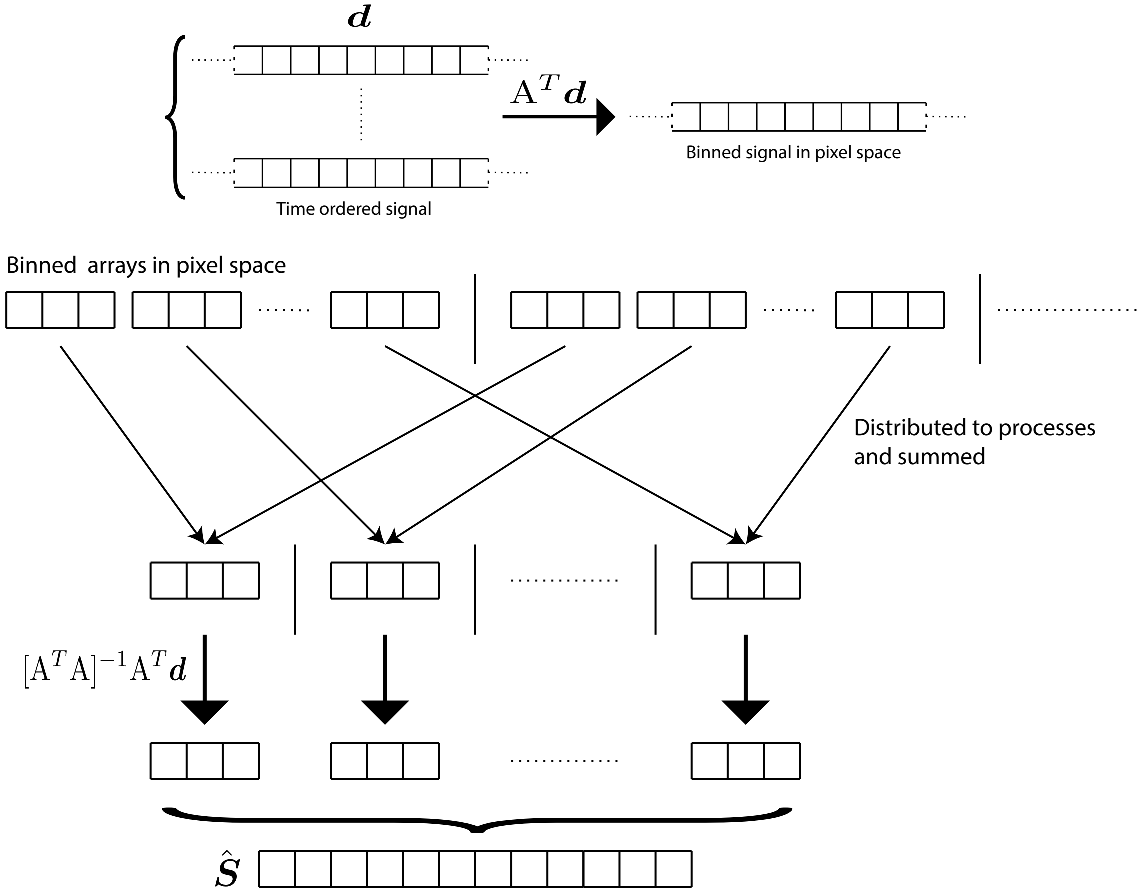

Figure 5.1: The data distribution model utilised in the map-making process. The time ordered signal chunks are binned onto the pixel space by de projection operator A^T. These pixel ordered arrays are then distributed to the individual processes and summed together. A similar procedure is applied to the inverse covariance matrix $[\mathrm{A}^T\mathrm{A}]$. The product of the covariance matrix with the distributes chunks give us segments of the final map. The final full sky map is obtained by concatenating the individual map chunks.

The implementation of the data distribution model described here allowed for very efficient use of memory and was crucial when working with large maps. For a $\mathrm{nside} = 4096$, the covariance matrix, in double precision, is $\approx 13.5\mathrm{GB}$. Inversion of each 3×3 element proved a bottleneck without implementing the second stage of distributing the chunked arrays.

5.3 Real Space Beam Convolution

An important and new feature implemented in the simulation code is that of fast real-space convolution of a *HEALPix* map with a real-space representation of the scanning beam. This allows us to simulate large volumes of realistic TODs for arbitrary beam shapes in a short time and has advantages over standard procedures used previously. We shall demonstrate these now.

The naïve procedure to simulate timestream signal is to scan the sky from a *HEALPix* map that has been pre-smoothed in the harmonic space by the beam-smoothing function (Equation 1.82). This has its limitations in that it smooths the sky for a symmetric Gaussian beam. Moreover, the sky pixelisation of the *HEALPix* maps adds artefacts such as sharp pixel edges to the timestream data. In real scans of the sky, the optical beam is never perfectly symmetric and Gaussian. Geometrical effects such as astigmatic aberration and the effect of the time constant cause the beams to be projected on the sky with a slight ellipticity. Additionally, there are inherent defects. With the motion of the instrument across the sky, the beam projects with changing orientations on the local sky coordinate system. Smoothing in harmonic space does not capture these features of a particular scan strategy. A real space convolution of the sky will capture these effects by mimicking exactly the movement and orientation of the beam on the sky.

The *Planck* mission employed a real space beam convolution method ‘FEBeCoP’ [89]. This algorithm generates an effective pixelised beam for each sky pixel and uses it to convolve the map in the real space. Other procedures such as ‘Quickbeam’ [90] provide an effective beam window function in the harmonic space. These algorithms act in the map space and do not generate any TOD that reflected the effect of the beam. Deconvolution map making techniques which generate maps from TOD with the knowledge of the beam in the harmonic space, such as [91] and [92], have also been developed.

The method developed here assumes an unsmoothed *HEALPix* sky at high resolution (ex: $nside = 4096$) and a pixelised map of the beam projected on to a Cartesian surface. At each sample point, the sky signal observed is the convolution of the *HEALPix* map with the optical beam. With discrete pixels, this amounts to a sum of the sky pixels weighted by the beam pixels. Consider a beam map divided into $\mathcal{N}_{\rm beam} \times \mathcal{N}_{\rm beam}$ pixels, where $\mathcal{N}_{\rm beam}$ is the number of beam pixels along a dimension. For each time sample, the number of computations required will scale as $\mathcal{N}^2_{\rm beam}$. Performing such a task is computationally cumbersome on the scale of the next generation CMB space missions. The real space convolution described here is implemented in a manner that reduces the number of computations.

An important feature that allows us to implement our real-space convolution algorithm is that the beam map projected on the sky remains fixed in the frame of the focal plane as illustrated in (5.2). Tracks traced out by different pixels on the beam will remain parallel to each other throughout the duration of the scan. This simplification allows us to easily perform our convolution in the focal plane reference frame. This also allows for a reduction in the complexity of the problem. Instead of the problem scaling as $\mathcal{N}_{\rm beam} \times \mathcal{N}_{\rm beam}$, it now scales as $\mathcal{N}_{\rm beam} \times \log(\mathcal{N}_{\rm beam})$.

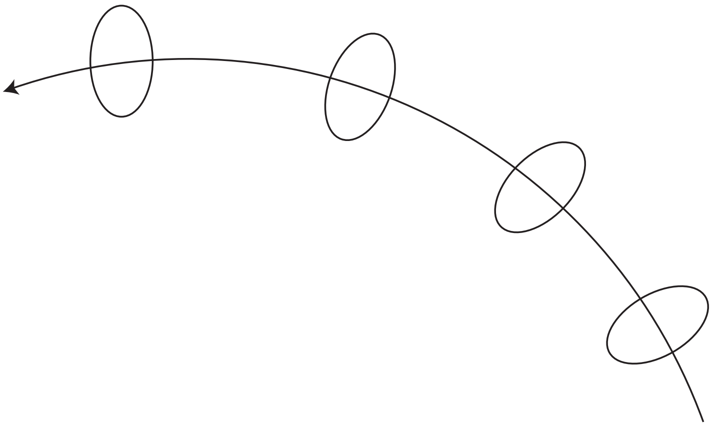

Figure 5.2: The figure illustrates how the projected beam on the sky remains fixed in the frame of the focal plane as the instrument scans along the sky.

The pixelised beam map, as illustrated in (5.3), is divided up into $\mathscr{N}_{\mathrm{beam}}$ individual rows, each along the direction of the scan. The beam map resolution is adjusted so as to correspond exactly to the co-scan resolution $\theta_{\parallel}$. Each beam pixel then correspond to contiguous time samples along the scan. To keep matters simple, the beam map pixels are of equal dimensions. The beam map is also normalised so that the sum of weights of all pixels is 1.

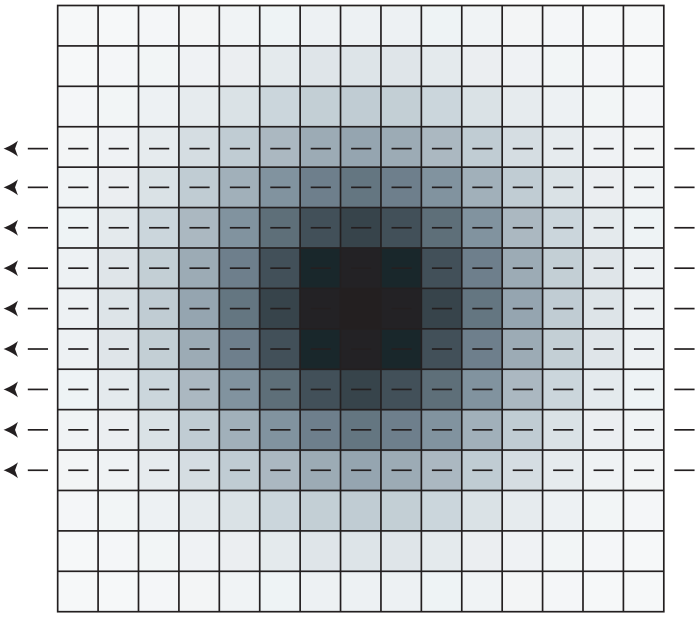

Figure 5.3: The strategy used for performing a real space beam convolution. The beam map is divided up into individual rows, each corresponding to an independent scan of the *HEALPix* sky map. The beam pixels are matched with the sampled points and each independent scan line is convolved in Fourier space by the corresponding beam row. The total signal due to the beam convolution is then just the sum of all the convolved scan lines.

Corresponding to each beam row an individual timestream is generated by scanning the sky. This is achieved by varying the opening angle β by $\theta_{\parallel}$ for each parallel scan row. This has a computational advantage in that the quaternions for the whole set need to be generated only once. The individual timestreams are then convolved in Fourier space by the corresponding beam rows and the total signal for each sample point is obtained by adding together all the $\mathscr{N}_{\mathrm{beam}}$ convolved timestreams.

Convolving two arrays with each other lead to edge effects due to the fact that the arrays have a finite length. This requires all the arrays for the time-ordered signal to have a padding of a certain length to avoid the edge effects. During testing of the convolution it was found that a padding of length $\mathscr{N}_{\mathrm{beam}}/2$ (rounded off the lower integer value) was sufficient to avoid edge effects.

The convolved timestream signal obtained by the above algorithm for a symmetric Gaussian beam is illustrated in (Figure 5.4). Notice that the signal obtained by the pencil beam contains artefacts due to the finite pixel size if $\theta_{\parallel}$ is smaller than the pixel size of the input map. The real space convolution avoids this problem as the extended beam map is sensitive to sub-pixel changes in its position and produces a smooth output signal. The size of the pixelised beam map was kept at $4\mathrm{FWHM}$ of the beam.

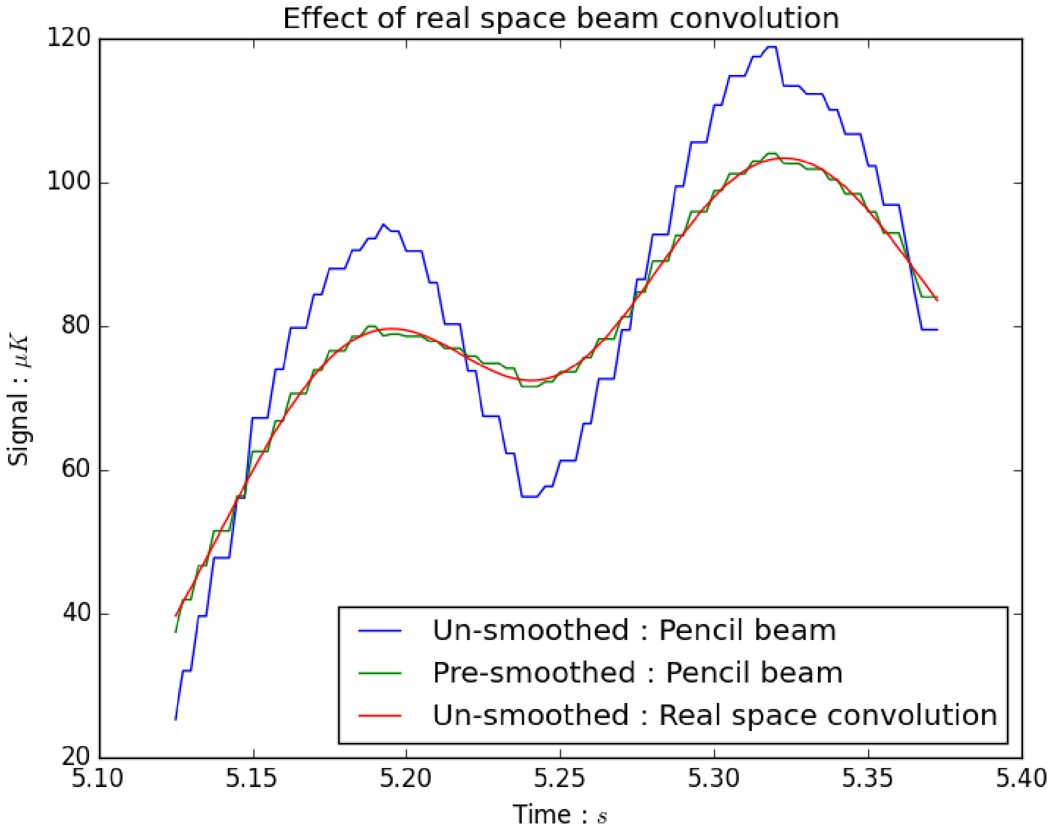

Figure 5.4: The real space convolved timestream is compared to that of a pencil beam scanning a sky map smoothed in harmonic space.

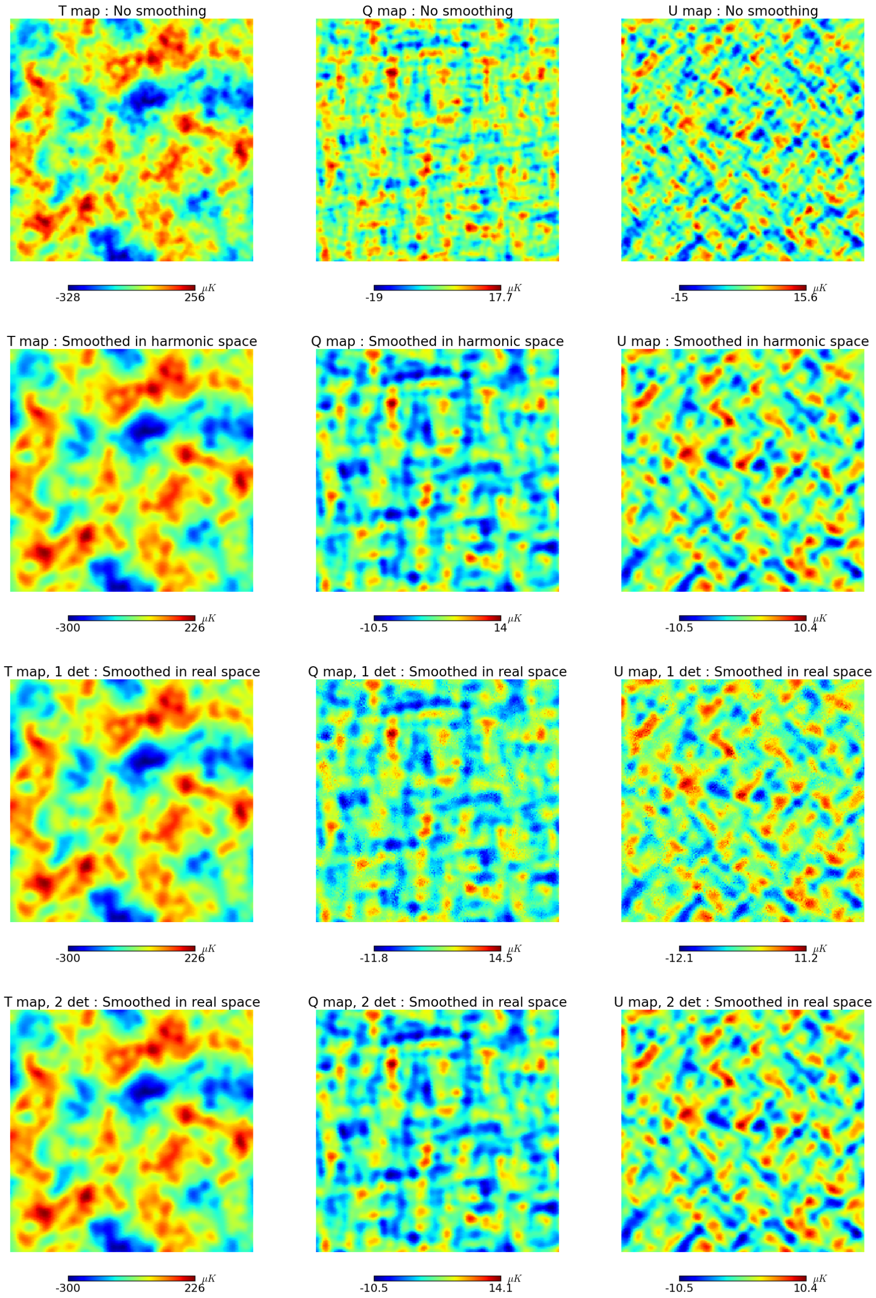

Figure 5.5: The figures compare the result of the real space beam convolution with a symmetric Gaussian beam of size $7.58'$ and a cutoff of 4 FWHM. The first row shows the unsmoothed map from which the timestream data was sampled from. The second row is that of a map smoothed in the harmonic space by an equivalent beam. The third row is the result of scanning the sky with a single detector. We see the presence of small scale artefacts. The final row is the result of scanning with a pair of orthogonally polarised detectors and shows the disappearance of the small scale artefacts.

(Figure 5.5) illustrates the resulting maps obtained by the real space beam convolution technique for an $7.58'$ symmetric Gaussian beam. The last two rows are done with the real space convolution technique using a single detector and a pair of detectors respectively. The simulations have been done for the scan configuration B in (Table 3.1). The input and output maps were both at $\mathrm{nside} = 4096$. The size of the pixelised beam map has been kept at 4 times the beam FWHM.

It is important to notice that in (Figure 5.5) for a single detector, there are visible small scale artefacts on the convolved map. As a result a residue with a white noise spectrum is induced (Figure 5.6). The induced noise starts dominating at $l \approx 1000$ over the lensing B modes and al $l \approx 100$ over the fiducial $r = 0.001$ signal.

To account for the spurious white noise induced on the map we investigated the effect of the Cartesian projection of the beam map. A spherical projection of the beam corresponding to the scan geometry was used to scan the same input map. The effect of the spherical projection was negligible and could not explain the spurious noise.

This spurious noise can be attributed to the fact that the pixel covariance matrix, as seen in (Figure 3.6) and (Figure 3.7) was not very well conditioned for a single detector and the noise variance was high in a large fraction of the detectors. The real space beam is also sensitive to sub-pixel effects and this difference is shown by the difference in the green and red line in (Figure 5.4). Scanning with a pencil beam does not capture the sub pixel effects. The high noise variance for the single detector can boost these small effects on the pixelised map. The induced white noise is considerably mitigated in the detector pair case and can be attributed to the better conditioning of the pixel covariance matrix. The remaining residual dominates over the lensing B modes at $l \approx 2500$ and over the fiducial $r = 0.001$ signal at $l \approx 350$. Further investigation is needed to completely characterise the source of this spurious signal and correct it.

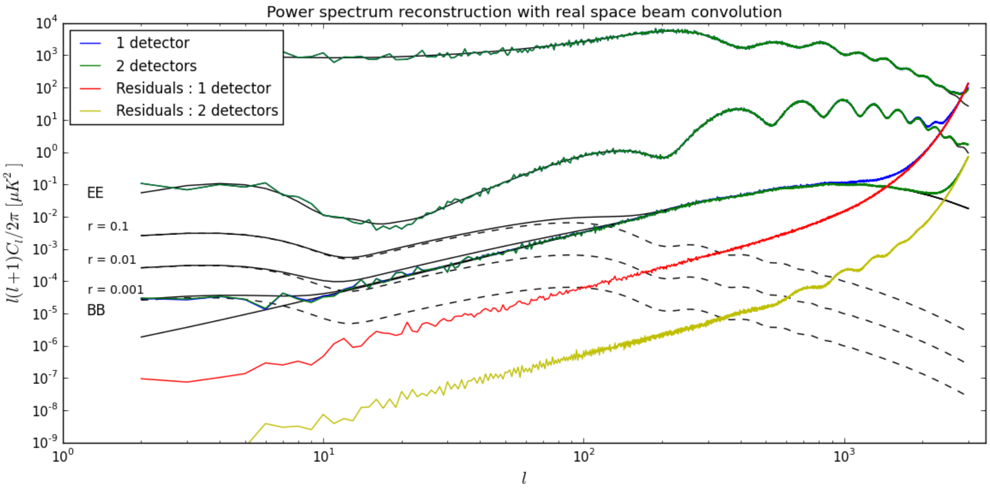

Figure 5.6: This figure shows the reconstructed spectra obtained from convolving the CMB sky in real space with a pixelised beam map. The green and blue curves overlap al low ells. However, the real space convolution introduces a white-noise like residual which is boosted by the beam ($7.58'$ here) at higher ells as shown by the 'Residual' curves.

5.4 Summary and Discussion

To optimise a next generation CMB space mission we need to perform large scale simulations to test out mission parameters and their impact on the mission requirements. To restrict the effect of systematics we need to develop accurate methods of simulating them and develop algorithms to mitigate their effects. This requires an efficient simulation and analysis tool that exploits the available optimised code base and the architecture of available computational systems. I have developed a simulation and analysis pipeline for such a purpose (5.1).

I have developed a real space beam convolution method that generates realistic TODs that reflect the motion and orientation of a pixelised beam map as it scans the sky (5.3). This has practical advantages over previous codes that performed convolutions at the map level. It allows us to analyse, characterise and mitigate for systematic effects at the timestream level. Such a tool is capable of generating other sources of systematics such as pointing mismatch, by shifting the beam origin, and can be coupled with effects such as bandpass mismatch. I used this tool to simulate the impact of elliptic beams in (Chapter 7). Using this I also developed an iterative deconvolution map making technique.

CHAPTER 6

BANDPASS MISMATCH

Cosmic Microwave Background experiments typically observe the microwave sky in several frequency channels, each channel having several detectors. Ideally, all detectors in a particular channel are expected to have the same spectral response function. The signal from the ensemble of such detectors is then used to produce single frequency maps. In practice, the response of each individual detector in a frequency band is not guaranteed to be identical to the others. In such a case of bandpass mismatch this leads to a leakage of signal from intensity to polarisation that can be severe enough to mask out the faint primordial B mode signal. Previous missions such as WMAP [93] and *Planck* [75][72] have encountered the issue of bandpass mismatch, and required sophisticated analysis methods to correct for its effect. For a future space mission, aimed at detecting the signature of Inflation through B-modes, it is necessary to estimate to impact of this effect, model it and find ways of mitigating it.

In this chapter we estimate the impact and characteristics of bandpass mismatch error for the case of CORE and LiteBIRD. We validate the systematics correction map-making technique we developed in (Chapter 4) and implement it on our simulated datasets.

6.1 Modelling the Signal

Polarisation sensitive detectors used for CMB and foreground observation scan the sky in particular microwave frequency bands determined by filters which are characterised by the spectral response function $h(\nu)$. The specific intensity (brightness) on the sky is thus integrated by the spectral response function to give us the total signal in the detector. Taking into account this band-integration explicitly, we can rewrite the data model (Equation 4.1) in the following form,

$$\boldsymbol{d} = \int d\nu\, h(\nu)\left[\boldsymbol{I}(\nu) + \boldsymbol{Q}(\nu)\cos\left(2\psi\right) + \boldsymbol{U}(\nu)\sin\left(2\psi\right)\right] + n, \tag{6.1}$$

where $[\boldsymbol{I}(\nu), \boldsymbol{Q}(\nu), \boldsymbol{U}(\nu)]$ are the Stokes parameters on the sky at the frequency ν. We have dropped the explicit time and the pixel indices t and $\hat{\mathrm{p}}(t)$.

The total sky brightness arises from the superposition of emission from different astrophysical processes. Apart from the CMB there is thermal dust and the CO line emission which are the main contributors above $100\,\mathrm{GHz}$, and the galactic synchrotron, anomalous dust and free-free which are the main contributors at lower frequencies. The total sky brightness at a given point can be written as a sum of all the components

$$\boldsymbol{I}(\nu) = \sum_{\mathrm{c}} f_{\mathrm{c}}(\nu, \nu_0)\boldsymbol{I}_{\mathrm{c}}(\nu_0), \tag{6.2}$$

where $\boldsymbol{I}_{\mathrm{c}}(\nu_0)$ is the amplitude of component c, at some reference frequency ν_0. $\boldsymbol{I}_{\mathrm{c}}(\nu_0)$ is scaled by the function $f_{\mathrm{c}}(\nu,\nu_0)$ to the appropriate frequency ν. The function $f_{\mathrm{c}}(\nu,\nu_0)$ contains the information of the spectral emission law for each component c. For example, to first order, thermal dust has the spectrum of a modified black-body with a spectral index, so that the scaling factor is given by

$$\begin{aligned} f_{\mathrm{TD}}(\nu,\nu_0) &= \frac{\boldsymbol{I}_{\mathrm{TD}}(\nu)}{\boldsymbol{I}_{\mathrm{TD}}(\nu_0)}, \\ &= \left(\frac{\nu}{\nu_0}\right)^{\beta(\hat{\mathrm{p}})} \frac{B(\nu, T_{\mathrm{TD}})}{B(\nu_0, T_{\mathrm{TD}})}, \end{aligned} \tag{6.3}$$

where T_{TD} is the effective temperature of the thermal dust, $B(\nu, T_{\mathrm{TD}})$ is the Planck emission law at temperature T_{TD} and $\beta(\hat{\mathrm{p}})$ is the spectral index of the emission at position $\hat{\mathrm{p}}$ on the sky.

We can construct relations similar to (Equation 6.2) for the Stokes $\boldsymbol{Q}(\nu)$ and $\boldsymbol{U}(\nu)$ parameters, and for the sake of simplicity we assume that the scaling law $f_{\mathrm{c}}(\nu,\nu_0)$ is identical for all the three Stokes parameters. Using this we can write down our data model (Equation 6.1) for any detector as

$$\boldsymbol{d} = \sum_{\mathrm{c}} \int \mathrm{d}\nu\, h(\nu) f_{\mathrm{c}}(\nu,\nu_0) \left[\boldsymbol{I}_{\mathrm{c}} + \boldsymbol{Q}_{\mathrm{c}} \cos(2\psi) + \boldsymbol{U}_{\mathrm{c}} \sin(2\psi)\right], \tag{6.4}$$

where $(\boldsymbol{I}_{\mathrm{c}}, \boldsymbol{Q}_{\mathrm{c}}, \boldsymbol{U}_{\mathrm{c}})$ are the Stokes parameters for each component c at the reference frequency ν_0. We may define a new parameter

$$\alpha_{\mathrm{c}} = \int d\nu\, h(\nu) f_{\mathrm{c}}(\nu,\nu_0). \tag{6.5}$$

Let us call this the bandpass parameter. This parameter contains all information regarding the bandwidth and spectral response of the detector, and the spectral emission law of the component c. The spectral emission law of any component c on the sky being the same for all detectors, it is only the spectral response function $h(\nu)$ that causes any change in the parameter α_{c}. As is standard in CMB observation, we consider that the signal is calibrated on the CMB dipole for the individual detectors. We can thus rescale the corresponding α_{CMB} for the CMB component to 1 and for all the rest of the components we will have $\alpha \neq 1$. Hereafter, we shall use only the rescaled bandpass parameter. As an example, as shown in [68], the bandpass parameter for thermal dust emission is given by,

$$\alpha_{\mathrm{TD}} = \left(\frac{\int \mathrm{d}\nu\, h(\nu) \left(\frac{\nu}{\nu_0}\right)^{\beta(\hat{\mathrm{p}})} \frac{B(\nu;T_{\mathrm{TD}})}{B(\nu_0;T_{\mathrm{TD}})}}{\int \mathrm{d}\nu\, h(\nu) \left(\frac{\partial B(\nu;T)}{\partial T}\right)\Big|_{T_0}} \right) \left(\frac{\partial B(\nu_0;T)}{\partial T}\right)\Big|_{T_0}, \tag{6.6}$$

where, T_0 is the mean CMB temperature of $2.73\mathrm{K}$, and all other variables and parameters are as defined before.

6.2 Multi-Detector Maps and Projection of the Leakage

We consider a set of detectors each with its individual bandpass parameter α_{c}^{i}. We define the following statistics on the set of parameters $\{\alpha_{\mathrm{c}}^{i}\}$ for each component c

$$\langle\alpha_{\mathrm{c}}\rangle = \bar{\alpha}_{\mathrm{c}}, \tag{6.7a}$$

$$\left\langle(\alpha_{\mathrm{c}} - \langle\alpha_{\mathrm{c}}\rangle)^2\right\rangle = \sigma_c^2. \tag{6.7b}$$

For each detector i we define the parameter $\delta\alpha_{\mathrm{c}}^{i} = \alpha_{\mathrm{c}}^{i} - \bar{\alpha}_{\mathrm{c}}$ which is the difference of the bandpass parameter α_{c}^{i} from the mean of the set. The statistics of this parameter is given by

$$\langle\delta\alpha_{\mathrm{c}}\rangle = 0, \tag{6.8a}$$

$$\left\langle(\delta\alpha_{\mathrm{c}} - \langle\delta\alpha_{\mathrm{c}}\rangle)^2\right\rangle = \sigma_{\mathrm{c}}^2. \tag{6.8b}$$

Using this definition, we can rewrite the data model (Equation 6.4) for a detector i as

$$\begin{aligned}\boldsymbol{d}^i &= \sum_{\mathrm{c}}\left(\bar{\alpha}_{\mathrm{c}} + \delta\alpha_{\mathrm{c}}^{i}\right)\left[\boldsymbol{I}_{\mathrm{c}} + \boldsymbol{Q}_{\mathrm{c}}\cos\left(2\psi^i\right) + \boldsymbol{U}_{\mathrm{c}}\sin\left(2\psi^i\right)\right],\\ &= \left[\boldsymbol{I} + \boldsymbol{Q}\cos\left(2\psi^i\right) + \boldsymbol{U}\left(2\psi^i\right)\right] + \sum_{\mathrm{c}}\delta\alpha_{\mathrm{c}}^{i}\left[\boldsymbol{I}_{\mathrm{c}} + \boldsymbol{Q}_{\mathrm{c}}\cos\left(2\psi^i\right) + \boldsymbol{U}_{\mathrm{c}}\sin\left(2\psi^i\right)\right].\end{aligned} \tag{6.9}$$

The terms in the first set of square brackets in (Equation 6.9) give the total anisotropy signal that would be seen for the average bandpass parameter $\bar{\alpha}$, and also if there was no bandpass mismatch between the detectors. The remaining terms are the spurious terms, specific to each detector.

Analogously to section (4.3) and along the lines of the treatment in [68], we demonstrate how the terms in the second set of brackets in (Equation 6.9) lead to a leakage onto the global maps for multiple detectors. We note that the intensity signal is a few orders of magnitude greater than the polarisation signal, so we keep the dominating intensity term in the spurious signal expression. We consider the concatenated vector of the spurious term from the complete detector set,

$$\delta\boldsymbol{d} = \left(\sum_{\mathrm{c}}\delta\alpha_{\mathrm{c}}^{i}\boldsymbol{I}_{\mathrm{c}}\right). \tag{6.10}$$

We consider that the sky has been observed with enough variation of polarisation angles with the complete detector set so that the covariance matrix approaches the ideal case (Equation 4.11). The projection of the spurious signal from each component c onto the maps is given by

$$\begin{bmatrix}\delta\widehat{I}_{\mathrm{c}}\\ \delta\widehat{Q}_{\mathrm{c}}\\ \delta\widehat{U}_{\mathrm{c}}\end{bmatrix}_p = \frac{1}{N_{\mathrm{hits}}}\begin{bmatrix}1 & 0 & 0\\ 0 & 2 & 0\\ 0 & 0 & 2\end{bmatrix}\begin{bmatrix}\sum\limits_i\sum\delta\alpha_{\mathrm{c}}^{i}I_{\mathrm{c}}\\ \sum\limits_i\sum\cos\left(2\psi^i\right)\delta\alpha_{\mathrm{c}}^{i}I_{\mathrm{c}}\\ \sum\limits_i\sum\sin\left(2\psi^i\right)\delta\alpha_{\mathrm{c}}^{i}I_{\mathrm{c}}\end{bmatrix} \tag{6.11}$$

where the second summation is over all data points corresponding to sky pixel p. Since I_{c} is a function of the pixel alone and $\delta\alpha_{\mathrm{c}}^{i}$ a function of the detector i, these can be taken out of their respective sums. Dropping the index p the leakage maps due to all the different foreground components are

$$\delta\widehat{I} = \frac{1}{N_{\mathrm{hits}}}\sum_{\mathrm{c}} I_{\mathrm{c}} \sum_{i} \delta\alpha_{\mathrm{c}}^{i} n_{\mathrm{hits}}^{i}, \tag{6.12a}$$

$$\delta\widehat{Q} = \frac{2}{N_{\mathrm{hits}}}\sum_{\mathrm{c}} I_{\mathrm{c}} \sum_{i} \delta\alpha_{\mathrm{c}}^{i} n_{\mathrm{hits}}^{i} \left\langle \cos\left(2\psi^{i}\right)\right\rangle, \tag{6.12b}$$

$$\delta\widehat{U} = \frac{2}{N_{\mathrm{hits}}}\sum_{\mathrm{c}} I_{\mathrm{c}} \sum_{i} \delta\alpha_{\mathrm{c}}^{i} n_{\mathrm{hits}}^{i} \left\langle \sin\left(2\psi^{i}\right)\right\rangle, \tag{6.12c}$$

where N_{hits} is the hit-count in the pixel p due to the complete detector set and n_{hits}^{i} is the hit-count due to just the detector i. The $< \cdots >$ represents an average over all data points in a particular pixel.

For a configuration of orthogonally polarised detector pairs labelled ia and ib, the cross-linking maps are related as

$$\left\langle \cos\left(2\psi^{i}\right)\right\rangle = \left\langle \cos\left(2\psi^{ia}\right)\right\rangle = -\left\langle \cos\left(2\psi^{ib}\right)\right\rangle, \tag{6.13a}$$

$$\left\langle \sin\left(2\psi^{i}\right)\right\rangle = \left\langle \sin\left(2\psi^{ia}\right)\right\rangle = -\left\langle \sin\left(2\psi^{ib}\right)\right\rangle. \tag{6.13b}$$

Using this relation and assuming that the detectors in a pair have identical hit-counts for every pixel, we can rewrite the leakage projection expressions (Equation 6.12) for Q and U as

$$\delta\widehat{Q} = \frac{2}{N_{\mathrm{hits}}}\sum_{\mathrm{c}} I_{\mathrm{c}} \sum_{i\in\{ia\}} \Delta\alpha_{\mathrm{c}}^{i} n_{\mathrm{hits}}^{i} \left\langle \cos\left(2\psi^{i}\right)\right\rangle, \tag{6.14a}$$

$$\delta\widehat{U} = \frac{2}{N_{\mathrm{hits}}}\sum_{\mathrm{c}} I_{\mathrm{c}} \sum_{i\in\{ia\}} \Delta\alpha_{\mathrm{c}}^{i} n_{\mathrm{hits}}^{i} \left\langle \sin\left(2\psi^{i}\right)\right\rangle, \tag{6.14b}$$

where the summation is now over only half of the detector set $\{ia\}$, that is, only detector a in each pair ia and ib. We have defined a new term $\Delta\alpha_{\mathrm{c}}^{i}$ and call it the bandpass mismatch parameter. It is defined as

$$\Delta\alpha_{\mathrm{c}}^{i} = \delta\alpha_{\mathrm{c}}^{ia} - \delta\alpha_{\mathrm{c}}^{ib} = \alpha_{\mathrm{c}}^{ia} - \alpha_{\mathrm{c}}^{ib}. \tag{6.15}$$

It is the difference of the bandpass parameters pair-by-pair. The variance of this parameter is given by,

$$\left\langle (\Delta\alpha_{\mathrm{c}} - \langle\Delta\alpha_{\mathrm{c}}\rangle)^{2}\right\rangle = 2\sigma^{2}. \tag{6.16}$$

The individual detector pairs have independent pointing and orientation of the polarisation axis on the sky. This amounts to each pair having an independent hitcount and cross-linking map. However, since the detectors will be closely packed in the focal plane, they are expected to have similar hitcounts across the sky. We make the simplifying assumption that the hitcount map of all detectors is the same. Using this assumption we may write the total hitcount for the entire detector set as

$$N_{\mathrm{hits}} = 2N_{\mathrm{pairs}}\, n_{\mathrm{hits}}, \tag{6.17}$$

where N_{pairs} is the number of detector pairs in the set. This gives us the expression for the leakage projection maps as

$$\delta\widehat{Q} = \frac{1}{N_{\text{pairs}}} \sum_{\text{c}} I_{\text{c}} \sum_{i\in\{ia\}} \Delta\alpha_{\text{c}}^{i} \left\langle \cos\left(2\psi^{i}\right)\right\rangle, \tag{6.18a}$$

$$\delta\widehat{U} = \frac{1}{N_{\text{pairs}}} \sum_{\text{c}} I_{\text{c}} \sum_{i\in\{ia\}} \Delta\alpha_{\text{c}}^{i} \left\langle \sin\left(2\psi^{i}\right)\right\rangle. \tag{6.18b}$$

This relation shows that, for each individual detector pair, the amplitude of the projected leakage from each component c is directly proportional to the bandpass mismatch parameter $\Delta\alpha_{\text{c}}$, and is projected onto the Q and U maps by the cross-linking maps $\langle\cos(2\psi^{i})\rangle$ and $\langle\sin(2\psi^{i})\rangle$ respectively. In units of power, the leakage spectra per pair and per component will thus be proportional to the square of $\Delta\alpha_{\text{c}}$.

Usually, CMB experiments employ detector pairs in multiple orientations. For example, as shown in (Table 6.1), the detectors are oriented at $0°$, $90°$, $45°$ and $135°$, with the ones at right angles forming the pair. The cross-linking maps for pairs with similar orientation will be similar. The parameter $\Delta\alpha_{\text{c}}$ being a random variate, the leakage projection due to the superposition of several detector pairs of the same orientation will scale inversely as a function of $\sqrt{N_{\text{pairs}}}$. In units of power, the leakage spectra will thus scale inversely as N_{pairs}. The leakage projection maps from pairs with different orientations do not superpose. Moreover, detectors are spread over the focal plane and similarly oriented detector pairs produce cross-linking maps that are slightly offset from each other. This makes the scaling law non-trivial and dependent upon the relative orientation and position of the detector pairs on the focal plane.

(Equation 6.18) also demonstrates the impact of the scan strategy on the bandpass mismatch contamination. The cross-linking maps are the cross terms in the covariance matrix (Equation 4.8). A good scan strategy will have these cross terms as close as possible to 0 and sharply peaked about it. The choice of a scan strategy to reduce bandpass mismatch leakage can thus be made from the histograms of the covariance matrix cross terms for a single detector as shown in (3.6).

To simulate the variation in the filter properties, we generate sky maps integrated by a top hat band profile and a variation in the edges of the bands. The spectral response function $h(\nu)$ is 1 within the band and 0 everywhere outside. As a conservative estimate, we vary the band edges by 1% over the central frequency $\nu_0 = 145\text{GHz}$.

$$\sigma\left[\frac{\nu_{\text{min}}}{\nu_0}\right] = \sigma\left[\frac{\nu_{\text{max}}}{\nu_0}\right] = 0.01. \tag{6.19}$$

The mean bandwidth is taken to be 25% of ν_0. The 16 bands are sampled from a Gaussian distribution with the given properties and are listed in (Table 6.1).

Pair	Detector	Pol angle	Position	ν_{min}	ν_{max}	ν_{mid}	α_{TD}	$\Delta\alpha_{\text{TD}}$
		Degrees	Arc-minutes	GHz	GHz	GHz		
1	$1a$	0	9.875	127.20	163.54	145.37	1.0087	0.0435
	$1b$	90	9.875	125.81	160.13	142.97	0.9652	
2	$2a$	45	9.875	127.05	161.71	144.38	0.9905	-0.0127
	$2b$	135	9.875	126.94	163.20	145.07	1.0032	
3	$3a$	0	19.75	124.85	162.16	143.50	0.9750	-0.0158
	$3b$	90	19.75	124.15	164.57	144.36	0.9908	
4	$4a$	45	19.75	124.67	161.93	143.30	0.9714	-0.0413
	$4b$	135	19.75	128.12	163.06	145.59	1.0126	
5	$5a$	0	29.625	126.32	164.08	145.20	1.0058	0.0069
	$5b$	90	29.625	128.19	161.51	144.85	0.9989	
6	$6a$	45	29.625	127.35	162.09	144.72	0.9967	-0.0032
	$6b$	135	29.625	128.97	160.85	144.91	0.9998	
7	$7a$	0	39.5	125.14	160.90	143.02	0.9662	-0.0195
	$7b$	90	39.5	126.10	162.12	144.11	0.9857	
8	$8a$	45	39.5	127.20	166.90	147.05	1.0404	0.0532
	$8b$	135	39.5	127.63	160.79	144.21	0.9872	

Table 6.1: The table shows the 16 detector used in our simulations, their position on the focal plane and their band properties. This represents a portion of the 145GHz channel for CORE [56]. A positive value of position means it is further away from the spin axis. The bandpass parameter α has been calculated using the lower and upper bounds, for a top-hat band profile, for thermal dust emission using the formula (Equation 6.6) with $\nu_0 = 145\,\text{GHz}$.

(Figure 6.1) illustrates the conclusion drawn out in equation (Equation 6.18) by comparing the ratio of the leakage Q map and reference map I_c to the corresponding cross-linking map $\langle\cos(2\psi)\rangle$. The two corresponding maps are similar but not identical. The small differences are not completely accounted for and need further investigation to fully characterise them. The simulation is done in galactic coordinates with input maps containing CMB and thermal dust only, and hence the leakage is due solely to the thermal dust signal. The reference thermal dust map is made at $145\,\text{GHz}$. The pair labelled 1 in (Table 6.1) with the specified top-hat bands is used. The scanning strategy employed is that of Configuration A and B in (Table 3.1). The leakage maps are constructed by taking the difference of the maps made for the pair with the average maps of the two detectors individually.

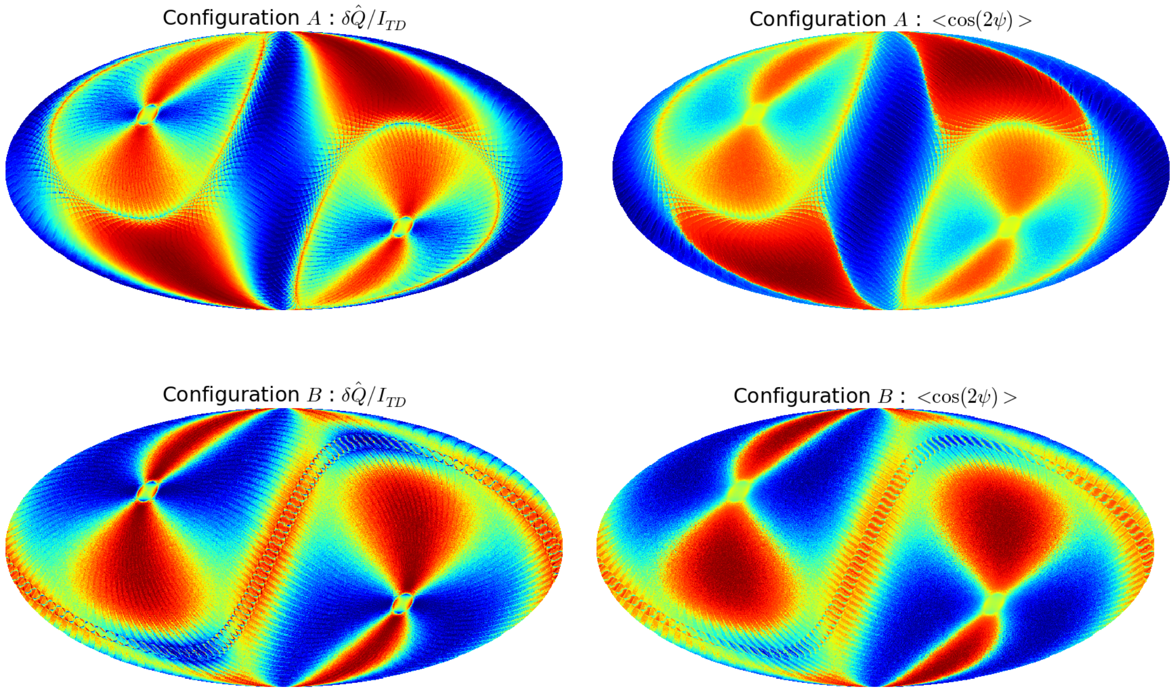

Configuration A : $\delta\hat{Q}/I_{TD}$

Configuration A : $<\cos(2\psi)>$

Configuration B : $\delta\hat{Q}/I_{TD}$

Configuration B : $<\cos(2\psi)>$

Figure 6.1: The figure compares the maps for $\frac{\delta\widehat{Q}}{I_{\mathrm{TD}}}$ to $\langle\cos(2\psi)\rangle$. The Two configurations A and B in table 3.1 are used for the pair labelled 1 in table 6.1.

(Equation 6.18) showed that amplitude of the leakage maps are directly proportional to the bandpass mismatch parameter $\Delta\alpha$. The leakage spectra should therefore be quadratic in $\Delta\alpha$. To demonstrate this, we plot the power spectra of the leakage generated for the different pairs given in (Table 6.1) in (Figure 6.2). The configuration used is A.

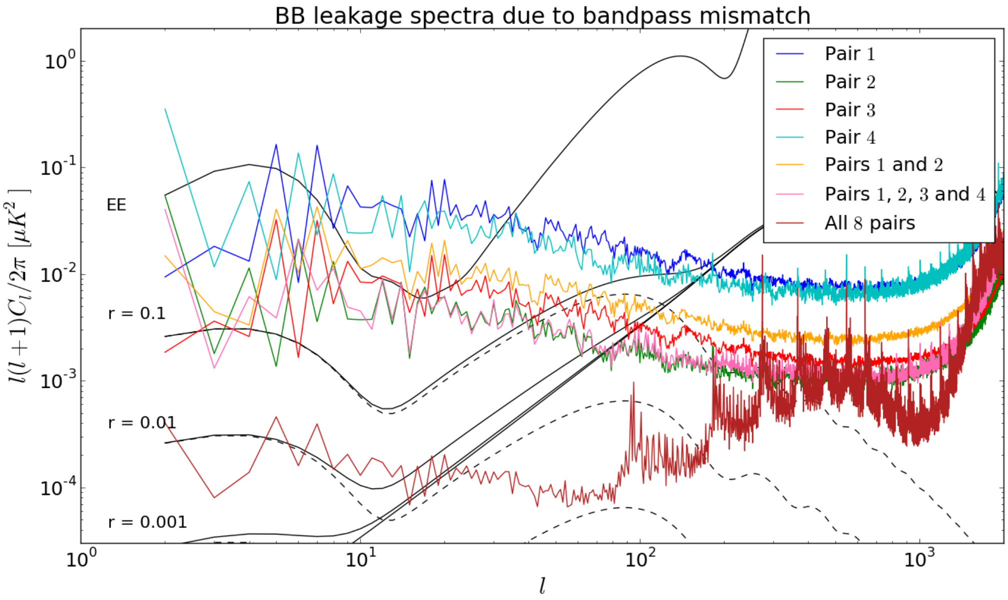

Figure 6.2: As can be seen from the spectra in (Figure 6.2), the leakage spectra of different pairs with similar polariser orientation have the same shape (compare pair 1 with 3 and pair 2 with 4) because they project in the same way. The leakage scales quadratically with the bandpass mismatch parameter $\Delta\alpha$. The leakage due to combination of pairs does not project in a simple manner since the different shapes of the projection maps do not superpose. The superposition of leakage maps due to all 16 detectors gives rise to artefacts that show up as peaks and its harmonics on the power spectrum and a distinct bump above $l \approx 100$.

The leakage projection maps in (Equation 6.18) transform by simple trigonometric relations in the following manner under a rotation of the instrument polariser,

$$\delta\widehat{Q} \xrightarrow{\psi+\frac{\pi}{4}} -\delta\widehat{U} \tag{6.20a}$$

$$\delta\widehat{U} \xrightarrow{\psi+\frac{\pi}{4}} \delta\widehat{Q} \tag{6.20b}$$

A simple substitution of the transformation (Equation 6.20) in (Equation 1.69) and in (Equation 1.70) shows that the coefficients $a_{E,lm}$ and $a_{B,lm}$ transform as,

$$a_{E,lm} \xrightarrow{\psi+\frac{\pi}{4}} a_{B,lm} \tag{6.21a}$$

$$a_{B,lm} \xrightarrow{\psi+\frac{\pi}{4}} -a_{A,lm} \tag{6.21b}$$

This has the effect of switching the EE and BB leakage spectra with each other as illustrated in (Figure 6.3). It shows the leakage spectra for the pairs 1 and 2 in (Table 6.1) which are at an angle of $45\,°$ with each other. The bandpass mismatch parameter $\Delta\alpha$ being different for the pairs, the amplitude of the leakage is correspondingly different. Using the configuration E we demonstrate an interesting feature of the leakage spectra, that of the conspicuous peaks. The location of the peaks show a strong relation to the scales at which the resonance patterns appear on the polarisation sensitivity map (Figure 3.8).

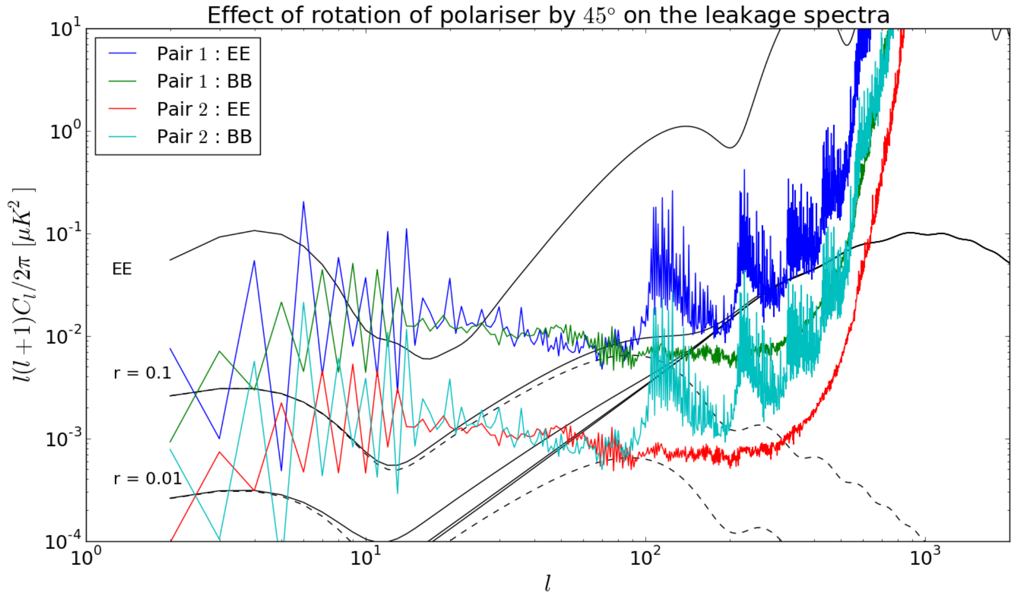

Figure 6.3: The rotation of the instrument polariser flips the EE and BB spectra with each other. The bandpass mismatch parameter $\Delta\alpha$ for the pairs 1 and 2 used in this plot are 0.04353 and -0.01271, hence the differing amplitude between the two pairs. The scan strategy used is Configuration E. The peaks seen in the figure correspond to the resonance patterns seen in (Figure 3.8).

Since we have shown that the magnitude of the leakage due to bandpass is directly proportional to the cross terms in the pixel covariance matrix, the effectiveness of a particular scan strategy in minimising bandpass mismatch errors can be gauged by comparing the leakage spectra from different scan strategies. For this purpose we compare the bandpass leakage spectra for all the five configurations in (Table 3.1) for the case of a single pair of detectors and for the case of the full set of 16 detectors.

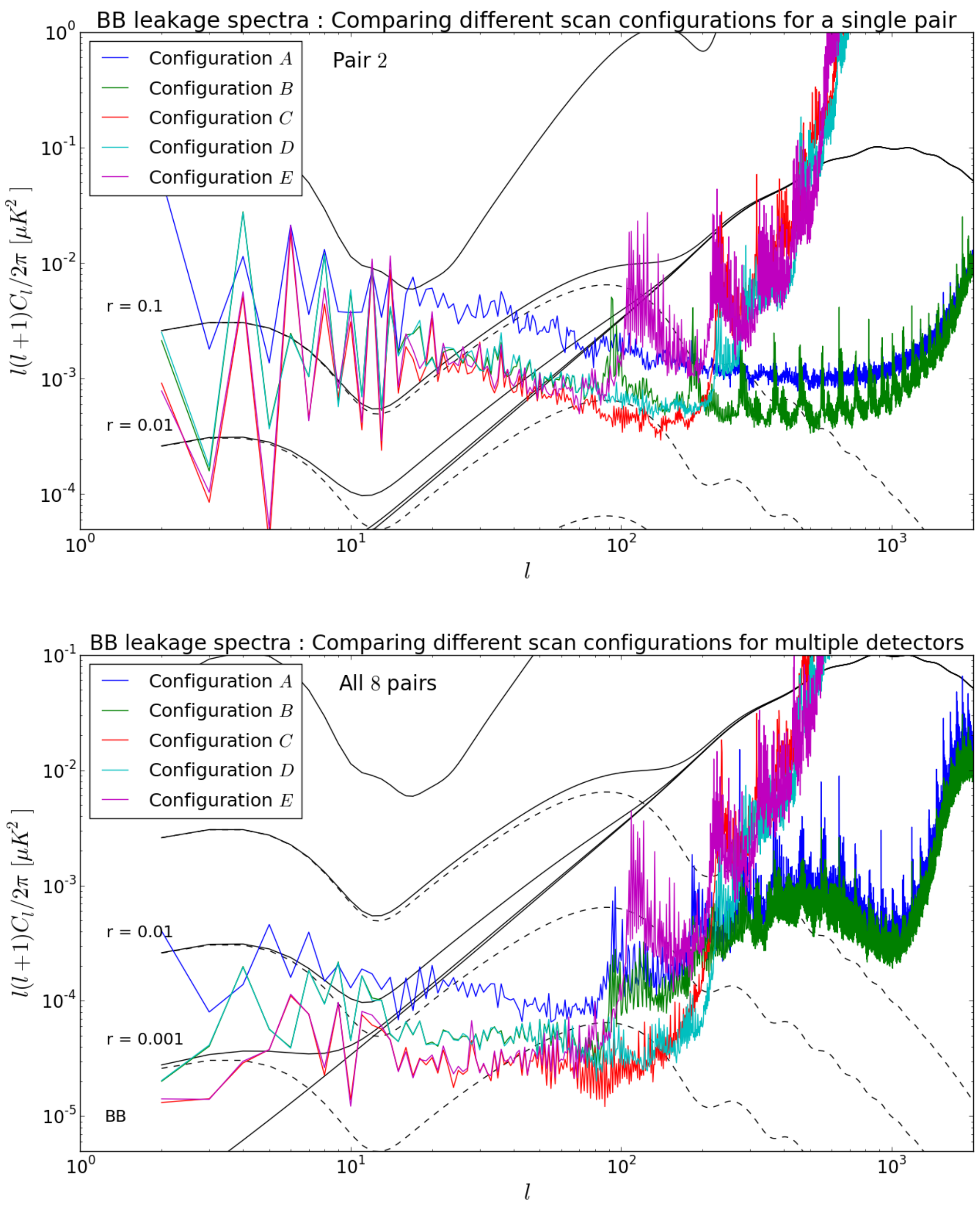

Figure 6.4: *Top*: The BB leakage spectra from all 5 scan strategies is plotted for the case of Pair 2. We note that the leakage for the configurations C, D and E is boosted at $l > 100$ because they were performed using a $30'$ beam and the leakage spectra had to be de-beamed for the same amount. *Bottom*: Similar to the top panel, the leakage spectra has been calculated for the full set of 16 detectors. The configurations A and B show a distinctive bump at $l > 100$ which is believed to be due to the effect of stacking leakage maps that are slightly offset from each other.

The spikes in (Figure 6.4) can be attributed to the resonance patterns seen in (Figure 3.8) for configuration E. Other configurations also show prominent spikes, such as B, but they are not as prominent as for E.

In (Figure 6.4) at low multipoles $l < 100$, where the signal is not dominated by the resonance spikes, the effect of the scan strategy is evident. The configuration A has the worst performance among the set. This can be attributed to the poor cross-linking leading to the large spread in the off-diagonal terms of the covariance matrix (3.6). Configurations C and E are the best owing to their superior angular coverage in each pixel. Configurations B and D are intermediate between the two cases. In general, strategies which have $\alpha > \beta$ as described in (3.3) are less affected by bandpass leakage.

6.3 Single-Detector Map-Making

The issue of bandpass mismatch leakage can be bypassed completely if we consider making single detector maps. The spurious signal in (Equation 6.9) gets projected on to the polarisation maps on a pair-by-pair basis. Single detector maps are immune to this as there is no intensity to polarisation leakage due to a mismatch with another detector. It however has the adverse effect of boosting the noise as shown in (Figure 6.5).

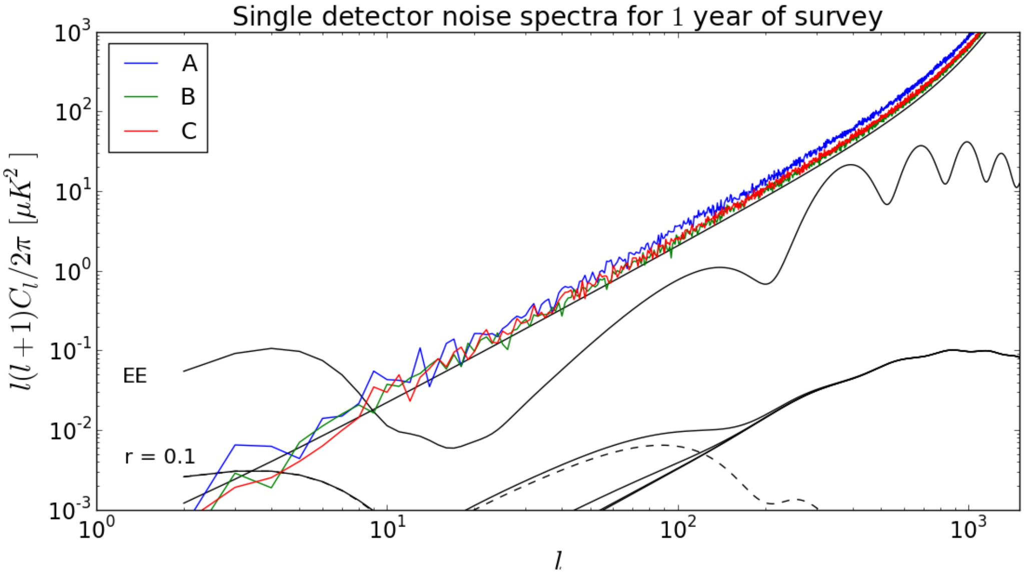

Figure 6.5: Single detector noise spectra for a scan duration of 1 year for the three configurations A, B and C. An ideal and uniform scan would have projected the noise on the theoretical line (solid black). The noise for the different configurations are however more than the theoretical value. This demonstrates the boosting of the noise spectra as a result of inadequate angular variation. The figures (Figure 3.6) and (Figure 3.7) show the boosted noise variance over a large fraction of the sky. As expected, the configuration A fares the worst among the three scan strategies plotted here

The increased noise is attributed to the large fraction of the sky being sampled poorly. The corresponding pixel covariance matrices demonstrate this in section (3.6).

6.4 Correction Model for Detector Pairs

To set up the leakage model for correction let us now consider a pair of detectors, ia and ib, which have their polarisation direction orthogonal to each other. The pair have a slightly mismatched band integration parameter between the two detectors leading to a leakage of a spurious signal (Equation 6.9) on to the polarisation Q and U maps (Equation 6.14). Let us write down the data model for the pair similar to (Equation 6.9),

$$\boldsymbol{d}^{ia} = \sum_{\mathrm{c}} \left(\bar{\alpha}_{\mathrm{c}} + \delta\alpha_{\mathrm{c}}^{ia}\right)\left[\boldsymbol{I}_{\mathrm{c}} + \boldsymbol{Q}_{\mathrm{c}}\cos\left(2\psi^i\right) + \boldsymbol{U}_{\mathrm{c}}\sin\left(2\psi^i\right)\right] + \boldsymbol{n}^{ia}, \tag{6.22a}$$

$$\boldsymbol{d}^{ib} = \sum_{\mathrm{c}} \left(\bar{\alpha}_{\mathrm{c}} + \delta\alpha_{\mathrm{c}}^{ib}\right)\left[\boldsymbol{I}_{\mathrm{c}} + \boldsymbol{Q}_{\mathrm{c}}\cos\left(2\psi^i + \pi\right) + \boldsymbol{U}_{\mathrm{c}}\sin\left(2\psi^i + \pi\right)\right] + \boldsymbol{n}^{ib}. \tag{6.22b}$$

To isolate the leakage term due to the bandpass mismatch we take the differenced signal of the pair to get

$$\begin{aligned}
\boldsymbol{d}^{i} &= \frac{1}{2}\left(\boldsymbol{d}^{ia} - \boldsymbol{d}^{ib}\right), \\
&= \sum_{\mathrm{c}} \bar{\alpha}_{\mathrm{c}}\left[\boldsymbol{Q}_{\mathrm{c}}\cos\left(2\psi^i\right) + \boldsymbol{U}_{\mathrm{c}}\sin\left(2\psi^i\right)\right] + \boldsymbol{n}^{i} \\
&\quad + \frac{1}{2}\sum_{\mathrm{c}}\left[\left(\delta\alpha_{\mathrm{c}}^{ia} - \delta\alpha_{\mathrm{c}}^{ib}\right)\boldsymbol{I}_{\mathrm{c}} + \left(\delta\alpha_{\mathrm{c}}^{ia} + \delta\alpha_{\mathrm{c}}^{ib}\right)\boldsymbol{Q}_{\mathrm{c}}\cos\left(2\psi^i\right) + \left(\delta\alpha_{\mathrm{c}}^{ia} + \delta\alpha_{\mathrm{c}}^{ib}\right)\boldsymbol{U}_{\mathrm{c}}\sin\left(2\psi^i\right)\right],
\end{aligned} \tag{6.23}$$

where the term in the first square brackets is the unbiased signal for the detector pair and $\boldsymbol{n}^i$ is as defined in (Equation 4.17). The remaining terms are the leakage terms.

Unlike for the complete set of detectors where the bandpass parameter α_{c} was distributed randomly about the mean of the set, for the detector pair, we can make a few simplifications. It is easy to see that for each individual pair of detectors, the $\delta\alpha_{\mathrm{c}}$ terms are related as

$$\delta\alpha_{\mathrm{c}}^{ia} = -\delta\alpha_{\mathrm{c}}^{ib} = \frac{1}{2}\left(\alpha_{\mathrm{c}}^{ia} - \alpha_{\mathrm{c}}^{ib}\right), \tag{6.24a}$$

$$\left(\delta\alpha_{\mathrm{c}}^{ia} - \delta\alpha_{\mathrm{c}}^{ib}\right) = \left(\alpha_{\mathrm{c}}^{ia} - \alpha_{\mathrm{c}}^{ib}\right), \tag{6.24b}$$

$$\left(\delta\alpha_{\mathrm{c}}^{ia} + \delta\alpha_{\mathrm{c}}^{ib}\right) = 0. \tag{6.24c}$$

These relations show us that when we consider each pair of detector alone, the spurious signal is purely due to the intensity signal on the sky and it has no contribution from the polarisation terms. We must be careful here in making the distinction between the situation of a pair of detectors and the complete set of detectors. The relations in (Equation 6.24) will not hold in the case of the full set of detectors.

Coming back to the pair differenced signal (Equation 6.23), we can rephrase the data model as the contribution due to the unbiased average signal of the pair plus the spurious leakage term. The relation (Equation 6.15) still holds for a pair of detectors and hence we may write,

$$\boldsymbol{d}^{i} = \left[\boldsymbol{Q}\cos\left(2\psi^i\right) + \boldsymbol{U}\sin\left(2\psi^i\right)\right] + \frac{1}{2}\sum_{\mathrm{c}\neq\mathrm{CMB}} \Delta\alpha_{\mathrm{c}}^{i}\boldsymbol{I}_{\mathrm{c}} + \boldsymbol{n}^{i} \tag{6.25}$$

$$= \mathrm{A}\boldsymbol{S} + \mathrm{T}\boldsymbol{y} + \boldsymbol{n} \tag{6.26}$$

This now resembles the data model we had worked out in the chapter 4 where the contribution is due to the sky signal plus the spurious term we wish to remove from the timestream.

6.5 Validation of the Correction Algorithm

In the previous section we have worked out the data model for bandpass leakage for the case of a pair of orthogonally oriented polarisation sensitive detectors. We showed that, to leading orders in leakage term, it is identical to the leakage data model we had worked out in chapter 4. We shall now use the case of bandpass leakage and construct a toy model to serve as a sanity test and validate our correction algorithm.

Let us consider a toy model where we have a pair of polarisation sensitive detectors, which are orthogonal in their polarisation directions, labelled a and b. These two detectors have slightly offset band edges and centres and have slightly different bandpass parameters α_{c}. This will thus lead to a projection of the spurious term onto the Q and U maps (Equation 6.14).

For our simulation we constructed two sets of sky maps, using the PSM tool [94], with a top hat spectral band of width 25% of the central frequency. The central frequencies of the maps were $145.37\,\mathrm{GHz}$ and $142.97\,\mathrm{GHz}$. The maps included just two components, CMB and thermal dust. The scanning strategy used is the baseline strategy for the CORE proposal (Configuration A). We demonstrate two situations. First, with no noise in the simulated timestreams to demonstrate the correction algorithm at its theoretical limit. Second, with a stationary white noise of amplitude $39.9\,\mu K\sqrt{s}$ for each detector.

We note that we are artificially constructing the template by having prior knowledge of how the leakage is projecting. This is done in order to validate our correction algorithm. In practice we will not have this information.

We construct an ideal template which we claim projects exactly like the spurious term onto the Q and U maps and thus can be used to completely cancel out the spurious term. This is motivated by (Equation 6.23) where the leakage term is proportional to $(\alpha_{\mathrm{c}}^{a}\boldsymbol{I}_{\mathrm{c}}^{a} - \alpha_{\mathrm{c}}^{b}\boldsymbol{I}_{\mathrm{c}}^{b})$. This is just the difference of the intensity signal observed by the two detectors. For the no noise case, we expect the estimated amplitude $\widehat{y}$ of the template to be exactly 0.5. The noisy case will demonstrate how the noise affects the estimation of y.

The leakage projection maps for the Q and U Stokes parameters are obtained by subtracting from the reconstructed global maps of the pair of detectors, the average of the individual input Q and U maps. This can be appreciated by observing in equation (Equation 6.25) that the band integration parameter of the unbiased Q and U maps will be the simple mean of the pair, and hence the expected unbiased maps will just be the simple mean of the two input maps.

The perfect template that we constructed is projected onto the Q and U map space by the P_{A} projection operator as shown in (4.6.2) and should match exactly the leakage pattern.

The estimated amplitudes of the templates for the noiseless and the noisy case are 0.5 and 0.501 respectively. This is what was predicted. On comparing the leakage maps for Q and U to the projected template we find them to be identical up to floating point precision for the noiseless case. Performing the complete leakage correction routine we are left with residues on the Q and U map consistent with the floating point precision of the machine.

For the noisy case, the noise in the timestream adds a statistical uncertainty to the estimate of y, hence the estimated leakage patterns do not cancel out completely the leakage.

This simple sanity test demonstrates the validity of the correction algorithm and shows that it functions as expected. This exercise tests out the properties of the operators defined in 4.

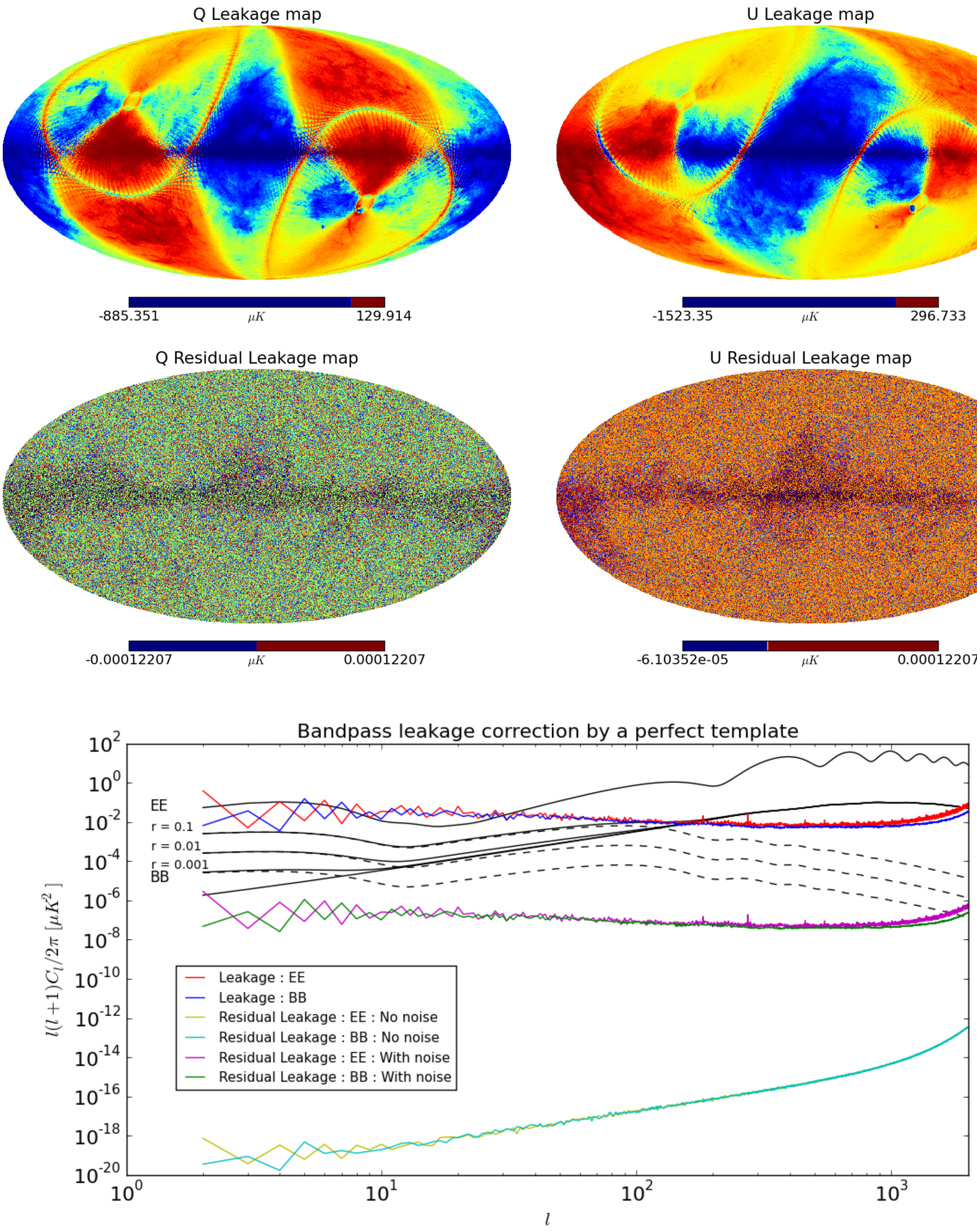

Figure 6.6: *Top row*: The figures illustrated the projection of the leakage on to the Q and U maps. *Middle row*: The residual leakage after correction in the no noise case. As expected, the leakage has been corrected up to machine precision for the majority of the pixels. *Bottom row*: The power spectra of the leakage map is compared with the residual leakage maps for the noisy and noiseless case.

6.6 Correction for Multiple Detectors

In section (6.2), we have shown that the leakage generated due to the bandpass mismatch error is significant enough to severely contaminate any primordial B-mode signal that might be present. For detector pairs, the leakage was directly proportional to the bandpass mismatch parameter $\Delta\alpha$ and for certain pairs strong enough to mask all E-mode and lensed B-mode signal at low multipoles. The effect is expected to scale with the number of detectors but due to the projection of leakage with different shapes, the final leakage map is shown to produce artefacts on the power spectrum. After having demonstrated the validity and effectiveness of the correction algorithm in the previous section, we now perform the exercise of correcting for the bandpass leakage for the set of 16 detectors that we have been working with.

We perform the leakage correction exercise for Configuration A, which is the CORE baseline strategy. The leakage spectra are shown for a combination of different detectors in (Figure 6.2). As a first test we include only Thermal Dust and CMB in our input maps with the same band profiles as defined in (Table 6.1). The template for the Thermal Dust emission is generated at $350\mathrm{GHz}$ using the PSM tool and with a 25% bandwidth.

Since the power spectra have been estimated on 75% of the sky after masking the galactic plane using the mask (Figure 6.7), it is not necessary to include the data points corresponding to the masked pixels in our estimation of the parameter $\widehat{y}_{\mathrm{TD}}$. Data points corresponding to such pixels are therefore masked out.

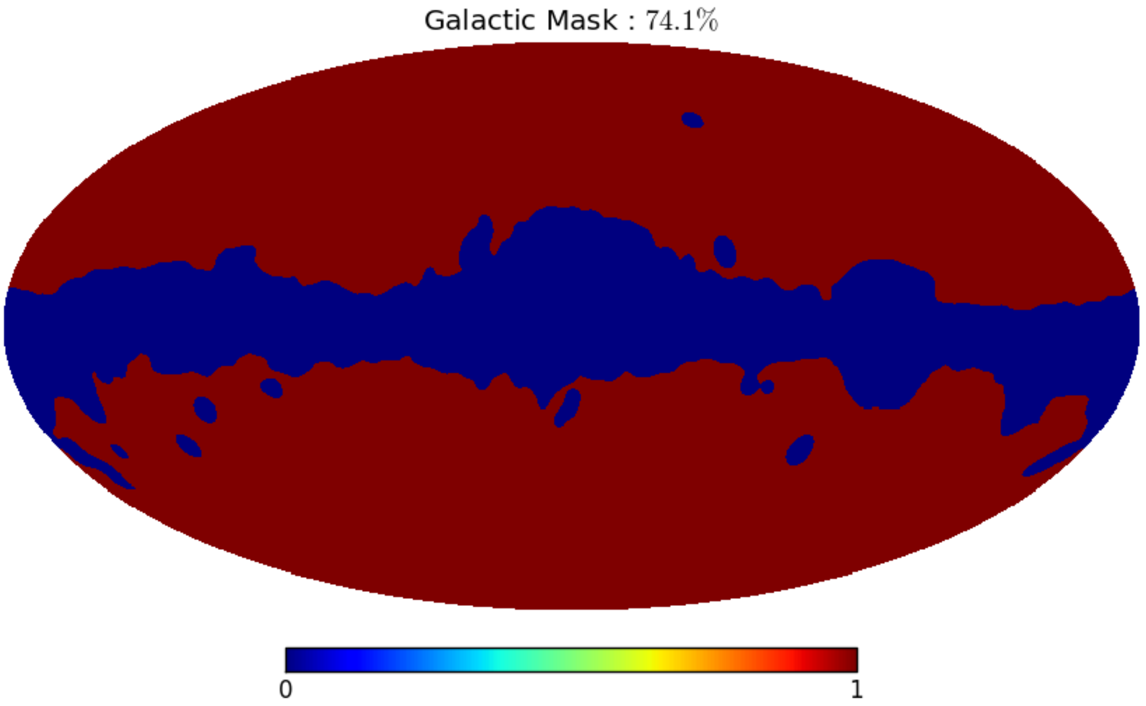

Figure 6.7: The 74.1% galactic mask used for estimating the power spectra for the bandpass mismatch error.

To determine the effect noise has on the estimation of the template amplitude, we perform our correction twice, once without any timestream noise and once with an added white noise of amplitude $39.9\mu\mathrm{K}\sqrt{\mathrm{s}}$. The estimated values of the template amplitude are tabulated for both cases in tables (Table 6.2) and (Table 6.3) respectively. The results of the correction plotted in (Figure 6.8) are for the noisy case. Map-making being a linear operation, the noise projection on the map is simply subtracted out in order to expose the leakage and the residual leakage maps.

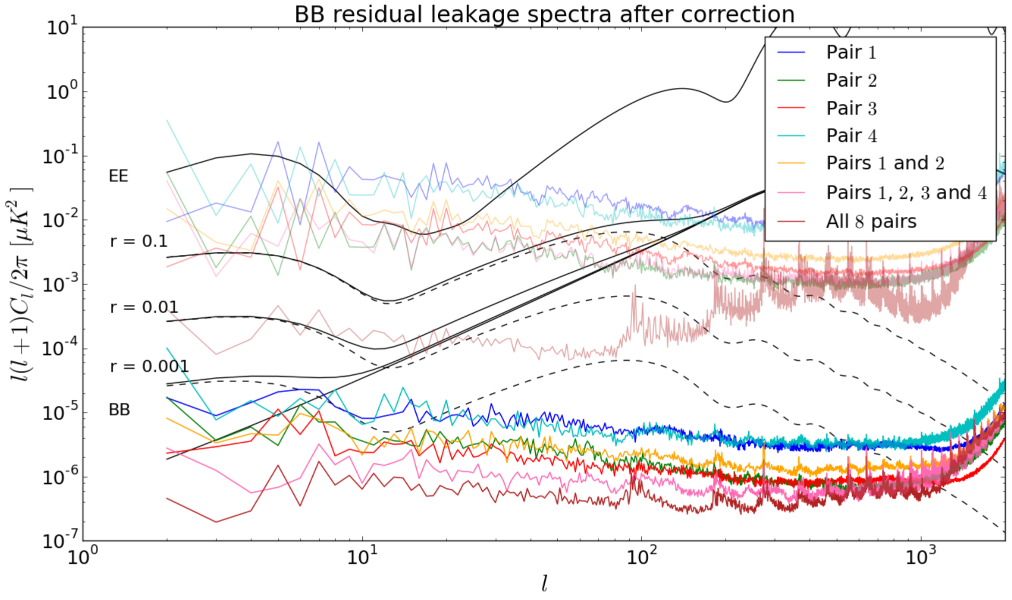

Figure 6.8: The residual leakage spectra, shown in solid colours, obtained after correction shows a significant improvement for all combinations of detectors and is subdominant to a primordial B-mode signal (except for a few multipoles). The residual leakage can be attributed to the variation of the spectral index of the Thermal Dust spectrum.

We see a significant improvement upon correction. The residual leakage is subdominant, up to intermediate multipoles as compared to a primordial B-mode signal at the necessary sensitivity to measure $r = 0.001$. The algorithm does not however correct for all of the leakage and leaves a residual. This is believed to be due to variation of the spectral index for the Thermal Dust emission across the sky. The estimator $\hat{y}_{\mathrm{TD}}$ is a single scalar quantity and gauges the mean value of the Thermal Dust spectral index. This complication was not experienced when we validated out correction algorithm in the previous section as the perfect template that we constructed was equally proportional to the leakage pattern on all pixels.

Pair label	Bandpass parameter	Measured amplitude				
	$\frac{1}{2}\Delta\alpha_{\mathrm{TD}} \times 10^2$	$\widehat{y}_{\mathrm{TD}} \times 10^4$				
		Config A	Config B	Config C	Config D	Config E
1	2.18	9.43	9.44	9.44	9.45	9.43
2	−0.64	−3.04	−3.05	−3.05	−3.04	−3.05
3	−0.79	−4.18	−4.19	−4.19	−4.18	−4.12
4	−2.06	−7.73	−7.74	−7.74	−7.75	−7.75
5	0.34	2.65	2.65	2.66	2.67	2.62
6	−0.16	0.11	0.11	0.11	0.10	0.11
7	−0.98	−4.05	−4.06	−4.06	−4.07	−4.07
8	2.66	12.69	12.71	12.70	12.70	12.69

Table 6.2: The amplitude of the template $\widehat{\boldsymbol{y}}_{\mathrm{TD}}$ as calculated by the correction algorithm is plotted against the bandpass mismatch parameter $\Delta\alpha_{\mathrm{TD}}$

Pair label	Bandpass parameter	Measured amplitude				
	$\frac{1}{2}\Delta\alpha_{\mathrm{TD}}$	$\widehat{y}_{\mathrm{TD}} \times 10^4$				
		Config A	Config B	Config C	Config D	Config E
1	2.18	9.55	9.55	9.53	9.50	9.54
2	−0.64	−3.00	−3.08	−3.04	−3.20	−3.12
3	−0.79	−4.28	−4.20	−4.178	−4.21	−4.15
4	−2.06	−7.88	−7.64	−7.75	−7.64	−7.67
5	0.34	2.59	2.58	2.67	2.83	2.72
6	−0.16	0.11	0.15	0.21	0.15	0.03
7	−0.98	−4.16	−4.02	−4.13	−4.18	−4.24
8	2.66	12.73	12.76	12.59	12.80	12.55

Table 6.3: The measured template amplitudes when timestream noise is added.

We wish to know how sensitive the correction algorithm is to a change in the scanning strategy. A significant deviation in the estimated value of y across scan strategies is undesirable since $\widehat{y}$ should be a function of the bandpass leakage parameter $\Delta\alpha$ alone. We also wish to know the effect of adding a white noise in the timestream on the estimation of y. Hence, we compare the results we have obtained to the set of simulations done without noise.

Comparing the estimated template amplitude across the five configurations, we see that the estimator is robust with hardly any variation between different configurations. The effect of adding a white noise to our simulated timestream has little effect on the estimation of the template amplitude due to the large volume of data points.

To test the relation between the estimated template amplitude $\widehat{\boldsymbol{y}}$ and the bandpass mismatch parameter $\Delta\alpha$ explicitly, we plot these two quantities against each other in (Figure 6.9).

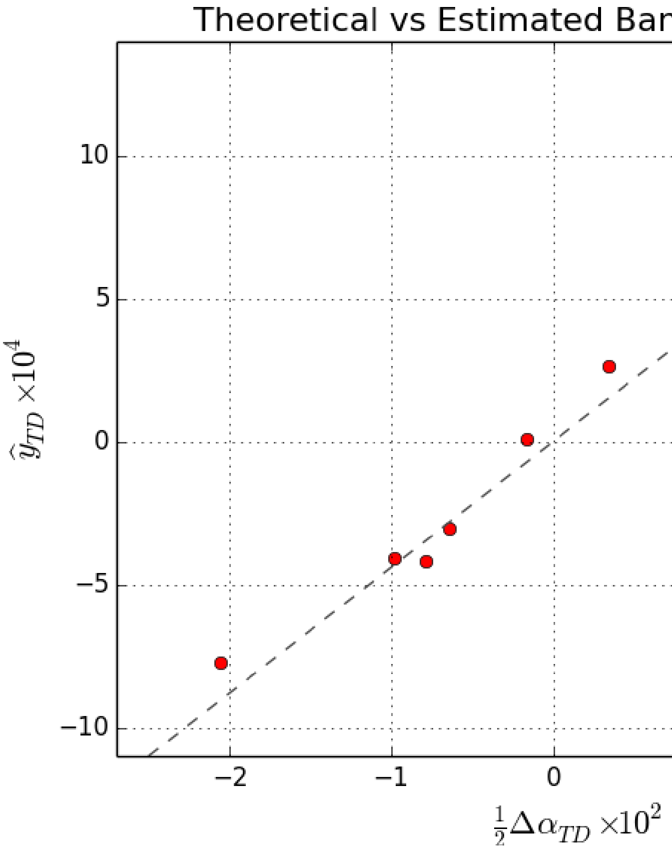

Figure 6.9: The figure shows the comparison between the calculated and estimated value of the bandpass mismatch parameter for thermal dust for the 8 detector pairs of Configuration A. This is a visual representation of (Table 6.2).

As expected, we have a very good agreement between the bandpass mismatch parameter and the estimated template amplitude. The best fit line passing through 0 is plotted along with the data points for the 8 detector pairs.

6.7 Correcting for Multiple Sources

The diffuse galactic emission contains contribution not only from Thermal Dust but also significantly from Synchrotron and Bremsstrahlung. Thermal Dust being the dominant galactic component above $100\mathrm{GHz}$ is the most significant contributor to the intensity to polarisation leakage at $145\mathrm{GHz}$. Synchrotron being the dominant component below $100\mathrm{GHz}$ is expected to have a non-negligible contribution at $145\mathrm{GHz}$. To demonstrate the leakage due to bandpass mismatch from Synchrotron alone, we perform a similar exercise as before but with input maps containing just Synchrotron and CMB emission. The leakage generated from such maps is compared to the Thermal Dust case by keeping all other scan parameters equivalent and is shown in (Figure 6.10).

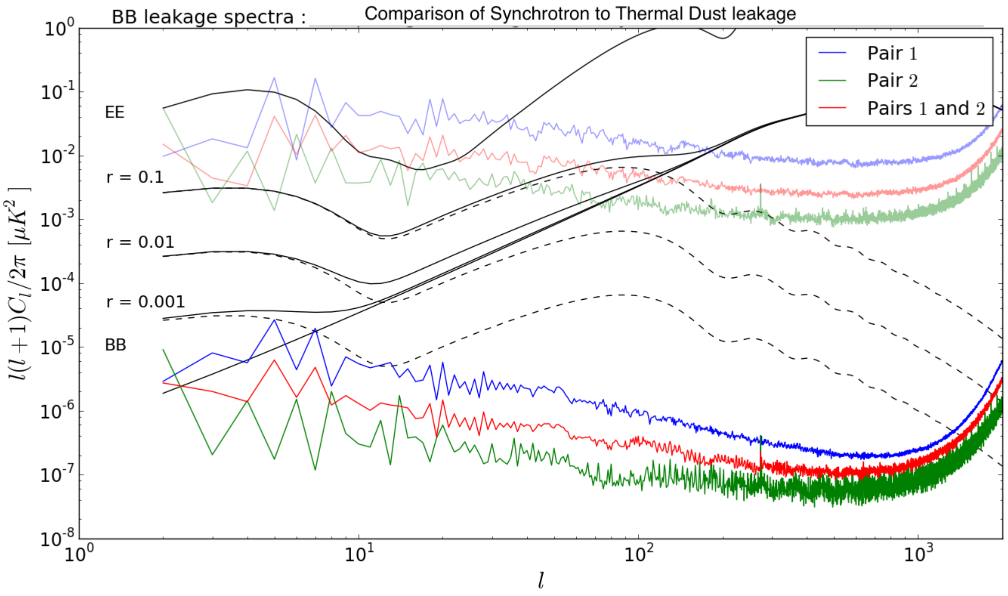

Figure 6.10: Comparing the leakage due to Synchrotron (solid colours) radiation to that of Thermal Dust (translucent) shows that at 145GHz the contribution from Synchrotron is very subdominant to Thermal Dust and is below the primordial B-mode signal for a fiducial value of $r = 0.001$.

We demonstrate now the correction of the bandpass mismatch error due to multiple foreground sources, in our case Thermal Dust and Synchrotron. Since in (Figure 6.10) we see that the leakage due to Synchrotron alone is subdominant to the primordial B-mode signal at $r = 0.001$, it would practically not be necessary to correct for Synchrotron. It still, however, is a useful exercise and we correct for both Thermal Dust and Synchrotron to check that the method is robust even when an additional sub-dominant source of leakage is present. We perform our correction for the two detector pairs 1 and 2 in (Table 6.1). As before we use the Thermal Dust template at 350GHz and we generate a new Synchrotron template at 60GHz with a 25% filter bandwidth. In order to test the effectiveness of the algorithm for multiple sources, we have kept out any other effect that might bias our estimator, hence this simulation is performed without any timestream noise.

We note that the argument of the Synchrotron emission being negligible holds true for the 145GHz channel. Going to lower frequencies where the Synchrotron emission is stronger, we expect to get a bigger leakage contribution from Synchrotron alone. This needs to be investigated in further studies.

Filtering out individual leakage component sequentially is a possibility. However, it is not guaranteed that it will not lead to a false estimation of the template amplitude due to the presence of other components. In such a case with added complexity to the input map, the estimator $\hat{\boldsymbol{y}}$ has the capability of simultaneously estimating the leakage amplitude of more than one source. It is interesting to demonstrate how the estimator performs for more than one template simultaneously and more than one source of leakage. We set up a test where we simulate the bandpass mismatch error for different cases of diffuse sources, Thermal Dust alone, Synchrotron alone, and Thermal Dust and Synchrotron both. We then estimate the

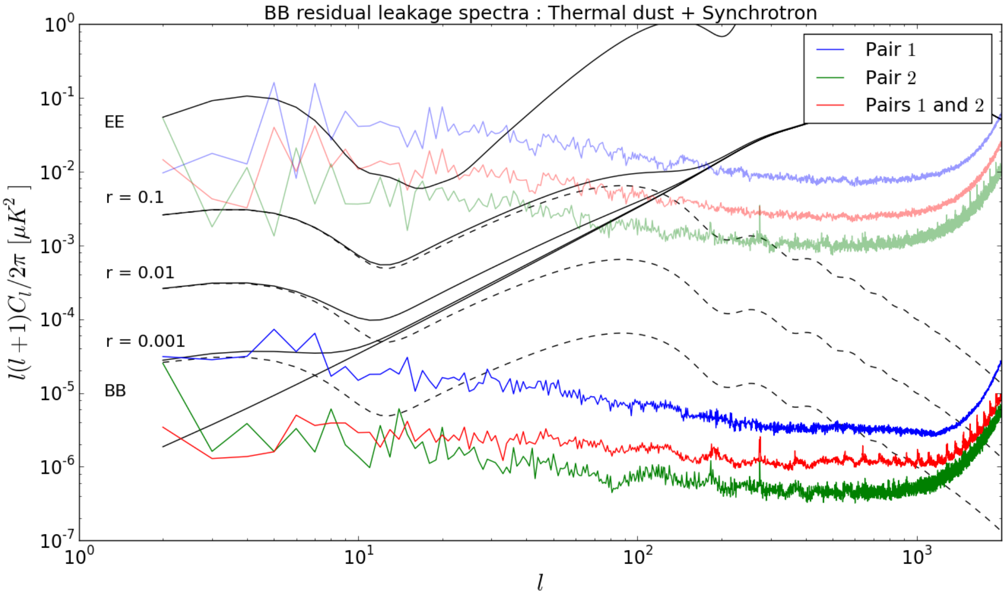

Figure 6.11: The figure demonstrated the correction to the bandpass mismatch error due to leakage from Thermal Dust and Synchrotron. The solid lines show the residual leakage after correction and comparing to (Figure 6.10) we see that the leakage from Synchrotron alone is still subdominant to the residual leakage signal.

leakage amplitude by fitting different combinations of template to the signal.

		Input foregrounds				
		Synchrotron	Thermal Dust	Synchrotron + Thermal Dust	Synchrotron	Synchrotron
$\widehat{y}_{\text{TD}} \times 10^4$	Pair 1	×	9.43	9.53	-0.102	$3.5e-11$
	Pair 2	×	-3.04	-3.08	0.0027	$-2.6e-10$
$\widehat{y}_{\text{Sync}} \times 10^3$	Pair 1	-1.81	×	-3.17	×	-1.81
	Pair 2	0.48	×	0.91	×	0.48

Table 6.4: The table demonstrates the performance of the estimator $\widehat{\boldsymbol{y}}$ under different circumstances. The second row tells us what are the components included in the input map apart from CMB. The next rows show the estimated template amplitudes of the two foreground components for Pair 1 and 2. A cross means that the template amplitude for that particular component was not calculated.

In columns 1 and 5 the only foreground source was Synchrotron. We see that estimating both the Thermal Dust and Synchrotron template amplitude had no bias on the weak Synchrotron signal and the estimated amplitude remains the same. In column 4 we forced an estimation of just the thermal dust amplitude alone and we do see some of the synchrotron signal contribution, although it is much subdominant to the actual value shown in column

2. The estimation of the synchrotron amplitude does show a large bias in the presence of a thermal dust signal as shown in column 3. This can be explained from the fact that the Synchrotron leakage is subdominant to the Thermal Dust residual leakage and is strongly biased by this. This does not impact negatively the detection of B-modes since the leakage from the Synchrotron alone was sub-dominant to the residual leakage from thermal dust.

6.8 Summary and Discussion

Bandpass mismatch between different detectors in the same frequency band was a major source of systematics in *Planck* and required extensive correction techniques. For a future CMB polarisation mission modelling and correcting the bandpass mismatch error is critical if we are to detect a B-mode signal with a sensitivity of $\delta r \sim 0.001$.

I have modelled the leakage induced by bandpass mismatch for a pair of orthogonally polarised detectors in (6.1) and in (6.2) I extended the model for an ensemble of multiple detectors. I calculated that the leakage in units of power is quadratic in the bandpass mismatch parameter $\Delta\alpha$. The leakage projects onto the polarisation maps in a predictable way given by the IQ and IU terms in the pixel covariance matrix for a single detector. This provides us an useful way of testing scan strategies and their ability in minimising bandpass mismatch leakage.

Using the spectral bands defined in (Table 6.1) I demonstrated the magnitude of the leakage of signal to B modes for different combinations of detectors. For the simulated 1% variation in the band edges, and for Thermal Dust alone, the leakage is substantial enough to mask out any primordial B-mode signal at $r = 0.001$ for all the cases I have studied in (6.2).

In (6.5) I tested out the correction algorithm, developed in (Chapter 4), for a toy model using a perfect template. This served as a sanity test and validated our correction algorithm. Using this algorithm I corrected the bandpass leakage demonstrated in (6.2). The residual leakage after correction for the Thermal Dust case was several orders of magnitude less than the leakage signal for all the cases I studied (6.6). The residual leakage after correction is demonstrated to be subdominant to a fiducial $r = 0.001$ signal. The presence of the residual signal is believed to be due to the variation of the thermal dust spectral index over the sky. Further studies are needed to quantify this and possibly model this as a second order effect that can be corrected.

The correction algorithm is shown to be robust to variation in can strategies and on the addition of timestream noise.

The contribution of the Synchrotron to the leakage is subdominant to that of the Thermal Dust, at least at $145\mathrm{GHZ}$ (Figure 6.10). Contribution from Synchrotron is expected to grow towards lower frequencies where the Synchrotron signal dominates and needs further study to quantify this. Using the correction algorithm, I demonstrated the correction of leakage for the case of Thermal Dust and Synchrotron together. Due to the relatively small contribution to the leakage by Synchrotron at $145\mathrm{GHz}$ we were not able to provide any substantial correction for it in the presence of Thermal Dust. This was because the residual leakage signal for Thermal Dust was dominant over that of the Synchrotron leakage signal. Further implementation of this algorithm is required at different frequencies where the leakage from different sources are comparable.

CHAPTER 7

BEAM ASYMMETRY AND MISMATCH

The detectors scanning the microwave sky have a spatial response to the incident radiation. The effect of this is a convolution of the signal on the sky with the detector response function. This response function in commonly referred to as the "beam" and under ideal circumstances is expected to be a symmetric Gaussian function. However, due to imperfections in the optics, effects of the detector time constant and positioning on the focal plane which causes an astigmatic aberration, the detector beam often assumes an irregular shape. To first order, the beam is well approximated by an elliptical Gaussian.

Scanning the sky with an elliptic beam produces systematic effects. Considering the Intensity signal alone, a detector visiting the same point in the sky with a different orientations will observe different quantities on each measurement. Similarly, different detectors with mismatched beams will observe the same point in the sky differently. These mismatches in the observation lead to intensity to polarisation and a cross polar leakage, and bias the estimation of the polarisation spectra.

The future generation of space missions will be particularly susceptible to systematic effects, especially due to beam mismatch errors, which can mask any primordial B-mode signal and severely limit the sensitivity of the mission. Beam effects have been considered among the principal sources of systematics for the *Planck* mission and have been studied in the following articles [95][90][96][89]. Prompted by the importance of beam systematics, several studies have been carried out to quantify and correct for the bias induced on the polarisation power spectra by it. Most efforts have been directed towards an analytic or semi-analytic approach. [89] convolves in the real space with an 'effective beam' and captures the effect of the average beam during an entire mission and is used in the *Planck* analyses. In the harmonic space [97][98][99] provide us effective ways of estimating the impact of such systematics with the last two providing effective correction algorithms. Deconvolution map-making, that is, making maps from the full time ordered data have also been implemented [91][92] as well as [99] which still perform the convolution in the harmonic space.

In the context of a next generation mission, two articles explore the implications and optimisation related to beam systematics [100][57].

In this chapter I present the results of scanning the CMB sky using a set of detectors with asymmetric beams. We propose an alternative method of simulating the time ordered data by exploiting the fast real-space convolution technique, described in chapter 5. We also provide a method of correcting for the beam systematics error.

7.1 Modelling the Signal, and Correcting Method

In the real space, the sky can be thought of as being integrated by the response (point spread function) of the detector. In the reference frame of the instrument, we can consider the response functions (B_I, B_Q, B_U) for the Stokes (I, Q, U) parameters independently. For some incident electromagnetic radiation, the total observed signal can written as

$$\boldsymbol{d} = \int \mathrm{d}\boldsymbol{r} \left[I(\boldsymbol{r})\mathrm{B}_I(\boldsymbol{r}) + Q(\boldsymbol{r})\mathrm{B}_Q(\boldsymbol{r}) + U(\boldsymbol{r})\mathrm{B}_U(\boldsymbol{r}) \right], \tag{7.1}$$

where the vector $\boldsymbol{r}$ points on the sky. These quantities are all defined in the instrument reference frame such that its $\mathrm{North} - \mathrm{South}$ axes coincide with that of the sky. Now, the instrument, as it tracks across the sky, will undergo a rotation changing the response functions. A rotation of the instrument in the counter-clockwise direction by an angle ψ translates to a transformation of the response function given by

$$B_I(\psi) = B_I(0) \tag{7.2a}$$
$$B_Q(\psi) = B_Q(0)\cos(2\psi) - B_U(0)\sin(2\psi) \tag{7.2b}$$
$$B_U(\psi) = B_Q(0)\sin(2\psi) + B_U(0)\cos(2\psi). \tag{7.2c}$$

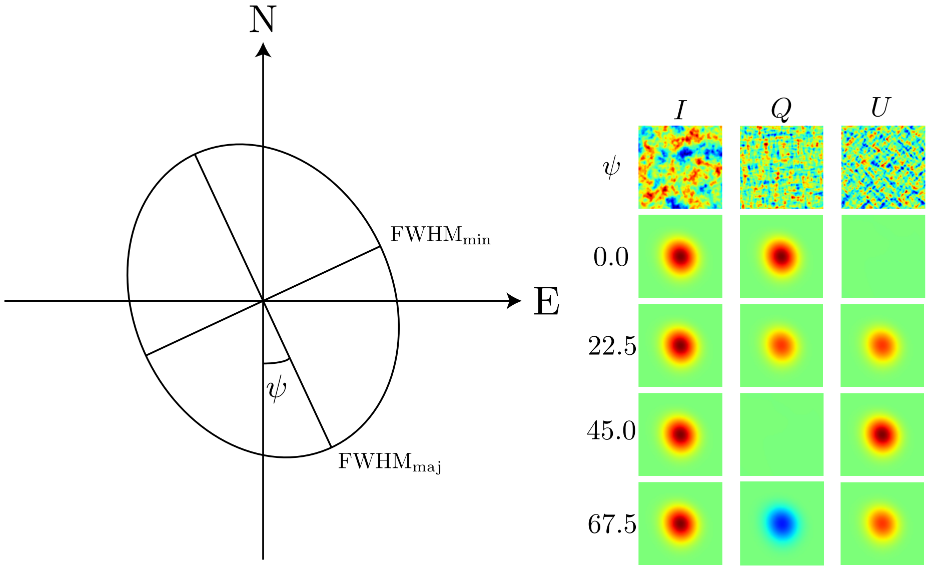

Figure 7.1: *Left*: The beam response function in the reference frame of the sky showing a rotation by an angle ψ. *Right*: In the sky frame, the Stokes maps of the incident radiation do not change. The response functions undergo a transformation as they are rotated by an angle ψ according to (Equation 7.2). Note that this does not include the physical rotation of the beam profile by the angle ψ.

Apart from the transformation (Equation 7.2), the beams undergoes an additional rotation of the entire beam profile by a rotation operator $\mathrm{R}(\psi)$, such that

$$B'_X(\psi) = \mathrm{R}(\psi) B_X(\psi), \tag{7.3}$$

where X is either I, Q or U.

Using the transformed beam response functions, the data model can now be defined in the reference frame of the sky. The Stokes parameters are defined in this frame and hence are not a function of ψ. The data model is given by

$$\boldsymbol{d}_t = \int \mathrm{d}\boldsymbol{r}' \left[I(\boldsymbol{r}')\mathrm{B}'_I(\boldsymbol{r},\boldsymbol{r}',\psi) + Q(\boldsymbol{r}')\mathrm{B}'_Q(\boldsymbol{r},\boldsymbol{r}',\psi) + U(\boldsymbol{r}')\mathrm{B}'_U(\boldsymbol{r},\boldsymbol{r}',\psi) \right]. \tag{7.4}$$

where $B'_X(\boldsymbol{r},\boldsymbol{r}',\psi)$ is the beam that has been positioned at $\boldsymbol{r}$, rotated in the sky frame and transformed by the relations (Equation 7.2). The integration is over $\boldsymbol{r}'$.

The instrument observes each of the sky pixels at different times, each time making an approach at a different angle ψ. Any asymmetry in the shape of the beam response function will lead to a mismatch in the measured signal on the same sky pixels. Direct detection experiments that rely on pair differencing or combining the time ordered data from multiple detectors can suffer from a few classes of errors that are related to beam systematics. As shown in [100], we can classify these as

- **Gain mismatch**: This is when the beam response functions for different detectors differs in its absolute magnitude. This situation is analogous to the bandpass mismatch effect we studied earlier.
- **Pointing mismatch**. This happens when the centre of the different beams are not coincident.
- **Beam ellipticity**. This is caused by astigmatic aberrations and the effect of the detector time constant. This manifests as somewhat elongated beam profiles.

Even for single detector maps, the last two cases are capable of generating intensity to polarisation leakage if the map making is done by using inaccurate pointing data and assuming a symmetric Gaussian beam. The intensity signal being a few orders of magnitude greater than the polarisation is the main source of contamination.

The fast real-space beam convolution method described in section 5.3 provides us a method of simulating time-ordered data that accurately depicts the effect of scanning the CMB sky with a beam of any shape and preserves the effect of rotation of the beam as it moves along the sky. The signal thus obtained mimics exactly (up to discrete pixelisation effects), the scan of the sky by a detector without making any simplifications or assumptions.

We propose an iterative deconvolution method to correct for the Intensity to Polarisation leakage due to asymmetric and mismatched beams. We use the real space beam convolution algorithm for this purpose. The mismatched signal projects on to the map in a predictable manner if we have knowledge of the beam response function and the pointing data. It is possible to re project the leakage pattern from a template map of the CMB intensity sky by scanning the template map with the known beam and pointing data. The re-projected leakage maps can thus be subtracted from the original observed maps and produce maps that should theoretically be unbiased by the beam mismatch errors.

An Intensity template map can be reconstructed by averaging the signal from the full detector set of a frequency band. In reality, the Intensity template map is not exact and contains small deviations, both due to detector noise and from errors generated by scanning with the imperfect beams. Moreover, this also assumes we have an almost perfect knowledge of, at least, the Intensity beam profile. The intensity beams are expected to be well constrained from ground calibration and in-flight observation of planets [90], and by using geometric optics simulations with tools such as GRASP. Since the Intensity maps, from current generation of experiments, are scanned with a high signal-to-noise ratio, we can safely assume that the small deviations on the Intensity map will not drastically limit the correction method.

7.2 Results for Elliptical Beams

Using our real space convolution technique we have tested a few configurations of elliptical beams for the scan configuration A described in (Table 3.1). As input maps we consider (I,Q,U) un-smoothed *HEALPix* maps at $\mathrm{nside} = 4096$ containing CMB alone. We consider an ideal configuration of 4 detectors pointing at the same position in the sky. The ellipticity of the beams ϵ have been defined such that

$$\epsilon = \frac{\mathrm{FWHM}^2_{\mathrm{maj}} - \mathrm{FWHM}^2_{\mathrm{min}}}{\mathrm{FWHM}^2_{\mathrm{maj}} + \mathrm{FWHM}^2_{\mathrm{min}}} \tag{7.5}$$

The leakage map is calculated by subtracting from the map generated by the elliptical beams, the map generated by scanning the same input maps using symmetric Gaussian beams. The FWHM of the symmetric beams is estimated by fitting the resulting TT spectrum of the map generated by the elliptical beams to the fiducial TT spectrum used to generate the input maps. We have for now not added any noise in the timestream. The size of the pixelised beam maps was kept at $4\mathrm{FWHM}$ of the beams.

To make the Intensity template map we take the map that has been reconstructed from the signal of the four detectors with elliptical beams. An effective smoothing scale of the observed map is estimated by using a simple chi-square estimator. We fit a fiducial TT spectrum to the TT spectrum recovered from the simulation. The intensity map is then de-convolved for a symmetric Gaussian with the estimated FWHM in the harmonic space. We use a Weiner filter to reduce any noise at high-l from blowing up.

By scanning our Intensity template map with the pointing data and the pixelised intensity beam map, we re project the leakage pattern on the polarisation sky. The corrected polarisation map is obtained by subtracting out the re projected leakage from our biased maps.

The result for the correction, using the method described above, is plotted along with the leakage spectra in the following plots.

We propose three hypothetical scenarios where the major axes of the elliptic beams are oriented in a specified manner in relation to the polarisation axes. They are

- Setup 1: Major axis oriented along the detector polarisation axis.
- Setup 2: Major axis oriented at $45°$ to the detector polarisation axis.
- Setup 3: Major axis oriented at $22.5°$ to the detector polarisation axis.

These three setups illustrate an interesting feature of how the Intensity signal couples with the polarisation signal.

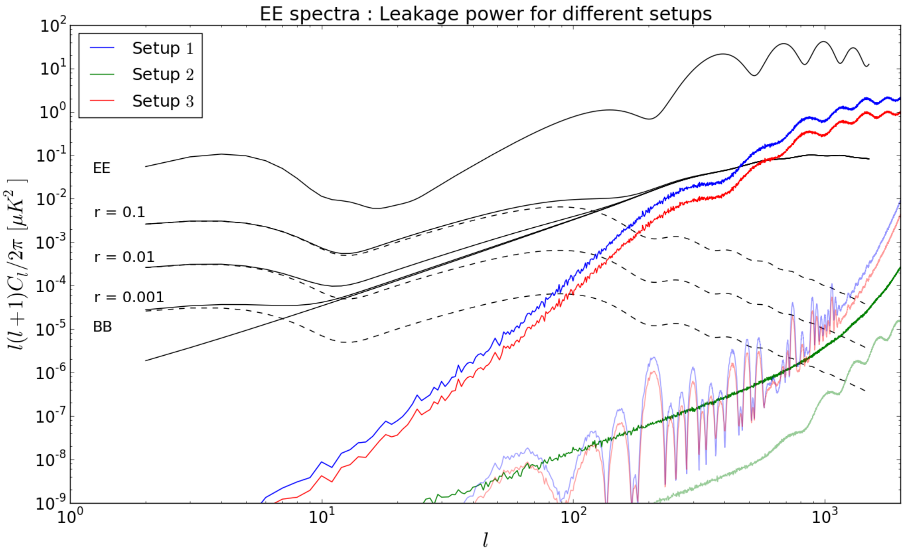

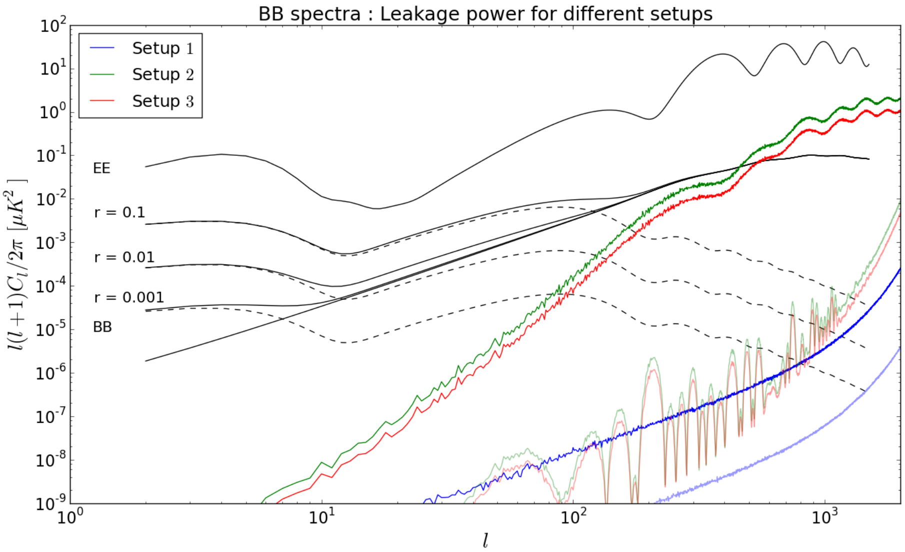

Figure 7.2: These plots illustrate the coupling between the Intensity to the EE and BB spectra. In solid colours are plotted the leakage from Intensity to Polarisation due to beam asymmetry for the three setups defined before. The residual leakage after correction is plotted using the translucent lines. The ellipticity of the beams used here was $\epsilon = 0.05$.

The coupling between the Intensity and the B-mode signal is zero when the major axes of the beams are oriented along the polarisation axes. The converse takes place when they are at an angle of 45° with each other and the coupling between Intensity and the E-mode signal is zero. This is in accordance with the analytical results computed in [97][99]. The leakage amplitude between the E and B modes become equal midway between the two extreme cases when the major axis is oriented at $22.5°$ to the polarisation axis.

As we had shown in 5.3, the real space convolution introduces a white noise due to pixelisation and numerical effects on to the reconstructed maps. This is seen here in (Figure 7.2) in the EE leakage spectrum for Setup 2 and the BB leakage spectrum for Setup 3. This limits the effectiveness of using this method to estimate and correct for systematics but is low enough to not be a concern for the sensitivity that we are interested in.

The leakage spectra for all cases is strongly subdued after correction. The residual leakage spectra are below the fiducial $r = 0.001$ plot for all $l < 900$.

The magnitude of the leakage is expected to be quadratic in beam ellipticity [97]. This is demonstrated by the set of simulations performed using beams with different ellipticity. The following figures show the B-mode leakage due to elliptical beams with $\epsilon = 0.05, 0.10, 0.15$ for Setup 3, calculated using the real space space beam convolution method.

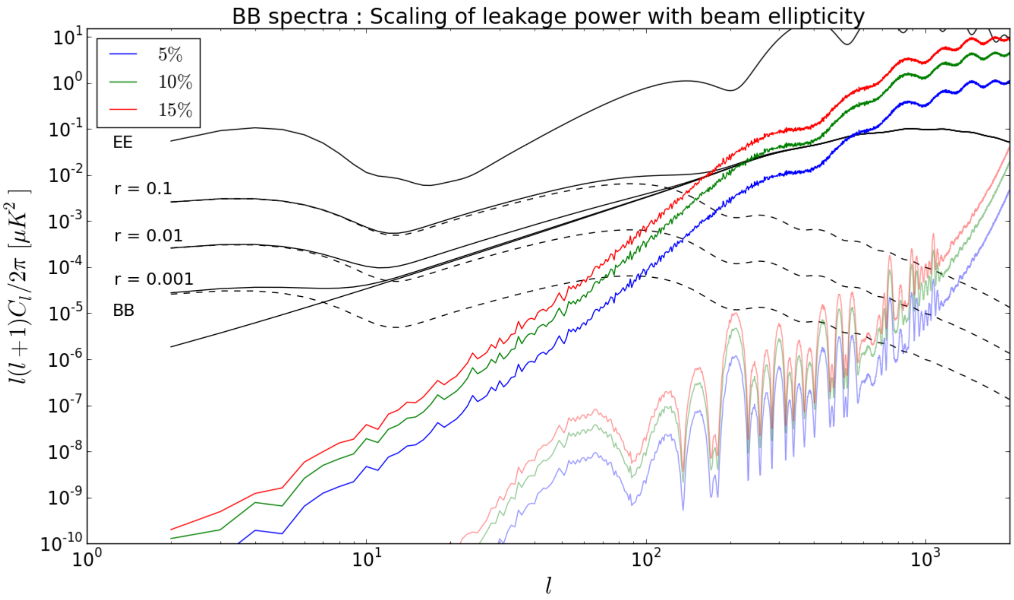

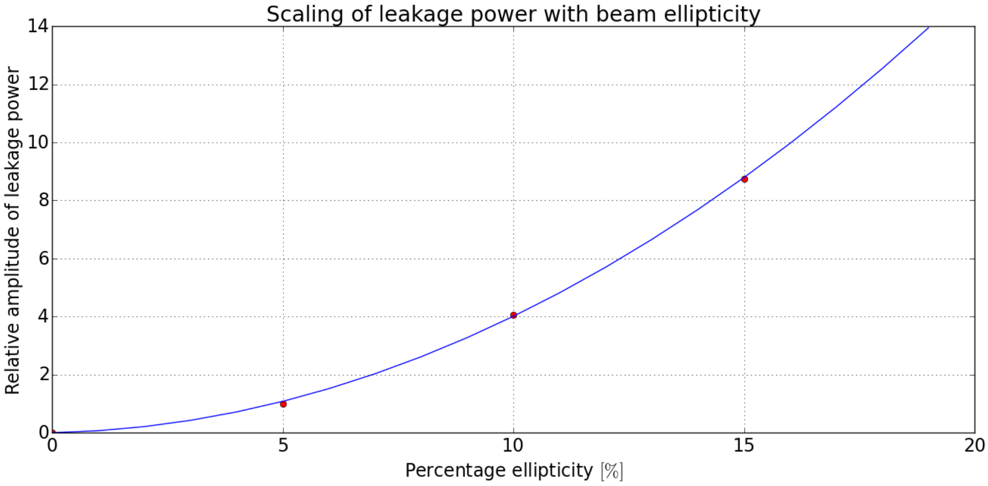

Figure 7.3: *Top*: The figure illustrates the scaling of the BB leakage power with beam ellipticity. The effective size of the beam has been kept constant at $8'$. The ellipticity is given as a percentage such that $\epsilon = 0.05$ corresponds to 5%. *Bottom*: The relative amplitudes of the leakage spectra are plotted as a function of the beam ellipticity. The amplitude of each leakage spectrum is measured against the leakage spectrum for the 5% case.

We also demonstrate below the effect the size of the beam has on the amplitude of the leakage signal.

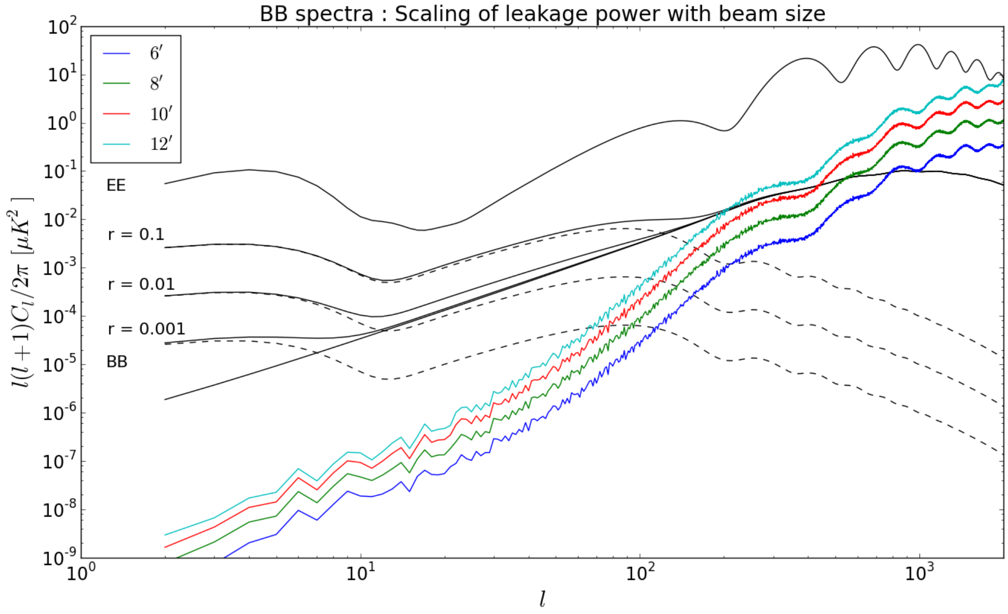

Figure 7.4: The magnitude of the leakage to B-modes is plotted for various beam sizes but with a fixed ellipticity of 0.1.

Similar to increasing the ellipticity of the beams, increasing the size of the beam monotonically increases the leakage power at all scales.

The hypothetical configurations with elliptical beams studied in this section serve as a validation and verification for the real space beam convolution method when compared to previous analytical results. It provides a useful method of estimating the magnitude and shape of the polarisation leakage spectra for a simulation that preserves all the intricacies of the motion of an asymmetric beam on the sky. The correction method was also tested and showed, for the studied cases, that the leakage signal is reduced by a few orders of magnitude. This brings it well within tolerance levels set for the next generation of space missions.

7.3 Simulated Beams for the CORE Proposal

A realistic beam profile is expected to not only be elliptic but also contain other irregularities dictated by optics. We perform a similar exercise as in the previous section by using as out scanning beams those computed using GRASP for three locations on the focal plane, the ’boresight’, ’high’ and ’low’ detectors as defined in [57]. These beams were generated for the $145\mathrm{GHz}$ channel and for the crossed-Dragone design proposed for the CORE mission. ’High’ refers to the position on the focal plane that is 4° towards the spin axis and ’low’ refers to the equivalent position in the opposite direction. For this purpose 4 sets of beams were generated, two for the boresight and one each for the high and low detectors. The asymmetric beams are expected to generate an intensity to polarisation leakage and a more sub-dominant cross polar leakage.

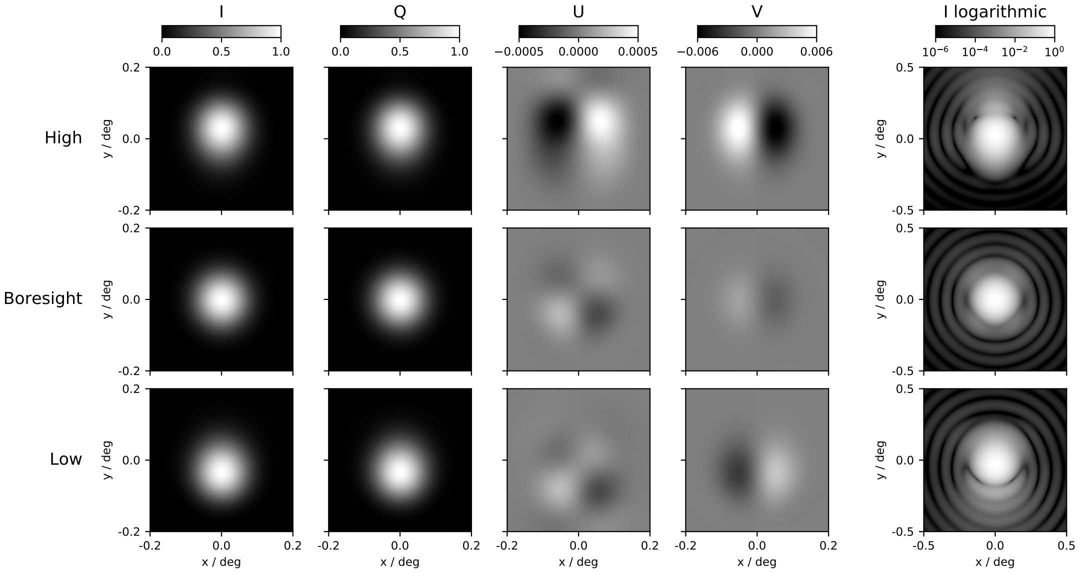

Figure 7.5: The figure shows the beams generated for the CORE $145\mathrm{GHz}$ channel using GRASP for the crossed-Dragone configuration. The beams generated for the 'boresight', 'low' and 'high' positions of the focal plane. The beams have been normalised to unity at the peak for Intensity. *Image credit*: Mark Ashdown

The simulations were done at a high resolution with the input map at $\mathrm{nside} = 4096$. The scan strategy used is configuration A in (Table 3.1) which is the CORE baseline and no timestream noise was added. Due to the limited number of simulated beams available, we performed our simulation for different combinations of the detectors. Simulations with a single and with both 'boresight' detectors were performed, and simulations with the single 'high' and 'low' detectors were performed independently.

In (Figure 7.6) we show the leakage generated by scanning with the simulated beams for a period of one year. As can be seen from the plot of the GRASP beams (Figure 7.5), the beams at 'high' and 'low' are considerably more elliptical than the boresight beam. This is reflected in the single detector leakage power spectrum where the amplitude of leakage for the 'boresight' detector is much weaker. The spectra for the high and low detectors were nearly identical in magnitude and shape and hence we plot just for the 'low' detector and term it as the 'edge' detector. A considerable improvement, by over a magnitude in power at all scales, is observed when combining both 'boresight' detectors.

We see that for a mission such as CORE, the leakage from the detectors at the edges of the focal plane can prove very restrictive in the measurement of any primordial B-mode signal. The leakage from a single 'edge' detector is at the level of the E-mode spectrum. For the pair of 'boresight' detectors, the leakage starts dominating over the fiducial $r = 0.001$ signal at $l = 100$.

After correcting for the leakage signal, we see a significant improvement for the case of the 'edge' detectors. Their magnitude has been brought down to levels comparable to a primordial B-mode signal at a few times $r = 0.001$ and the residual leakage is dominated by E to B mode leakage. The correction for the single 'boresight' detector is however limited by the pixelisation noise induced by the real-space scanning and is not conclusive. The case for the pair of 'boresight' detectors is, however, better tackled by the correction method due to a better

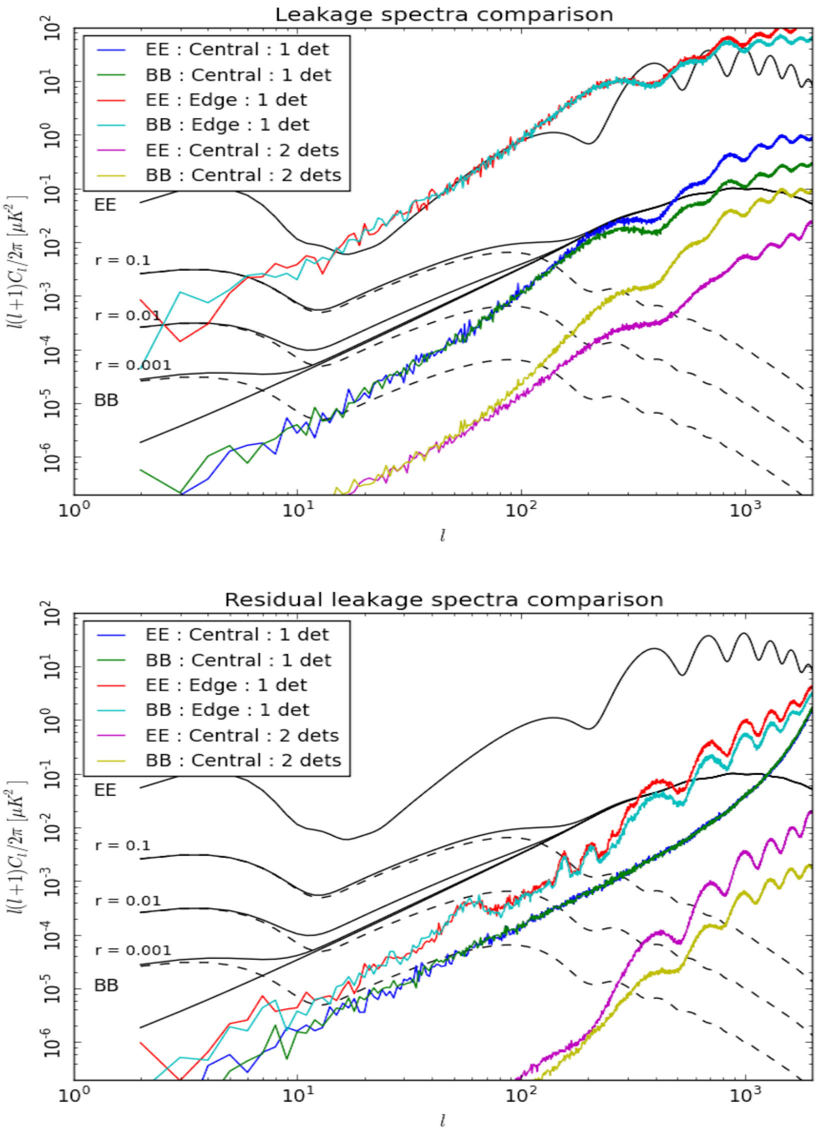

Figure 7.6: The leakage spectra generated from scanning the sky with the asymmetric beams simulated by GRASP for the $145\mathrm{GHz}$ band detectors. The ’edge’ detector is the referred to as ’low’ earlier. The simulations have been done foe different combinations of the available detector beams. The second plot gives us the residual leakage after the real space correction method is applied.

conditioning of the pixel covariance matrix from the pair of detectors. The residual leakage in this case appears to be dominated by E to B leakage that has not been corrected for and is subdominant to the fiducial $r = 0.001$ signal up to $l \approx 200$.

7.4 Summary and Discussion

Leakage due to beam ellipticity and mismatch between detectors is considered an important source of systematic contamination for a future CMB space mission. It can lead to a leakage of signal both from intensity to polarisation and from E to B modes.

I show the effect of scanning the sky for different settings of elliptic beams using the real space beam convolution method. For the beam configurations we studied, the leakage was significant enough to mask the fiducial BB spectrum for $r = 0.001$ above l of a few tens.

To correct for the leakage I implemented an iterative method using the real space convolution technique. The residual leakages for the elliptic beams were corrected and were brought down to within accepted limits.

I also studied the effect of simulated beams for the CORE optics design for detectors at the centre and the edge of the focal plane. The edge beams were significantly elliptic and produced a leakage signal comparable to the E modes. Correction of the leakage brought it down below the $r = 0.01$ B mode signal. The detector pair at the boresight fared the best as they were the most symmetric among the set. Further simulations with a bigger set of simulated beams are required as the set of simulated beams was very limited.

A simulation with a real space beam convolution is an important tool that can generate realistic time ordered signals that preserves all the intricacies of an actual scan and the motion of the beam on the sky. With the verification of expected results using this tool (7.2), and offering a procedure to mitigate beam systematic effects, it complements other analytic tools that work at the power spectrum level or provide deconvolution map making solutions.

CHAPTER 8

CONCLUSION

In this thesis I presented the work that I have performed as a doctoral student at APC, Paris. The main objective was to optimise a next generation CMB polarisation space mission to detect any primordial B-mode signal with a sensitivity of $\delta r \approx 0.001$. This work was done assuming no half-wave plate is used, to demonstrate that in its absence we are still capable of mitigating contamination from systematic effects and achieving the required sensitivity.

I had the opportunity to work at the proposal stages for COrE+ and CORE and have collaborated with researchers working on the LiteBIRD mission. The work presented here has been used in the set of publications accompanying the CORE proposal especially in [57] and [56]. I have also contributed significantly to the paper on bandpass mismatch [68].

To prepare a next generation CMB polarisation mission with ambitious goals of detecting primordial B-modes, it is necessary to optimise different aspects of it. In this thesis I have studied two such areas, the scan strategy, and data analysis techniques to mitigate systematic contamination.

To perform the simulation and analysis tasks I developed a comprehensive pipeline written in Python using optimised Numpy and Scipy libraries and is MPI parallelised. I also developed a fast algorithm to convolve a pixelised sky map in real space that performs satisfactorily at the sensitivities required for most of our analysis. Further development and fine tuning is required on this algorithm to fix some of its pixelisation issues.

A future mission such as CORE or LiteBIRD will be placed in orbit at the $\mathrm{L2}$ Lagrange point and scan the sky with a combination of two rotational motions. We can specify the scan strategy of the mission with a small set of parameters and varying these will give us different configurations. I studied the features of a few variants of these scan strategies regarding their ability to produce polarisation maps and their sensitivity to polarisation. By comparing the outcome of different situations, I can conclude that, a larger precession angle is better capable of producing single detector all sky polarisation maps on the timescale of a year. The cases studied were not exhaustive and I mentioned examples from among the broad classes of scan configurations possible. A more extensive and exhaustive simulation exercise will provide more detail and the five examples studied give us an overview of the possibilities. Certain configurations produce unfavourable results and I have identified them.

A sensitive mission is expected to be limited by systematic contaminations due to non idealities in the instrument. These have the ability to leak the much stronger intensity signal to polarisation and mask out any primordial B-mode signal. One of the most important tasks during my study was to develop a general data model for a pair of mismatched orthogonally polarised detectors and a method of correcting the induced leakage. The correction method relies on fitting a set of appropriate templates to the leakage signal. Subtracting out the estimated leakage at the timestream level provides us unbiased polarisation maps.

I studied the case of bandpass mismatch extensively and modelled the leakage signal and its projection on to polarisation maps. The magnitude of the leakage had a direct relation to the scan strategy and gives an example how systematics can be minimised by scan strategy alone. The leakage signal seen in B-modes is substantial to mask out a primordial signal at $r = 0.001$ and thus needs to be corrected. I validated the correction method using a toy model of bandpass mismatch error and concluded that it works as expected. I proceeded to correct for the bandpass leakage signal from thermal dust and was successful in reducing the leakage to below accepted levels. The correction algorithm is shown to be robust and effective for correcting multiple sources of leakage. Further modelling of the diffuse emissions are required to explain the residual leakage. Extensions of the correction algorithm can be made to further reduce the leakage. Further development of this is hence required. More simulations are required at frequency bands below $145\mathrm{GHz}$ to assess the impact of Synchrotron and free-free.

I also studied the issue of asymmetric beams. This was a major issue for the *Planck* mission and is expected to be so for a next generation mission. Using the real space beam convolution algorithm I developed a method of correcting for the leakage induced by beams of any shape. I tested a few cases of elliptic beams and performed the correction procedure that I developed. The level of the leakage induced was significant enough to mask out a primordial B-mode signal at $r = 0.001$ above a few tens of l. The correction procedure was effective in reducing the error by a few orders of magnitude and brought down the leakage to within accepted limits. I also performed tests on simulated beams for the CORE mission. The leakage from beams at the edge of the focal plane is at the level of the E-mode signal and the beams at the centre of the focal plane perform significantly better due to their better symmetry. The correction method was effective in reducing the leakage for all the cases but a larger set of simulated beams is required to better demonstrate the full capability of the correction algorithm.

As of now, the LiteBIRD mission is the only experiment undergoing a phase of study. I have collaborated with researchers working on it on the issue of bandpass mismatch and optimising the scan strategy. A “probe class” mission is being studied for a proposal to NASA during $2020-2021$ and I have been volunteering on the team studying systematic effects.

The tools developed over the last three years will be useful for future studies. They can be used in the context of the ongoing LiteBIRD phase A or for the “probe class” mission studies in the US, or for other future opportunities.

BIBLIOGRAPHY

[1] R. A. Alpher and R. C. Herman, “On the relative abundance of the elements,” *Phys. Rev.*, vol. 74, pp. 1737–1742, Dec 1948.

[2] G. Gamow, “The origin of elements and the separation of galaxies,” *Phys. Rev.*, vol. 74, pp. 505–506, Aug 1948.

[3] A. A. Penzias and R. W. Wilson, “A Measurement of excess antenna temperature at 4080-Mc/s,” *Astrophys. J.*, vol. 142, pp. 419–421, 1965.

[4] R. H. Dicke, P. J. E. Peebles, P. G. Roll, and D. T. Wilkinson, “Cosmic Black-Body Radiation.,” *Astrophys. J.*, vol. 142, pp. 414–419, July 1965.

[5] G. F. Smoot, C. L. Bennett, A. Kogut, E. L. Wright, J. Aymon, N. W. Boggess, E. S. Cheng, G. de Amici, S. Gulkis, M. G. Hauser, G. Hinshaw, P. D. Jackson, M. Janssen, E. Kaita, T. Kelsall, P. Keegstra, C. Lineweaver, K. Loewenstein, P. Lubin, J. Mather, S. S. Meyer, S. H. Moseley, T. Murdock, L. Rokke, R. F. Silverberg, L. Tenorio, R. Weiss, and D. T. Wilkinson, “Structure in the COBE differential microwave radiometer first-year maps,”

[6] J. C. Mather, E. S. Cheng, D. A. Cottingham, R. E. Eplee, Jr., D. J. Fixsen, T. Hewagama, R. B. Isaacman, K. A. Jensen, S. S. Meyer, P. D. Noerdlinger, S. M. Read, L. P. Rosen, R. A. Shafer, E. L. Wright, C. L. Bennett, N. W. Boggess, M. G. Hauser, T. Kelsall, S. H. Moseley, Jr., R. F. Silverberg, G. F. Smoot, R. Weiss, and D. T. Wilkinson, “Measurement of the cosmic microwave background spectrum by the COBE FIRAS instrument,”

[7] E. Kolb and M. Turner, *The Early Universe*.
Frontiers in physics, Avalon Publishing, 1994.

[8] D. Baumann, “Inflation,” in *Physics of the large and the small, TASI 09, proceedings of the Theoretical Advanced Study Institute in Elementary Particle Physics, Boulder, Colorado, USA, 1-26 June 2009*, pp. 523–686, 2011.

[9] S. Dodelson, *Modern cosmology*.
San Diego, CA: Academic Press, 2003.

[10] S. Weinberg, *Gravitation and Cosmology: Principles and Applications of the General Theory of Relativity*.
New York, NY: Wiley, 1972.

[11] M. Trodden and S. M. Carroll, “TASI lectures: Introduction to cosmology,” in *Progress in string theory. Proceedings, Summer School, TASI 2003, Boulder, USA, June 2-27, 2003*, pp. 703–793, 2004.

[,703(2004)].

[12] P. Ntelis *et al.*, “Exploring cosmic homogeneity with the BOSS DR12 galaxy sample,” *JCAP*, vol. 1706, no. 06, p. 019, 2017.

[13] S. Perlmutter *et al.*, “Measurements of Omega and Lambda from 42 high redshift supernovae,” *Astrophys. J.*, vol. 517, pp. 565–586, 1999.

[14] A. G. Riess *et al.*, “Observational evidence from supernovae for an accelerating universe and a cosmological constant,” *Astron. J.*, vol. 116, pp. 1009–1038, 1998.

[15] P. A. R. Ade *et al.*, “Planck 2015 results. XIII. Cosmological parameters,” *Astron. Astrophys.*, vol. 594, p. A13, 2016.

[16] A. G. Riess, L. M. Macri, S. L. Hoffmann, D. Scolnic, S. Casertano, A. V. Filippenko, B. E. Tucker, M. J. Reid, D. O. Jones, J. M. Silverman, R. Chornock, P. Challis, W. Yuan, P. J. Brown, and R. J. Foley, “A 2.4determination of the local value of the hubble constant,” *The Astrophysical Journal*, vol. 826, no. 1, p. 56, 2016.

[17] A. A. Starobinskiĭ, “Spectrum of relict gravitational radiation and the early state of the universe,” *Soviet Journal of Experimental and Theoretical Physics Letters*, vol. 30, p. 682, Dec. 1979.

[18] A. H. Guth, “Inflationary universe: A possible solution to the horizon and flatness problems,” *Phys. Rev. D*, vol. 23, pp. 347–356, Jan 1981.

[19] A. D. Linde, “A New Inflationary Universe Scenario: A Possible Solution of the Horizon, Flatness, Homogeneity, Isotropy and Primordial Monopole Problems,” *Phys. Lett.*, vol. 108B, pp. 389–393, 1982.

[20] A. D. Linde, “Inflationary Cosmology,” *Lect. Notes Phys.*, vol. 738, pp. 1–54, 2008.

[21] BICEP2/Keck and P. Collaborations, “Joint analysis of bicep2/keck array and planck data,” *Phys. Rev. Lett.*, vol. 114, p. 101301, Mar 2015.

[22] E. F. Bunn, “Calculations of cosmic background radiation anisotropies and implications,” 1996.

[23] R. K. Sachs and A. M. Wolfe, “Perturbations of a cosmological model and angular variations of the microwave background,” *Astrophys. J.*, vol. 147, pp. 73–90, 1967. [Gen. Rel. Grav.39,1929(2007)].

[24] W. Hu, N. Sugiyama, and J. Silk, “The Physics of microwave background anisotropies,” 1995.

[25] G. B. Rybicki and A. P. Lightman, *Radiative Processes in Astrophysics*. Wiley, 1979.

[26] M. Zaldarriaga and U. c. v. Seljak, “All-sky analysis of polarization in the microwave background,” *Phys. Rev. D*, vol. 55, pp. 1830–1840, Feb 1997.

[27] A. Kosowsky, “Cosmic microwave background polarization,” *Annals Phys.*, vol. 246, pp. 49–85, 1996.

[28] W. Hu and M. J. White, "A CMB polarization primer," *New Astron.*, vol. 2, p. 323, 1997.

[29] J. Kaplan, J. Delabrouille, P. Fosalba, and C. Rosset, "Cmb polarization as complementary information to anisotropies," *Comptes Rendus Physique*, vol. 4, p. 917, 2003.

[30] A. Lewis and A. Challinor, "Weak gravitational lensing of the cmb," *Phys. Rept.*, vol. 429, pp. 1–65, 2006.

[31] W. Hu, "Weak lensing of the cmb: A harmonic approach," *Phys. Rev. D*, vol. 62, p. 043007, Jul 2000.

[32] B. D. Sherwin *et al.*, "Two-season Atacama Cosmology Telescope polarimeter lensing power spectrum," *Phys. Rev.*, vol. D95, no. 12, p. 123529, 2017.

[33] P. A. R. Ade *et al.*, "BICEP2 / Keck Array VIII: Measurement of gravitational lensing from large-scale B-mode polarization," *Astrophys. J.*, vol. 833, no. 2, p. 228, 2016.

[34] P. A. R. Ade *et al.*, "Planck 2015 results. XV. Gravitational lensing," *Astron. Astrophys.*, vol. 594, p. A15, 2016.

[35] P. A. R. Ade, Y. Akiba, A. E. Anthony, K. Arnold, M. Atlas, D. Barron, D. Boettger, J. Borrill, S. Chapman, Y. Chinone, M. Dobbs, T. Elleflot, J. Errard, G. Fabbian, C. Feng, D. Flanigan, A. Gilbert, W. Grainger, N. W. Halverson, M. Hasegawa, K. Hattori, M. Hazumi, W. L. Holzapfel, Y. Hori, J. Howard, P. Hyland, Y. Inoue, G. C. Jaehnig, A. Jaffe, B. Keating, Z. Kermish, R. Keskitalo, T. Kisner, M. Le Jeune, A. T. Lee, E. Linder, E. M. Leitch, M. Lungu, F. Matsuda, T. Matsumura, X. Meng, N. J. Miller, H. Morii, S. Moyerman, M. J. Myers, M. Navaroli, H. Nishino, H. Paar, J. Peloton, E. Quealy, G. Rebeiz, C. L. Reichardt, P. L. Richards, C. Ross, I. Schanning, D. E. Schenck, B. Sherwin, A. Shimizu, C. Shimmin, M. Shimon, P. Siritanasak, G. Smecher, H. Spieler, N. Stebor, B. Steinbach, R. Stompor, A. Suzuki, S. Takakura, T. Tomaru, B. Wilson, A. Yadav, and O. Zahn, "Measurement of the cosmic microwave background polarization lensing power spectrum with the polarbear experiment," *Phys. Rev. Lett.*, vol. 113, p. 021301, Jul 2014.

[36] J. Lesgourgues and S. Pastor, "Massive neutrinos and cosmology," *Phys. Rept.*, vol. 429, pp. 307–379, 2006.

[37] J. Lesgourgues and S. Pastor, "Neutrino cosmology and planck," *New Journal of Physics*, vol. 16, no. 6, p. 065002, 2014.

[38] K. A. Olive *et al.*, "Review of Particle Physics," *Chin. Phys.*, vol. C38, p. 090001, 2014.

[39] E. Di Valentino, E. Giusarma, M. Lattanzi, O. Mena, A. Melchiorri, and J. Silk, "Cosmological Axion and neutrino mass constraints from Planck 2015 temperature and polarization data," *Phys. Lett.*, vol. B752, pp. 182–185, 2016.

[40] R. H. Becker, X. Fan, R. L. White, M. A. Strauss, V. K. Narayanan, R. H. Lupton, J. E. Gunn, J. Annis, N. A. Bahcall, J. Brinkmann, A. J. Connolly, I. Csabai, P. C. Czarapata, M. Doi, T. M. Heckman, G. S. Hennessy, Željko Ivezić, G. R. Knapp, D. Q. Lamb, T. A. McKay, J. A. Munn, T. Nash, R. Nichol, J. R. Pier, G. T. Richards, D. P. Schneider,

C. Stoughton, A. S. Szalay, A. R. Thakar, and D. G. York, “Evidence for reionization at z 6: Detection of a gunn-peterson trough in a z = 6.28 quasar,” *The Astronomical Journal*, vol. 122, no. 6, p. 2850, 2001.

[41] R. Adam *et al.*, “Planck intermediate results. XLVII. Planck constraints on reionization history,” *Astron. Astrophys.*, vol. 596, p. A108, 2016.

[42] E. Di Valentino *et al.*, “Exploring Cosmic Origins with CORE: Cosmological Parameters,” 2016.

[43] R. A. Sunyaev and I. B. Zeldovich, “Microwave background radiation as a probe of the contemporary structure and history of the universe,” *Annual review of astronomy and astrophysics*, vol. 18, pp. 537–560, 1980.

[44] J. E. Carlstrom, G. P. Holder, and E. D. Reese, “Cosmology with the Sunyaev-Zel’dovich effect,” *Ann. Rev. Astron. Astrophys.*, vol. 40, pp. 643–680, 2002.

[45] M. Hasselfield *et al.*, “The Atacama Cosmology Telescope: Sunyaev-Zel’dovich selected galaxyclusters at 148 GHz from three seasons of data,” *JCAP*, vol. 1307, p. 008, 2013.

[46] P. A. R. Ade *et al.*, “Planck 2015 results. XXIV. Cosmology from Sunyaev-Zeldovich cluster counts,” *Astron. Astrophys.*, vol. 594, p. A24, 2016.

[47] C. L. Reichardt, B. Stalder, L. E. Bleem, T. E. Montroy, K. A. Aird, K. Andersson, R. Armstrong, M. L. N. Ashby, M. Bautz, M. Bayliss, G. Bazin, B. A. Benson, M. Brodwin, J. E. Carlstrom, C. L. Chang, H. M. Cho, A. Clocchiatti, T. M. Crawford, A. T. Crites, T. de Haan, S. Desai, M. A. Dobbs, J. P. Dudley, R. J. Foley, W. R. Forman, E. M. George, M. D. Gladders, A. H. Gonzalez, N. W. Halverson, N. L. Harrington, F. W. High, G. P. Holder, W. L. Holzapfel, S. Hoover, J. D. Hrubes, C. Jones, M. Joy, R. Keisler, L. Knox, A. T. Lee, E. M. Leitch, J. Liu, M. Lueker, D. Luong-Van, A. Mantz, D. P. Marrone, M. McDonald, J. J. McMahon, J. Mehl, S. S. Meyer, L. Mocanu, J. J. Mohr, S. S. Murray, T. Natoli, S. Padin, T. Plagge, C. Pryke, A. Rest, J. Ruel, J. E. Ruhl, B. R. Saliwanchik, A. Saro, J. T. Sayre, K. K. Schaffer, L. Shaw, E. Shirokoff, J. Song, H. G. Spieler, Z. Staniszewski, A. A. Stark, K. Story, C. W. Stubbs, R. Šuhada, A. van Engelen, K. Vanderlinde, J. D. Vieira, A. Vikhlinin, R. Williamson, O. Zahn, and A. Zenteno, “Galaxy Clusters Discovered via the Sunyaev-Zel’dovich Effect in the First 720 Square Degrees of the South Pole Telescope Survey,”

[48] N. Aghanim *et al.*, “Planck 2015 results. XI. CMB power spectra, likelihoods, and robustness of parameters,” *Astron. Astrophys.*, vol. 594, p. A11, 2016.

[49] T. Louis *et al.*, “The Atacama Cosmology Telescope: Two-Season ACTPol Spectra and Parameters,” *JCAP*, vol. 1706, no. 06, p. 031, 2017.

[50] J. W. Henning *et al.*, “Measurements of the Temperature and E-Mode Polarization of the CMB from 500 Square Degrees of SPTpol Data,” *Submitted to: Astrophys. J.*, 2017.

[51] H. C. Chiang, P. A. R. Ade, D. Barkats, J. O. Battle, E. M. Bierman, J. J. Bock, C. D. Dowell, L. Duband, E. F. Hivon, W. L. Holzapfel, V. V. Hristov, W. C. Jones, B. G. Keating, J. M. Kovac, C. L. Kuo, A. E. Lange, E. M. Leitch, P. V. Mason, T. Matsumura, H. T. Nguyen,

N. Ponthieu, C. Pryke, S. Richter, G. Rocha, C. Sheehy, Y. D. Takahashi, J. E. Tolan, and K. W. Yoon, “Measurement of cosmic microwave background polarization power spectra from two years of bicep data,” *The Astrophysical Journal*, vol. 711, no. 2, p. 1123, 2010.

[52] P. A. R. Ade *et al.*, “BICEP2 / Keck Array V: Measurements of B-mode Polarization at Degree Angular Scales and 150 GHz by the Keck Array,” *Astrophys. J.*, vol. 811, p. 126, 2015.

[53] P. A. R. Ade *et al.*, “A Measurement of the Cosmic Microwave Background B-Mode Polarization Power Spectrum at Sub-Degree Scales from 2 years of POLARBEAR Data,” 2017.

[54] A. Challinor, P. Fosalba, D. Mortlock, M. Ashdown, B. Wandelt, and K. Górski, “All-sky convolution for polarimetry experiments,” *Phys. Rev. D*, vol. 62, p. 123002, Nov 2000.

[55] L. Knox, “Determination of inflationary observables by cosmic microwave background anisotropy experiments,” *Phys. Rev. D*, vol. 52, pp. 4307–4318, Oct 1995.

[56] J. Delabrouille *et al.*, “Exploring Cosmic Origins with CORE: Survey requirements and mission design,” 2017.

[57] P. Natoli *et al.*, “Exploring cosmic origins with CORE: mitigation of systematic effects,” 2017.

[58] M. Remazeilles *et al.*, “Exploring Cosmic Origins with CORE: B-mode Component Separation,” 2017.

[59] K. N. Abazajian *et al.*, “CMB-S4 Science Book, First Edition,” 2016.

[60] J. B. Melin *et al.*, “Exploring Cosmic Origins with CORE: Cluster Science,” 2017.

[61] A. Challinor *et al.*, “Exploring cosmic origins with CORE: gravitational lensing of the CMB,” 2017.

[62] T. Matsumura *et al.*, “Mission design of LiteBIRD,” 2013.
[J. Low. Temp. Phys.176,733(2014)].

[63] M. Remazeilles, C. Dickinson, H. K. K. Eriksen, and I. K. Wehus, “Sensitivity and foreground modelling for large-scale cosmic microwave background B-mode polarization satellite missions,” *Mon. Not. Roy. Astron. Soc.*, vol. 458, no. 2, pp. 2032–2050, 2016.

[64] A. Kogut, D. Fixsen, D. Chuss, J. Dotson, E. Dwek, M. Halpern, G. Hinshaw, S. Meyer, S. Moseley, M. Seiffert, D. Spergel, and E. Wollack, “The primordial inflation explorer (pixie): a nulling polarimeter for cosmic microwave background observations,” *Journal of Cosmology and Astroparticle Physics*, vol. 2011, no. 07, p. 025, 2011.

[65] J. Errard *et al.*, “Modeling atmospheric emission for CMB ground-based observations,” *Astrophys. J.*, vol. 809, p. 63, 2015.

[66] D. Poletti *et al.*, “Making maps of Cosmic Microwave Background polarization for B-mode studies: the POLARBEAR example,” *Astron. Astrophys.*, vol. 600, p. A60, 2017.

[67] F. Finelli *et al.*, “Exploring Cosmic Origins with CORE: Inflation,” 2016.

[68] D. T. Hoang, G. Patanchon, M. Bucher, T. Matsumura, R. Banerji, H. Ishino, M. Hazumi, and J. Delabrouille, “Bandpass mismatch error for satellite CMB experiments I: Estimating the spurious signal,” 2017.

[69] P. A. R. Ade *et al.*, “Planck 2013 results. I. Overview of products and scientific results,” *Astron. Astrophys.*, vol. 571, p. A1, 2014.

[70] B. A. Benson *et al.*, “SPT-3G: A Next-Generation Cosmic Microwave Background Polarization Experiment on the South Pole Telescope,” *Proc. SPIE Int. Soc. Opt. Eng.*, vol. 9153, p. 91531P, 2014.

[71] Planck Collaboration, “Planck 2015 results - vii. high frequency instrument data processing: Time-ordered information and beams,” *Astron. Astrophys.*, vol. 594, p. A7, 2016.

[72] R. Adam *et al.*, “Planck 2015 results. VIII. High Frequency Instrument data processing: Calibration and maps,” *Astron. Astrophys.*, vol. 594, p. A8, 2016.

[73] N. Aghanim *et al.*, “Planck intermediate results. XLVI. Reduction of large-scale systematic effects in HFI polarization maps and estimation of the reionization optical depth,” *Astron. Astrophys.*, vol. 596, p. A107, 2016.

[74] P. A. R. Ade *et al.*, “Planck 2015 results. III. LFI systematic uncertainties,” *Astron. Astrophys.*, vol. 594, p. A3, 2016.

[75] Planck Collaboration, “Planck intermediate results - xlvi. reduction of large-scale systematic effects in hfi polarization maps and estimation of the reionization optical depth,” *Astron. Astrophys.*, vol. 596, p. A107, 2016.

[76] M. Tegmark, “CMB mapping experiments: A Designer’s guide,” *Phys. Rev.*, vol. D56, pp. 4514–4529, 1997.

[77] M. A. J. Ashdown *et al.*, “Making sky maps from Planck data,” *Astron. Astrophys.*, vol. 467, pp. 761–775, 2007.

[78] B. Revenu, F. Couchot, J. Delabrouille, and J. Kaplan, “Destriping Polarised Data,” *Astrophysical Letters and Communications*, vol. 37, p. 267, 2000.

[79] H. Kurki-Suonio, E. Keihänen, R. Keskitalo, T. Poutanen, A.-S. Sirviö, D. Maino, and C. Burigana, “Destriping CMB temperature and polarization maps,” *Astron. Astrophys.*, vol. 506, pp. 1511–1539, Nov. 2009.

[80] C. M. Cantalupo, J. D. Borrill, A. H. Jaffe, T. S. Kisner, and R. Stompor, “MADmap: A Massively Parallel Maximum Likelihood Cosmic Microwave Background Map-maker,” *“Th Astrophysical Journal Supplements”*, vol. 187, pp. 212–227, Mar. 2010.

[81] E. Keihänen, R. Keskitalo, H. Kurki-Suonio, T. Poutanen, and A.-S. Sirviö, “Making cosmic microwave background temperature and polarization maps with MADAM,” *Astron. Astrophys.*, vol. 510, p. A57, Feb. 2010.

[82] R. Adam *et al.*, “Planck 2015 results. X. Diffuse component separation: Foreground maps,” *Astron. Astrophys.*, vol. 594, p. A10, 2016.

[83] G. de Gasperis, A. Balbi, P. Cabella, P. Natoli, and N. Vittorio, “ROMA: A map-making algorithm for polarised CMB data sets,” *Astron. Astrophys.*, vol. 436, pp. 1159–1165, June 2005.

[84] M. Tegmark, “How to make maps from CMB data without losing information,” *Astrophys. J.*, vol. 480, pp. L87–L90, 1997.

[85] R. Stompor *et al.*, “Making maps of the cosmic microwave background: The MAXIMA example,” *Phys. Rev.*, vol. D65, p. 022003, 2002.

[86] Couchot, F., Delabrouille, J., Kaplan, J., and Revenu, B., “Optimised polarimeter configurations for measuring the stokes parameters of the cosmic microwave background radiation,” *Astron. Astrophys. Suppl. Ser.*, vol. 135, no. 3, pp. 579–584, 1999.

[87] P. de Bernardis *et al.*, “Exploring Cosmic Origins with CORE: The Instrument,” 2017.

[88] E. Keihanen, H. Kurki-Suonio, T. Poutanen, D. Maino, and C. Burigana, “A maximum likelihood approach to the destriping technique,” *Astron. Astrophys.*, vol. 428, pp. 287–298, 2004.

[89] S. Mitra, G. Rocha, K. M. Gorski, K. M. Huffenberger, H. K. Eriksen, M. A. J. Ashdown, and C. R. Lawrence, “Fast Pixel Space Convolution for CMB Surveys with Asymmetric Beams and Complex Scan Strategies: FEBeCoP,” *Astrophys. J. Suppl.*, vol. 193, p. 5, 2011.

[90] P. A. R. Ade *et al.*, “Planck 2013 results. VII. HFI time response and beams,” *Astron. Astrophys.*, vol. 571, p. A7, 2014.

[91] C. Armitage and B. D. Wandelt, “Deconvolution map-making for cosmic microwave background observations,” *Phys. Rev.*, vol. D70, p. 123007, 2004.

[92] E. Keihänen and M. Reinecke, “ArtDeco: a beam-deconvolution code for absolute cosmic microwave background measurements,” *Astron. Astrophys.*, vol. 548, p. A110, Dec. 2012.

[93] E. Komatsu *et al.*, “Results from the Wilkinson Microwave Anisotropy Probe,” *PTEP*, vol. 2014, p. 06B102, 2014.

[94] J. Delabrouille, M. Betoule, J.-B. Melin, M.-A. Miville-Deschênes, J. Gonzalez-Nuevo, M. Le Jeune, G. Castex, G. de Zotti, S. Basak, M. Ashdown, J. Aumont, C. Baccigalupi, A. J. Banday, J.-P. Bernard, F. R. Bouchet, D. L. Clements, A. da Silva, C. Dickinson, F. Dodu, K. Dolag, F. Elsner, L. Fauvet, G. Faÿ, G. Giardino, S. Leach, J. Lesgourgues, M. Liguori, J. F. Macías-Pérez, M. Massardi, S. Matarrese, P. Mazzotta, L. Montier, S. Mottet, R. Paladini, B. Partridge, R. Piffaretti, G. Prezeau, S. Prunet, S. Ricciardi, M. Roman, B. Schaefer, and L. Toffolatti, “The pre-launch Planck Sky Model: a model of sky emission at submillimetre to centimetre wavelengths,” *Astron. Astrophys.*, vol. 553, p. A96, May 2013.

[95] C. Rosset, V. Yurchenko, J. Delabrouille, J. Kaplan, Y. Giraud-Heraud, J.-M. Lamarre, and A. J. Murphy, “Beam mismatch effects in cosmic microwave background polarization measurements,” *Astron. Astrophys.*, vol. 464, pp. 405–415, 2007.

[96] N. Aghanim *et al.*, “Planck 2015 results. XI. CMB power spectra, likelihoods, and robustness of parameters,” *Astron. Astrophys.*, vol. 594, p. A11, 2016.

[97] M. Shimon, B. Keating, N. Ponthieu, and E. Hivon, “CMB Polarization Systematics Due to Beam Asymmetry: Impact on Inflationary Science,” *Phys. Rev.*, vol. D77, p. 083003, 2008.

[98] E. Hivon, S. Mottet, and N. Ponthieu, “QuickPol: Fast calculation of effective beam matrices for CMB polarization,” *Astron. Astrophys.*, vol. 598, p. A25, 2017.

[99] C. G. R. Wallis, M. L. Brown, R. A. Battye, G. Pisano, and L. Lamagna, “Removing beam asymmetry bias in precision CMB temperature and polarization experiments,” *Mon. Not. Roy. Astron. Soc.*, vol. 442, no. 3, pp. 1963–1979, 2014.

[100] C. G. R. Wallis, M. L. Brown, R. A. Battye, and J. Delabrouille, “Optimal scan strategies for future cmb satellite experiments,” *Monthly Notices of the Royal Astronomical Society*, vol. 466, no. 1, p. 425, 2017.